5-19-2015 12:00 AM

Ion beam modification of strontium titanate and highly oriented pyrolytic graphite

Olga Lobacheva, *The University of Western Ontario*

Supervisor: Prof. Lyudmila Goncharova, *The University of Western Ontario*

A thesis submitted in partial fulfillment of the requirements for the Doctor of Philosophy degree in Physics

ION BEAM MODIFICATION OF STRONTIUM TITANATE AND HIGHLY ORIENTED PYROLYTIC GRAPHITE

(Thesis format: Monograph)

by

Olga Lobacheva

Graduate Program in Physics

A thesis submitted in partial fulfillment
of the requirements for the degree of
Doctor of Philosophy

The School of Graduate and Postdoctoral Studies
The University of Western Ontario
London, Ontario, Canada

Abstract

Doping and structural modification affects such important characteristics as conductivity, catalytic activity, luminescent and magnetic properties of modern materials. Ion beam implantation is a conventional doping method which combines a low processing temperature with convenient control of concentration and distribution of dopant and irradiation damage. In this study, the ion beam implantation method was used to modify strontium titanate (STO) and highly oriented pyrolytic graphite (HOPG). Both materials have immense potential for applications in different areas of modern technology, including gas sensing, catalysis, electronics and spintronics. Fe-implanted STO and N- and O-implanted HOPG were examined with complementary experimental techniques, including Particle Induced X-ray Emission (PIXE), Rutherford Backscattering (RBS), X-ray Absorption Near Edge Structure (XANES) and X-ray Photoemission (XPS). Magnetic properties were analyzed with Superconducting quantum interference device (SQUID) magnetometry.

Irradiation with ion beams modifies structure and increases the surface reactivity of STO and HOPG. XPS reveals an increase of O and C content on STO surface due to reactions with gases from the ambient atmosphere with the surface defects. XANES analysis detects the formation of carbonyl and other functional groups as well as amorphization with formation of sp^3 carbon species on the ion irradiated HOPG surfaces. Iron irradiation and post-implantation annealing in O_2 at 350°C cause unexpected loss of Sr at the surface area of STO due to formation of lower density $SrCO_3$ and $Sr(OH)_2$ phases and possible SrO desorption.

The STO single crystals exhibit weak ferromagnetic moments prior to implantation. The maximum saturation moment is obtained after our highest implantation dose of 2×10^{16} Fe atom/cm^2, which could be correlated with the metallic Fe^0 phases in addition to the presence of O/Ti vacancies. The annealing in oxygen atmosphere partially heals implantation damages and changes the oxidation state of the implanted iron from metallic Fe^0 to Fe^{2+}/Fe^{3+} oxide, accompanied by a loss of the ferromagnetic response. Iron oxide phases with Fe^{2+} and Fe^{3+} states corresponding to this regime are identified and their structures are confirmed by calculations using the Real Space Multiple Scattering program (FEFF9). Magnetic moments of the N-and O-implanted HOPG samples are correlated well with transition metal impurities.

Keywords

Ion beam modification, Rutherford Backscattering Spectrometry, Particle Induced X-Ray Emission, X-Ray Photoelectron Spectroscopy, X-Ray Absorption Near Edge Structure, Superconducting Quantum Interference Device, Strontium titanate, Highly-Oriented Pyrolytic Graphite, Fe doping.

Co-authorship statement

The following thesis contains experimental data from a previously published paper written in co-authorship with Y.M. Yiu, T.K. Sham, and L.V. Goncharova. The experimental results presented in the article are shown in Chapters 5 and 7. Olga Lobacheva was the primary author responsible for the majority of the experimental work, as well as the writing and revision of all drafts, including final manuscripts. Y.M. Yiu performed FEFF9 simulations used in the article. Dr L.V. Goncharova and Dr. T.K. Sham were supervising Olga Lobacheva. They participated in the discussion of the experimental results and revision of the final drafts.

Part of the XANES data was collected by Robert Gordon at Argonne National Laboratory, and SQUID measurements were performed by Samer Kahwaji at MBE Lab of Dalhousie University.

Acknowledgement

I wish to express many thanks to my supervisor Dr. L.V. Goncharova, who guided me with friendship and patience through my academic work and led me to strive for excellence in my work. I express my undying gratitude to Dr. TK. Sham who has worked with me ever since I embarked on my Masters career in Western University and all throughout my PhD. His support, social involvement, and an unending belief in me and all of his students helped me grow and accomplish things I didn't believe possible.

I wish to express my gratitude to people who made my research effective and possible. I thank Jack Hendriks for his unruffled calm in all situations as he helped me at the Tandetron with ion beam implantation and analysis. I owe my gratitude to Robert Gordon of Argonne National Laboratory (USA) for his help with XANES experiment, to Mark Biesinger of Surface Science Western for help with XPS analysis of samples and Samer Kahwaji of MBE Lab of Dalhousie University for his assistance with SQUID measurement. My special thanks to Mui Yiu for her help with FEFF9 simulations of XANES spectra, positive attitude and constructive feedback. Thank you very much for helping me navigate through the technical difficulties of my research.

It has been such a pleasure to work with all of my talented and dedicated colleagues at Western and CLS. It is your passion for experimental physics, the in-depth knowledge of your field, and your friendships that served as a constant inspiration to me. Your support and kindness were essential for the completion of my thesis.

I thank my dear family for the encouragement to pursue my professional goals, for all the rides to and from work, and for filling in as family cooks – and the furry family cat who reminded me of the simple pleasures in life. It has been a journey full of personal growth, trial and error, collaboration, learning, and occasional shopping therapy. I thank you all, without you none of it would be possible!

Table of Contents

List of Tables

List of Figures

List of abbreviations

2DEG	two-dimensional electron gas
amu	atomic mass unit
APS	Advanced Photon Source
BE	binding energy
CLS	Canadian Light Source
DFT	density functional theory
DMS	dilute magnetic semiconductor
DOS	density of states
EELS	electron energy loss spectroscopy
EXAFS	Extended X-ray Absorption Fine Structure
HBE	high binding energy
HOPG	Highly oriented pyrolytic graphite
KE	kinetic Energy
LOD	limit-of-detection
NIST	National Institute of Standards and Technology
PIXE	Particle Induced X-ray Emission
RBS	Rutherford Backscattering Spectrometry
RKKY	Rudermann–Kittel–Kasuya–Yosida interaction
SEM	Scanning Electron Microscopy
SQUID	Superconducting Quantum Interference Device
SRIM	The Stopping and Range of Ions in Matter
STF	strontium titanium ferrate $SrTi_{1-x}Fe_xO_3$
STM	Scanning Transmission Microscopy
STO	strontium titanate $SrTiO_3$
TEM	Transmission Electron Microscopy
TEY	total electron yield

TFY	total fluorescence yield
TM	transition metal
TRIM	Transport of Ions in Matter
UHV	ultra-high vacuum
XAFS	X-ray Absorption Fine Structure
XANES	X-ray Absorption Near Edge Structure
XPS	X-ray Photoelectron Spectroscopy

Chapter 1. Materials for modern technology

1.1 Motivation

The growth of digital electronics creates a great demand for new materials for information and communication technology, processing and storage of data, photonic technology, energy industry and others applications [1]. Recently considerable interest has been focused on the functional perovskite oxides owing to their rich physics and great potentials as the next-generation electronic materials. Basic research has been boosted by a series of discoveries of their amazing properties including superconductivity, tunneling magnetoresistance, piezoelectric, ferromagnetic, ferroelectric, and multiferroic behaviour, resistive switching behaviour, giant thermoelectric and photoconductivity effects, and exceptional catalytic properties [2-5]. Novel perovskite oxide materials find versatile applications in optical electronics, gas sensors, photocatalysts, oxide cathodes, insulating layers in random access memory, ferroelectric thin film structures, high-T_C superconductors, and gate dielectric material [6-8].

This multitude of properties comes with a price. Only a few parameters must be controlled to obtain reliable device performance in conventional semiconductors such as silicon. A vast knowledge has been accumulated on the microfabrication routes that do not degrade properties and allow a system control with complex device functionality. Numerous studies have shown that electronic, light-emitting and magnetic properties of perovskite oxide materials depend to the greatest extent on the doping (or impurities) and defects in different crystal structures [9].

However, the tendency to form oxygen vacancies or to develop dopant concentration gradients in perovskite oxides significantly hinders the device fabrication. The improved ability to control the growth of thin films and modify properties at the atomic scale developed in recent years have extended the possibility of creating new materials by alternating the thin-film growth of two materials on top of each other and repeating the sequence multiple times [10]. The structures consisting only of few monolayers, so-called “superlattices” or artificial lattices, indeed do not have their bulk

analogs. This opens the possibility to either enhance or introduce completely new properties that are completely absent in the parent compounds.

Until the late 1990s, the semiconductor industry has relied on silicon, a material which is abundant and well understood, has excellent mobility properties, and offered inexpensive fabrication routes. Silicon can be conveniently oxidized producing a SiO_2 dielectric layer with a sharp interface to be used as a transistor gate insulator. However, with further miniaturization new materials, new device geometries and new switching concepts are required.

Intense research activity is aimed to the search of other high-mobility semiconductor materials and new oxide materials which can replace SiO_2 as a gate dielectric material. At thickness ~ 1.2 nm silicon dioxide ceases to be perfectly insulating, and the tunneling-induced leakage current becomes unacceptably high. Oxides with high dielectric constant (high-κ dielectrics) can improve the operation of electronic devices. Besides desirable dielectric constant the material should possess good thermal stability, thermodynamic compatibility with semiconductor and low defect density at the dielectric/semiconductor interface. Besides silicon nitride and nitrided SiO_2 the candidates were Ta_2O_5, TiO_2, Al_2O_3, ZrO_2, $HfSi_xO_y$, and $SrTiO_3$ films grown by atomic layer deposition, metal-organic chemical vapour deposition, and molecular beam epitaxy [11]. Unfortunately many of them, including TiO_2 and Ta_2O_5, are not suitable, as they are not thermodynamically stable in contact with Si [12].

Contemporary interest in $SrTiO_3$ material examined in this thesis was focused on its multiple roles in the post-Si semiconductor technology applications. First, the excellent electrical properties of the $SrTiO_3$/Si structures were reported with capacitance electrically equivalent to that of an SiO_2 film less than 10 Å thick [13]. Epitaxial $SrTiO_3$ is an excellent dielectric providing a higher uniformity and lower defect density compared to polycrystalline metal oxide films. Second, $SrTiO_3$ can be used as a buffer layer, as its lattice structure permits epitaxial integration with other functional transition metal oxides, such as $SrRuO_3$ or $LaAlO_3$. Finally, $SrTiO_3$, either doped with magnetic ions or significantly reduced, can be used for spintronic applications [14]. Computing with spins and magnets, instead of conventional logic architecture, has several advantages if

implemented. This information storage is non-volatile, has less power consumption and power dissipation issues, since the operating voltages are typically lower than 1 V [15].

Another class of materials for novel post-Si technology applications is carbon with its various allotropes and a wide range of properties [16].

Carbon-based materials comprise a huge amount of different structures from 0D fullerene to 2D graphene and 3D graphite, diamond and so on. Introduction of defects and doping allows us to engineer new structures and to change electronic, mechanical and chemical properties of carbon materials [17-19]. In recent years, there have been numerous reports of defect-induced ferromagnetism in graphite and graphene materials which promotes their use in spintronics [20-24].

Different carbon materials are very appealing for catalytic applications both as support for active phases and as catalyst themselves. They are environmentally friendly and can be a cheaper replacement of conventionally used platinum catalyst. Studies have shown that carbon-based catalysts can be applied in different fields including hydrocarbon conversion, chemical production, fuel cells, and solar energy. Variety of catalytic processes includes gas phase, liquid phase, oxygen reduction, and photocatalytic reactions [25-28]. The catalytic activity of graphite can be modified and enhanced by oxygen and nitrogen functional groups adsorbed on the surface defects. They have a versatile potential for use in reactions of dehydration of alcohols, nitric oxide and sulfur dioxide oxidation [27, 29, 30]. Nitrogen doped carbon materials have been studied as a substitution of Pt catalyst in fuel cell anodes [31-34].

In this thesis, I have summarized the results of the surface analysis studies of the local structure and magnetic properties of $SrTiO_3$ and highly oriented pyrolytic graphite modified by ion beams. Ion beam implantation has been routinely used in the semiconductor industry for doping (for example, producing n- and p-type Si), fabrication of buried layers and imbedded nanocrystals [35]. The main advantage of this approach is that implanted doses and produced structural modification can be easily controlled by ion beam parameters. The effect of ion irradiation on the structure and properties of materials was studied by several methods including Rutherford backscattering spectroscopy (RBS), particle-induced X-ray emission (PIXE), X-ray photoelectron spectroscopy (XPS), X-ray absorption near edge structure (XANES), and superconducting quantum interference

device (SQUID) analysis. We found iron and iron oxide phases corresponding to the ferromagnetic response at room temperature. Their structures were confirmed using Real Space Multiple Scattering calculation (FEFF9).

The thesis is organized as follows. Chapter 2 discusses the experimental methods used for sample fabrication and their analysis, including ion implantation, RBS, PIXE, XPS and XANES that are used extensively throughout this work. SQUID measurements were conducted at Dalhousie University by our collaborators. Therefore, in Chapter 2 we present the theoretical background behind these methods, as well as some essential data interpretation caveats. The idea is to provide a reader with a substantial background in order to understand Chapters 4-7. The basic structural properties of strontium titanate and graphite materials, as well as their defects are described in Chapter 3. Chapters 4 and 5 present RBS, PIXE, XPS and XANES experimental results for the Fe-implanted strontium titanate. XANES is particularly suitable to study ion-irradiated systems, which can be highly disordered or even amorphous, since no long-range crystal order is necessary to get this information. We found correlation between observed magnetic behaviour, Fe phases, defect concentrations and order. For better interpretation of XANES spectra at Fe K-edge, FEFF9 calculations were performed using the Real Space Multiple-Scattering (RSMS) formalism which takes advantage of the close connection between XANES and electronic structure. We also observed unusual loss of Sr from the surface layer affected by implantation. Thermodynamic parameters of several processes involved are discussed and quantified. Experimental RBS, PIXE and XANES data for N and O ion implanted HOPG are summarized in Chapter 6. Surprisingly, the produced irradiation damage was similar for both ions. Defects produced by ion irradiation increase the surface reactivity. Reaction of defective graphite surface with ambient atmosphere led to formation of various oxygen functional groups. The origin of magnetism in oxide and graphite materials is further considered in Chapter 7. It was recently discovered that ferromagnetic behaviour is possible in materials that were not considered to be traditionally magnets before. Here, our experimental SQUID results for ion implanted strontium titanate and graphite are further considered. Chapter 8 presents the conclusion as well as outlines potentials for future studies.

References

[1] P. Ball, Electronic materials: Oxides in electronics, Mrs Bulletin 38 (2013) 873-875.
[2] J.F. Schooley, W.R. Hosler, M.L. Cohen, Superconductivity in Semiconducting $SrTiO_3$, Physical Review Letters 12 (1964) 474-475.
[3] M. Bowen, M. Bibes, A. Barthelemy, J.P. Contour, A. Anane, Y. Lemaitre, A. Fert, Nearly total spin polarization in $La_{2/3}Sr_{1/3}MnO_3$ from tunneling experiments, Appl. Phys. Lett. 82 (2003) 233-235.
[4] J.M. Rondinelli, N.A. Spaldin, Substrate coherency driven octahedral rotations in perovskite oxide films, Phys Rev B 82 (2010) 1-4.
[5] J. Wang, J.B. Neaton, H. Zheng, V. Nagarajan, S.B. Ogale, B. Liu, D. Viehland, V. Vaithyanathan, D.G. Schlom, U.V. Waghmare, N.A. Spaldin, K.M. Rabe, M. Wuttig, R. Ramesh, Epitaxial $BiFeO_3$ multiferroic thin film heterostructures, Science 299 (2003) 1719-1722.
[6] F. Napolitano, A.L. Soldati, J. Geck, D.G. Lamas, A. Seyquis, Electronic and structural properties of $La_{0.4}Sr_{0.6}Ti_{1-y}Co_yO_{3\pm\delta}$ electrode materials for symmetric SOFC studied by hard X-ray absorption spectroscopy, International Journal of Hydrogen Energy 38 (2013) 8965-8973.
[7] R. Moos, N. Izu, F. Rettig, S. Reiss, W. Shin, I. Matsubara, Resistive Oxygen Gas Sensors for Harsh Environments, Sensors 11 (2011) 3439-3465.
[8] H. Liu, H. Dong, X. Meng, F. Wu, First-principles study on strontium titanate for visible light photocatalysis, Chemical Physics Letters 555 (2013) 141-144.
[9] J. Mannhart, D.G. Schlom, Semiconductor physics - The value of seeing nothing, Nature 430 (2004) 620-621.
[10] G. Rijnders, D.H.A. Blank, Materials science - Build your own superlattice, Nature 433 (2005) 369-370.
[11] N. Izyumskaya, Y. Alivov, H. Morkoc, Oxides, Oxides, and More Oxides: High-Oxides, Ferroelectrics, Ferromagnetics, and Multiferroics, Critical Reviews in Solid State and Materials Sciences 34 (2009) 89-179.
[12] D.G. Schlom, J.H. Haeni, A thermodynamic approach to selecting alternative gate dielectrics, MRS Bull. 27 (2002) 198-204.
[13] K. Eisenbeiser, J.M. Finder, Z. Yu, J. Ramdani, J.A. Curless, J.A. Hallmark, R. Droopad, W.J. Ooms, L. Salem, S. Bradshaw, C.D. Overgaard, Field effect transistors with $SrTiO_3$ gate dielectric on Si, Appl Phys Lett 76 (2000) 1324-1326.
[14] J.M.D. Coey, Ariando, W.E. Pickett, Magnetism at the edge: New phenomena at oxide interfaces, MRS Bulletin 38 (2013) 1040-1047.
[15] S.J. Pearton, W.H. Heo, M. Ivill, D.P. Norton, T. Steiner, Dilute magnetic semiconducting oxides, Semicond. Sci. Technol. 19 (2004) R59-R74.
[16] M. Terrones, A.R. Botello-Mendez, J. Campos-Delgado, F. Lopez-Urias, Y.I. Vega-Cantu, F.J. Rodriguez-Macias, A.L. Elias, E. Munoz-Sandoval, A.G. Cano-Marquez, J.-C. Charlier, H. Terrones, Graphene and graphite nanoribbons: Morphology, properties, synthesis, defects and applications, Nano Today 5 (2010) 351-372.
[17] J.R. Hahn, H. Kang, Vacancy and interstitial defects at graphite surfaces: Scanning tunneling microscopic study of the structure, electronic property, and yield for ion-induced defect creation, Phys. Rev. B 60 (1999) 6007-6017.

[18] A.V. Krasheninnikov, F. Banhart, Engineering of nanostructured carbon materials with electron or ion beams, Nat. Mater. 6 (2007) 723-733.
[19] D.W. Boukhvalov, M.I. Katsnelson, Chemical Functionalization of Graphene with Defects, Nano Lett. 8 (2008) 4373-4379.
[20] H. Ohldag, P. Esquinazi, E. Arenholz, D. Spemann, M. Rothermel, A. Setzer, T. Butz, The role of hydrogen in room-temperature ferromagnetism at graphite surfaces, New Journal of Physics 12 (2010) 123012.
[21] M. Sepioni, R.R. Nair, S. Rablen, J. Narayanan, F. Tuna, R. Winpenny, A.K. Geim, I.V. Grigorieva, Limits on intrinsic magnetism in graphen, Physical Review Letters 105 (2010) 207205.
[22] O.V. Yazyev, Emergence of magnetism in graphene materials and nanostructures, Reports on Progress in Physics 73 (2010) 056501.
[23] R. Hohne, P. Esquinazi, V. Heera, H. Weishart, A. Setzer, D. Spemann, The influence of iron, fluorine and boron implantation on the magnetic properties of graphite, J Magn Magn Mater 320 (2008) 966-977.
[24] Z.T. He, X.M. Yang, H.H. Xia, T.Z. Regier, D.K. Chevrier, X.T. Zhou, T.K. Sham, Role of defect electronic states in the ferromagnetism in graphite, Phys Rev B 85 (2012) 144406.
[25] X.Y. Sun, R. Wang, D.S. Su, Research progress in metal-free carbon-based catalysts, Chin. J. Catal. 34 (2013) 508-523.
[26] D. Chen, A. Holmen, Z.J. Sui, X.G. Zhou, Carbon mediated catalysis: A review on oxidative dehydrogenation, Chin. J. Catal. 35 (2014) 824-841.
[27] J.L. Figueiredo, M.F.R. Pereira, The role of surface chemistry in catalysis with carbons, Catal. Today 150 (2010) 2-7.
[28] R.A. Sidik, A.B. Anderson, N.P. Subramanian, S.P. Kumaraguru, B.N. Popov, O_2 reduction on graphite and nitrogen-doped graphite: Experiment and theory, J. Phys. Chem. B 110 (2006) 1787-1793.
[29] S. Biniak, G. Szymanski, J. Siedlewski, A. Swiatkowski, The characterization of activated carbons with oxygen and nitrogen surface groups, Carbon 35 (1997) 1799-1810.
[30] E. Raymundo-Pinero, D. Cazorla-Amoros, A. Linares-Solano, The role of different nitrogen functional groups on the removal of SO_2 from flue gases by N-doped activated carbon powders and fibres, Carbon 41 (2003) 1925-1932.
[31] P.O. Lehtinen, A.S. Foster, Y.C. Ma, A.V. Krasheninnikov, R.M. Nieminen, Irradiation-induced magnetism in graphite: A density functional study, Physical Review Letters 93 (2004) 187202.
[32] B. Wang, Recent development of non-platinum catalysts for oxygen reduction reaction, J. Power Sources 152 (2005) 1-15.
[33] Y. Okamoto, First-principles molecular dynamics simulation of O_2 reduction on nitrogen-doped carbon, Applied Surface Science 256 (2009) 335-341.
[34] W.Y. Wong, W.R.W. Daud, A.B. Mohamad, A.A.H. Kadhum, K.S. Loh, E.H. Majlan, Recent progress in nitrogen-doped carbon and its composites as electrocatalysts for fuel cell applications, International Journal of Hydrogen Energy 38 (2013) 9370-9386.
[35] J. Leveneur, G.I.N. Waterhouse, J. Kennedy, J.B. Metson, D.R.G. Mitchell, Nucleation and Growth of Fe Nanoparticles in SiO_2: A TEM, XPS, and Fe L-Edge XANES Investigation, Journal of Physical Chemistry C 115 (2011) 20978-20985.

Chapter 2. Experimental methods

2.1 Incident ion techniques

2.1.1 Ion-solid interactions

Modern techniques of material analysis are based on the interaction of particles, including electrons, ions, and photons with matter. Ion beams are widely used for the analysis and modification of materials. When an energetic ion collides with a solid, it can either be elastically and inelastically scattered or it can penetrate into the solid. At moderate energies (particles with velocity $v << c$), the interactions of the projectile with the target atoms include several processes: (i) excitation or ionization of target atoms accompanied by emission of electron and photon, (ii) transfer of energy to center-of-mass motion of the interacting projectile and the target atom, and (iii) changes in the internal state of the projectile. As the projectile is moving inside the target and transferring its energy to the target atoms, it gradually slows down until it finally stops. The penetration depth is determined by the initial kinetic energy of the projectile and the interactions with the target atoms. Ion-solid interactions can be accompanied by emission of electron and photon, heating of the target, formation of defects (vacancies and interstitials), and sputtering of the target atoms.

Several ion beam analytical methods, such as Rutherford Backscattering (RBS), and Particle Induced X-ray emission (PIXE) (Fig. 2.1) were utilized in this thesis. Ion beams were also used for doping and material modification, as well as sputtering of the surface.

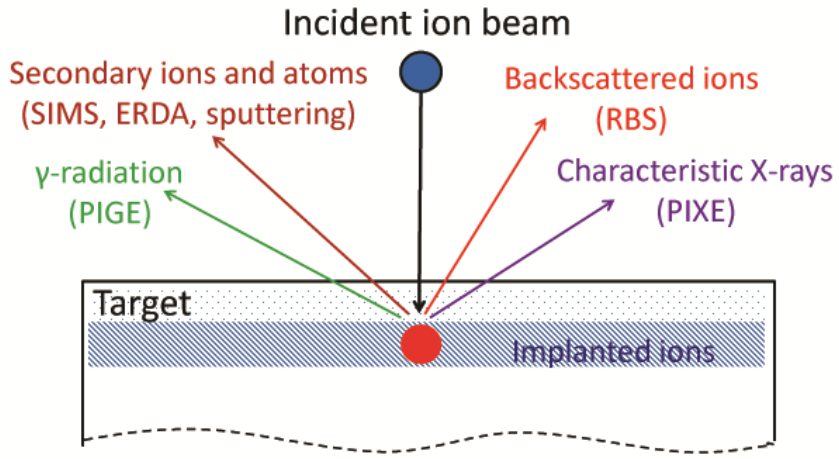

Figure 2.1. Schematic processes involved in ion-solid interactions and associated techniques: Rutherford backscattering (RBS); elastic recoil detection analysis (ERDA); particle induced X-ray emission (PIXE); particle induced γ-ray emission (PIGE); secondary ions mass spectroscopy (SIMS).

Ion-nucleus interactions are dominated by the Coulomb repulsion between two positive charges. Upon collision, ions change their energy and direction. Considering the target ion to be at rest before collision (Fig. 2.2), simple kinematic calculations give an expression for the energy of the projectile before scattering, E_0, and after scattering, E_1 and for the scattering angle θ [1]:

$$E_1 = kE_0 = \left(\frac{M_1 \cos\theta \pm \left(M_2^2 - M_1^2 \sin^2 \theta \right)^{1/2}}{M_1 + M_2} \right)^2 E_0, \qquad (2.1)$$

$$\cos\theta = \frac{1-(1+M_2/M_1)((E_o - E_1)/2E_0)}{\sqrt{1-(E_0 - E_1)/E_0}}. \qquad (2.2)$$

where M_1 and M_2 are the masses of the projectiles and target atoms, respectively. The ratio of the energy of the scattered ions to their initial energy $k = E_1 / E_0$ is called the kinematic factor.

These equations hold as long as the forces are acting along the line connecting the two interacting particles and the collision is elastic. The latter condition is fulfilled when

the projectile energy exceeds the binding energy of the target atom inside solid material, and nuclear reactions and resonances are absent.

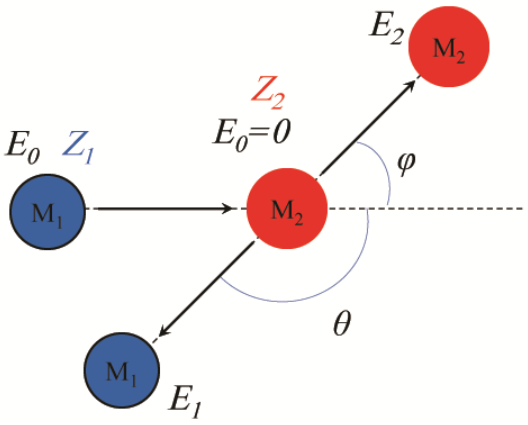

Figure 2.2. Interaction of the projectile of mass M_1 and the target ion of mass M_2.

2.1.2 Rutherford Backscattering

Rutherford Backscattering spectrometry (RBS) provides information about the elemental composition of the target as a function of depth in the near surface area (on the order of several microns) [2]. RBS uses a monoenergetic and collimated ion beam. Typically, He ion or proton energies are in the range of 0.5–4 MeV. The principle of RBS analysis is described by the equation (2.1). If the mass and the initial ion energy are known, the mass of the target ion can be easily derived by measuring the energy of backscattered ions at any particular scattering angle. The kinematic factors, *k*, calculated for the proton interaction with different elements are shown in Figure 2.3 as a function of the scattering angle. As a general trend, the change of the proton energy after the scattering is greater for larger scattering angles. In RBS experiments the energy of backscattered protons are usually monitored at scattering angles close to 180º, which provides better mass resolution (Fig. 2.4). Better mass resolution is also a reason why He ions are used more frequently than H^+.

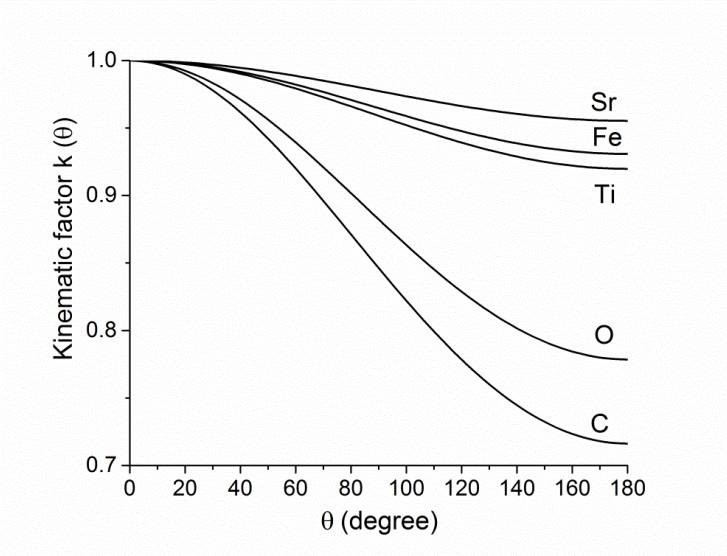

Figure 2.3. The kinematic factor *k* as function of the scattering angle for the different target elements for H^+ beam.

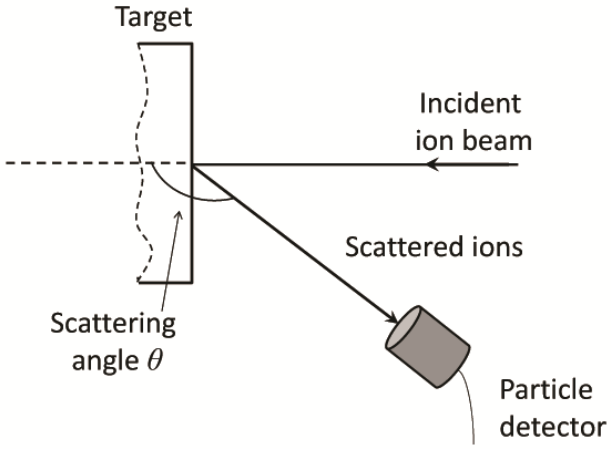

Figure 2.4. Schematic diagram of RBS experiment.

The probability of the incident ions of energy *E* to be scattered into the scattering angle θ is determined by a scattering cross-section. Differential scattering cross-section for scattering of the incident ion of energy *E* by target particles is defined as

$$\frac{d\sigma(\theta,E)}{d\Omega} = \left(\frac{1}{N\Delta x}\right)\frac{1}{Q}\frac{dQ(E)}{\Omega(\theta)}, \qquad (2.3)$$

where N is the volume density of atoms in the target, Δx is the target thickness, Q is the total number of incident ions and dQ is the number of particles scattered into the solid angle $d\Omega$. Rutherford cross-section values are calculated in the assumption that the interaction between the incident and the target ions is due to the Coulomb forces:

$$\sigma(\theta) = \left(\frac{Z_1 Z_2 e^2}{4E} \right)^2 \frac{4}{\sin^4 \theta} \frac{\left(\sqrt{1 - \left((M_1 / M_2) \sin\theta \right)^2} + \cos\theta \right)^2}{\sqrt{1 - \left((M_1 / M_2) \sin\theta \right)^2}}, \qquad (2.4)$$

Equation (2.4) shows that the cross section is proportional to the atomic numbers Z_1 and Z_2 squared, and increases for heavier incident ions and target elements. As a result, RBS is more sensitive to heavy elements, and the back scattering yield is higher for heavier projectile. The cross section is higher for smaller scattering angles, and rapidly decreases with the projectile energy (as $\propto 1/E^2$).

Some deviations from the Rutherford values become noticeable at high and low energies for all projectile-target pairs. For low energy projectiles ($E < 40$ keV/amu) or small scattering angles, the incident particle does not completely penetrate through the screening electron cloud.

This screening effect can be treated in the first order approximation using a correction factor. The screened cross section is defined as:

$$\sigma_{sc} = \sigma(\theta) F, \qquad (2.5)$$

where the correction factor $F = (1 - 0.049 Z_1 Z_2^{4/3} / E)$ and the projectile energy E are given in keV. Depending on the ion-target combination and ion energy, the screening term lies typically in the range $0.85 \le F \le 1$ [3]. For $1 MeV$ helium ions incident on strontium the correction factor is less than 2 %, and can be neglected for the most cases [4]. At high energies the deviation from the Rutherford scattering cross sections is due to nuclear interactions. The energy, at which the nuclear interactions start causing deviations from the Rutherford cross sections, can be estimated by the equation:

$$E = \frac{Z_1 Z_2 e^2}{R}, \qquad (2.6)$$

where e is elementary charge ($e^2 \approx 14.4$ eV Å), and R is the nuclear radius, which can be expressed as $R = R_o A^{1/3}$, where A is the mass number, and $R_o \approx 1.4 \times 10^{-5}$ Å [4]. For helium ions incident on Si, the energy at which one should expect the deviation from the Rutherford cross sections is ~9.6 MeV.

In some cases non-Rutherford cross sections experimentally are recorded at lower energies (in the 2–5MeV range) and the enhancement of cross sections at these energies help us to improve detection of light elements. For instance, for helium ions $^4He^+$ incident on ^{16}O, the cross section has a sharp resonance at 3.03 MeV, and it can be used to increase RBS sensitivity for oxygen detection by a factor of 15 [5]. At present, no practical method exists for rapid accurate calculations of these non-Rutherford cross sections; they must be measured.

2.1.3 Depth resolution

In the RBS method, only a small fraction (typically less than 0.1%) of the incident ions get scattered from the surface layer. The majority of the ions will penetrate into the material to depths up to several microns [6]. As the ion passes through the target, it loses its energy on its way in and out due to interaction with the target ions and electrons. This means that an ion scattered from the layer below the surface arrives at the detector with a lower energy than an ion scattered from the surface as illustrated in Figure 2.5.

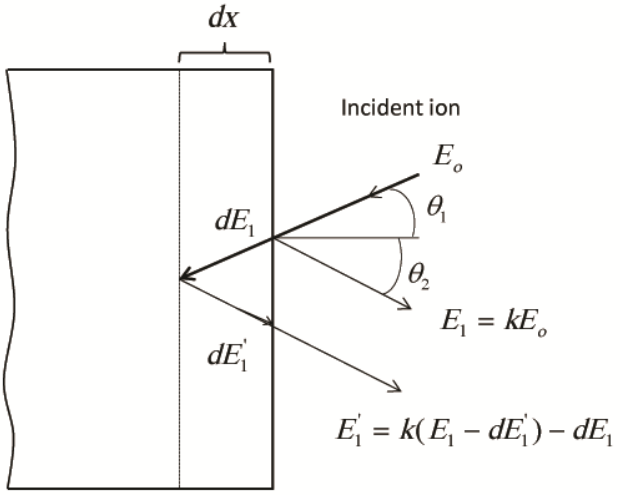

Figure 2.5 Schematic of of the energy loss processes in a thin layer.

The interaction between the projectile and the targets can be described in terms of the stopping cross section (or stopping power). The total stopping power is determined by ion interactions with electrons and nuclei of the target atoms:

$$\frac{dE}{dx} = \left(\frac{dE}{dx}\right)_e + \left(\frac{dE}{dx}\right)_n = N(\varepsilon_e + \varepsilon_n), \qquad (2.7)$$

where ε_e and ε_n are the electronic and nuclear stopping cross-sections, respectively. The former is most important, because at typical RBS beam energies of 0.5–4 MeV the projectile energy losses are determined mainly by the interactions with electrons due to a higher probability of the ion-electron collisions.

The energy loss of the ions traversing through a mono-elemental target of thickness *x* can be described by the equation:

$$E(x) = E_0 - N\int_0^x \varepsilon dx \qquad (2.8)$$

where ε is the stopping cross section.

On the other hand, it is possible to estimate the thickness of the layer if the initial and the final energy are known:

$$x = \frac{1}{N}\int_{E(x)}^{E_0} \frac{1}{\varepsilon} dE \qquad (2.9)$$

In a target composed of several elements the stopping power is calculated based on the superposition of the individual stopping energy losses according to Bragg's rule of stopping power additivity:

$$\varepsilon = \sum c_i \varepsilon_i \,, \qquad (2.10)$$

where c_i and ε_i are the concentration and the stopping power of the i^{th} element [7]. The rule is accurate for metals but not for light element compounds such as organic materials, oxides, and nitrides where the chemical and physical environments of the elements become important [6].

A schematic RBS spectrum of a Co_3Pt thin film on MgO substrate simulated using the Simulation for Nuclear Reaction Analysis (SIMNRA) program [8] is presented in

Figure 2.6. The spectrum is a superposition of the signals from the individual target element contributions. Heavy atoms on the surface are detected at the higher scattering energies. Backscattered ions reach the detector with the energy $E_i = k_i E_0$, if they scatter from the film surface. The spread in energy of Co and Pt peaks ΔE_0 reflects the film thickness. Note that the substrate surface signal appears at the energy $E_{01} = E_0 - \Delta E_0$.The incident ions have lost part of the energy in the Co_3Pt overlayer and arrived to the substrate surface at energy E_{01}. ΔE_0 is the energy loss in Co_3Pt film. As the ions go deeper into material and lose their energy, the scattering cross section and consequently the ion yield increase producing the characteristic trapezoidal shape of the RBS signal.

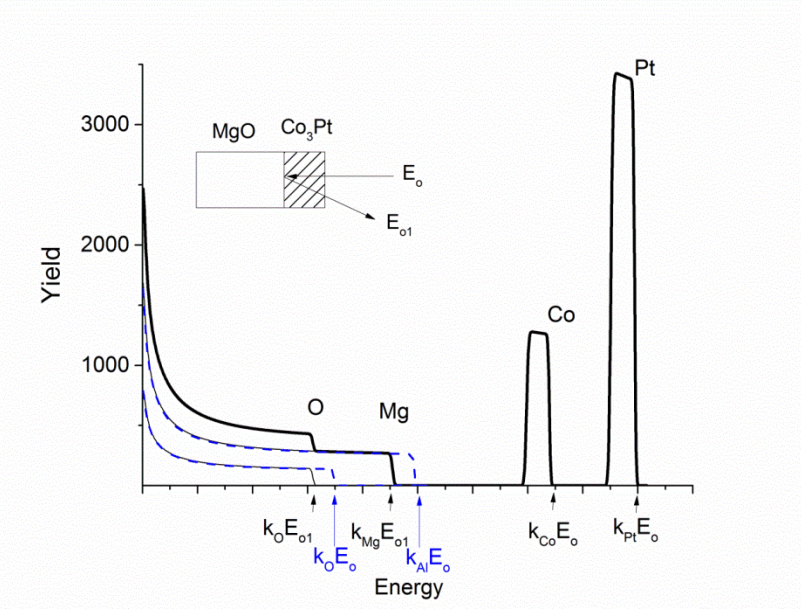

Figure 2.6 Schematic RBS spectrum of Co_3Pt thin film on MgO substrate (simulated in SIMNRA program).

RBS is a quick, easy and relatively nondestructive method, providing information about depth distribution of the elements. Interpretation of RBS spectra is facilitated by computer simulation using SIMNRA program [8]. However, some previous knowledge of the specimen composition is required to compose the target. The standard sample with well-known composition and distribution of elements is used to convert channel number of detector into energy. Typically, RBS provides depth resolution of 20 nm and mass resolution of 1–2 amu for atoms with atomic masses in the A = 20 – 100 amu range [9].

2.1.4. Channeling RBS experiments

Additional structural information can be obtained in RBS experiments by aligning the incident ion beam with so-called channeling directions which are major symmetry directions of the crystalline material. The probability of scattering events at such channeling directions is greatly reduced. Figure 2.7 shows cubic perovskite structure of strontium titanate at different geometries. If it is aligned along the <100> scattering direction, the crystal is consists of closely packed atomic rows (Fig. 2.7(a)).

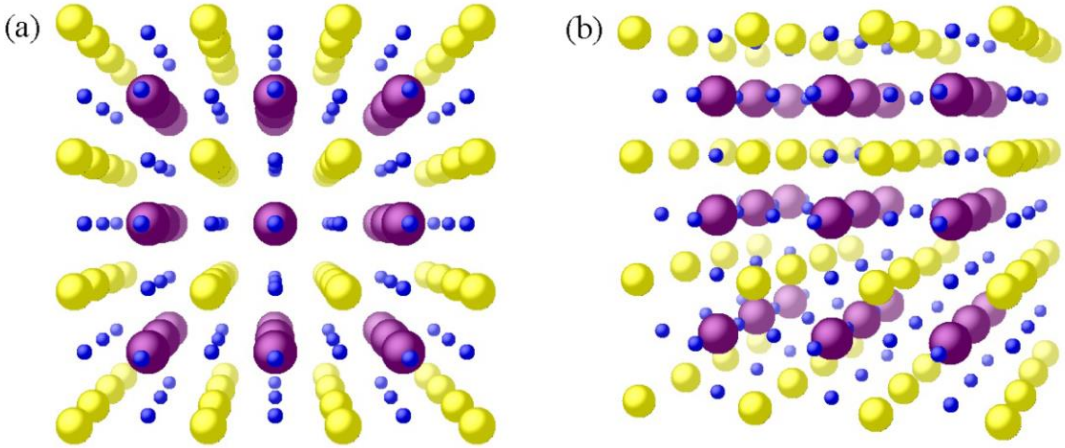

Figure 2.7. Schematic structures explaining the difference between (a) aligned along the <100> direction and (b) random scattering geometry for strontium titanate.

If the ion beam is carefully aligned with a high-symmetry direction of a crystal, the ions are gently steered by the potential field in "channels" formed by the atomic rows. The thermal vibration causes the atoms in the closely packed rows to deviate from their equilibrium positions [4]. When the ion moves along the row it senses its "roughness". As a result it cannot approach the atomic row closer than the minimum distance $r_{\min}$ for which the continuum model is valid. The interactions of a steered ion with an atomic row can be described by the continuum potential $U(r_{\min})$ that is uniformly averaged along the row. The channeled ions move by such trajectories that they make glancing angle impact with the atomic row at distances greater than 0.1 Å from the atomic cores (Fig. 2.8) [4]. The corresponding critical angle ψ_c at which the incident ions beam can be steered by the

atomic row depends on the single continuum potential $U(r_{\min})$ of the row and the ion beam energy E_o:

$$\psi_c = \sqrt{\frac{U(r_{\min})}{E_o}}, \qquad (2.10)$$

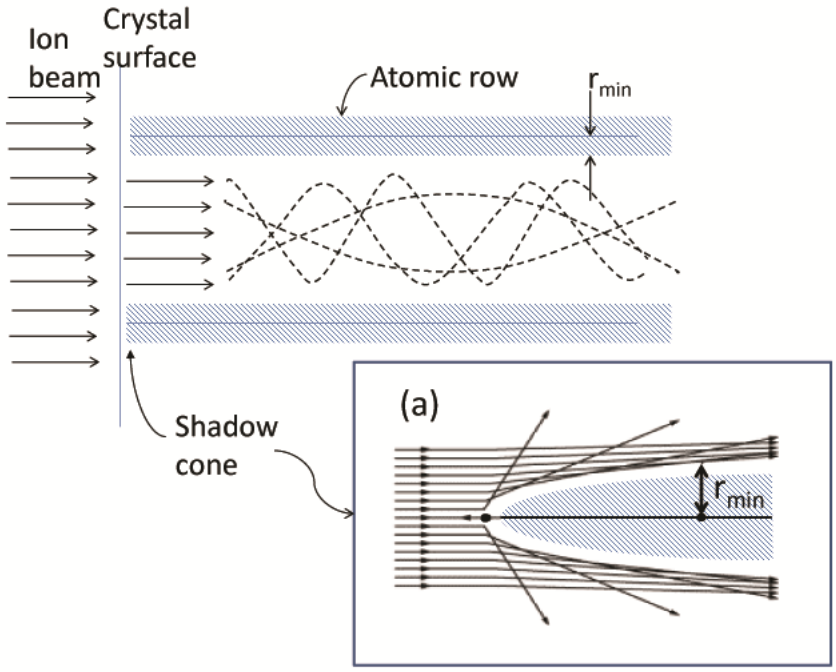

Figure 2.8 Schematic diagram of ion trajectories undergoing scattering at the surface and channeling within the crystal. Inset (a) shows the formation of a shadow cone behind a surface atom bombarded by ion beam. Adopted from Ref. [4].

The yield of channeling RBS is significantly lower compared to the yield of RBS experiment with "random" geometry when the ion beam does not align with the symmetry directions of the crystal (Fig. 2.7(b)). The minimum yield gives a measure of the fraction of particles that are not channeled, i.e. the fraction of scattered ions per number of incoming ions. In the channeling experiment for a well aligned ion beam, critical angle $\psi = 0$ and the minimum distance of approach to the atomic row $r_{\min} = \rho$, where ρ is the transverse vibrational amplitude, the minimum yield $\chi_{\min}$ is:

$$\chi_{\min}(\rho) = 3Nd\pi\rho^2, \qquad (2.11)$$

where the distances d and ρ are in Å, and the atomic concentration N is in atoms per Å^2.

As can be seen, the value of $\chi_{\min}$ is independent of the scattering parameters (Z_1, Z_2 and E_o of the ion beam). It is determined only by the crystal structure. For ideal Si crystal the minimal yield is about 3×10^{-2} ions per incident ion (or ~3%) [10]. In practice, the number of visible atoms per row can be larger due to lattice imperfections and thermal motions of the atoms.

Ions emerging from the crystal move within the same "tunnels" or channels. Similarly, they undergo the correlated scattering and emerge from the crystal with unique angular distribution. The phenomenon can be explained in terms of blocking. Figure 2.9 shows the close-encounter probability as a function of the scattering angle between the ion beam and the high-symmetry direction. If ions emerge at angles, which are slightly bigger than the critical angle, they have probability to be scattered slightly higher than 1.

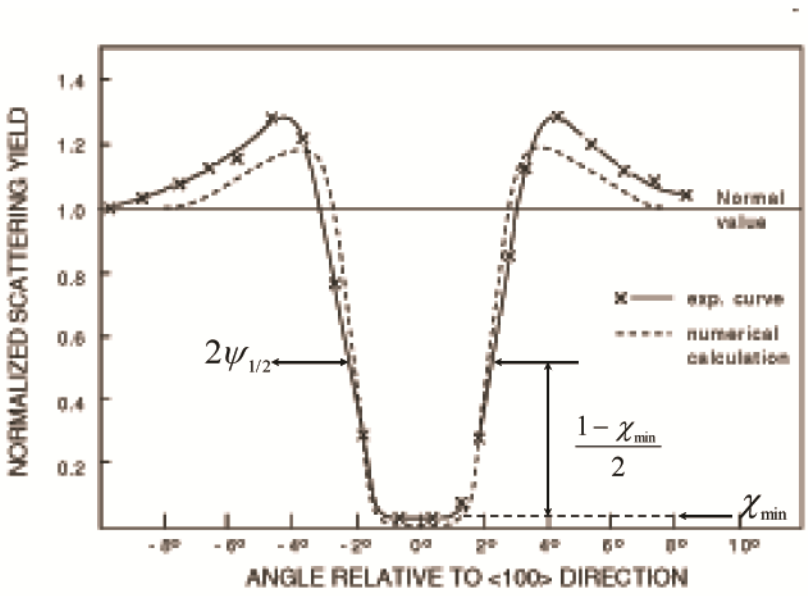

Figure 2.9 Schematic of the close-encounter probability as a function of the angle between the ion beam and the symmetry direction. Reprinted with permission from Ref. [10].

Channeling RBS is a convenient method to study radiation-induced disorder in crystals. During ion implantation experiments, doping atoms are introduced, and atoms of the host crystal are knocked out of their places producing vacancies and interstitials. These displaced atoms (as well as implanted impurities) block the channels inside crystal structure, and RBS yields from the disordered part increase. By increased scattering yield, it is possible to estimate what fraction of crystal has become disordered in the result of ion implantation. The energy spread of the RBS yield shows how deep these imperfections are.

An example of RBS-channeling experiment for silicon carbide implanted with 140 keV Ne ions at different doses is shown in Figure 2.10 [11]. Yield of channeled RBS spectrum of virgin SiC crystal is much lower than yield of the RBS spectrum collected in random geometry. Ne irradiation produces disordered area with maximal damage located below the surface of the crystal (at ~150 nm). Absence of Ne peak on the random RBS spectrum shows that Ne does not incorporate into the crystal structure. With increase of implantation dose disordering of the crystal structure increases, and de-channeling effect becomes more obvious. Surface peak is clearly detected in the channeled RBS spectrum. The peak appears due to interaction of incident ions with the first several monolayers of the target crystalline structure.

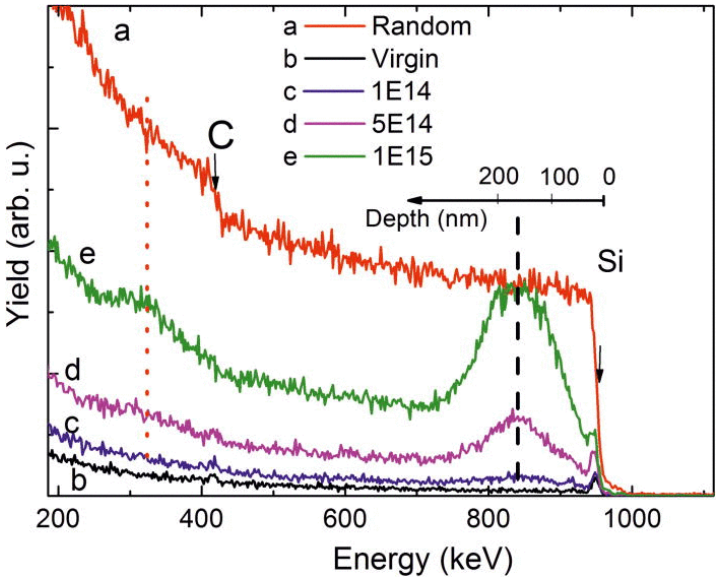

Figure 2.10. Rutherford Backscattering spectra using 1.7 MeV He ions on SiC crystal implanted with 140 keV Ne ions. Adopted from Ref. [11].

For the experimental conditions where a laterally uniform beam of ions collides with homogeneous target much larger than the beam size, the total number of particles *A* registered by a detector can be written as follows:

$$A = \sigma \times \Omega \times Q \times N\,\Delta x \qquad (2.12)$$

If σ and Ω are known, and the numbers of incident (*Q)* and detected particles *(A)* are counted, then the number of target atoms per unit area, $N\,\Delta x$ [atoms/cm^2], can be calculated from Equation 2.12. In practice, a common procedure for the determination of $N\,\Delta x$ is to calibrate the product $\Omega \times Q$ with respect to backscattering signal from a standard sample, e.g. Si, in which an accurately known number ($N\,\Delta x$) of heavy atoms, e.g. Bi or Sb, is implanted per unit area.

2.1.5 Ion beam implantation

Ion beam implantation is a fabrication technique which allows us to introduce dopants into the near-surface area in a well-controlled way. Virtually any element of the periodic table can be implanted into almost any solid material. An ion loses its energy in the interactions with the target until it finally stops inside the material, depending on its energy and the density of the target. The energy and the charge of the incident ions as well as the ion mass and the density and crystallinity of the target determine how deep it can penetrate into the target. The doping dose is easily controlled by the ion beam current and time. Ion dose is denoted by the total number of ions per unit area (ion/ cm^2) of a target material. For high implantation dose it is possible to exceed the solubility limit of an element in the host material which makes a promising way to fabricate nanomaterials [12].

Energies of the ion beams vary widely in the range from 10keV to several MeV though they can be lower or higher if different accelerators or implanters are used. At low energies, the implanted ions are distributed near the surface, for instance Au^+ implanted in alumina at the incident energy of 10 keV have an ion range of 8 nm from the surface. At higher energy, ions can penetrate deeper into material forming buried layers. Interaction of ions with solid depends also on the ion mass. At equal incident energy, a

lighter ion penetrates deeper into material than a heavier one. For instance, H^+ ions with the incident energy of 10 keV have an ion range of 90 nm in alumina.

When energetic ions hit a target, they lose their energy in the interactions with the electrons and the nuclei of the target. In the induced collision cascade, a high number of vacancies and interstitials are produced (Fig 2.11). Part of the target atoms can be ejected from the surface as recoiled or sputtered particles. The sputtering process prevails at low incident energy (0.5–20 keV), grazing incident angles and heavier incident ions. Typically, interstitials lie deeper in the target than vacancies. Being mobile they are able to form vacancy clusters (or voids), interstitial clusters, dopant-interstitial and dopant-vacancy clusters [10].

Irradiation damage depends on the type of the incident ions, on the energy, fluence and flux of the incident ions, as well as the target material which determine damage evolution, amorphization, dynamic defect recovery, and dynamic recrystallization processes [13-16].

The damage increases with the increase of the ion fluence (or implantation dose). At high dose amorphization of the surface layer occurs. Meldrum *et al.* [13] have studied the amorphization of several perovskite crystals ($CaTiO_3$, $SrTiO_3$, $BaTiO_3$, $LiNbO_3$, $KNbO_3$, $LiTaO_3$, and $KTaO_3$) resulting from the bombardment with 800 keV Kr^+, Xe^+, and Ne^+. They found that the oxide surfaces could not be amorphized by light Ne^+ ions but they were readily amorphized by Kr^+ and Xe^+.

The current or the flux of the ion beam, i.e. the rate at which ions arrive to the target surface per the unit time, is an important implantation parameter for the implantation process. Because ion bombardment causes an increase of the local temperature of the target, the self-annealing process is often competing with the irradiation damage. At low rate (or low beam current), the system has time to partially recover from the irradiation damage. At fast arrival rate (or high beam current), the ion beam can cause an accumulation of damages and, at the same time, a significant rise of target temperature, which increases the diffusion rate of atoms and the recombination rate of defects in the target material (vacancies and interstitials).

The critical temperature T_c above which the material cannot be amorphized is dependent on the material structure. For $SrTiO_3$ T_c was 370 K when irradiated with 1MeV

Au ions at any dose [16] and ~420 K when irradiated with 800 keV Kr and Xe [13]. Irradiation with 320 keV Pb ions caused full amorphization of $SrTiO_3$ only when temperatures were below 333 K [14]. With the increase of temperature significant dynamic recovery was observed [14, 15].

The self-annealing heals the lattice damage and at the same time dithers the implantation profile because it increases the diffusion rate of implanted ions. Thus, if a sharp doping profile is desirable, a special care should be taken to maintain a reasonably low target temperature during implantation [12].

The stopping of ion in the solid is a statistical process. Computer simulation program SRIM (The Stopping and Range of Ions in Matter)[6] based on the Monte-Carlo method is used to calculate the distribution of the implanted material and the defects due to ion irradiation. The input parameters include ion type and energy, target composition and its density. The program calculates ion ranges in the material depending on their energy and irradiation damage by calculation of the collision cascade for each incident ion. Figure 2.11 shows a sample of a TRIM (Transport of Ions in Matter) calculation (a part of the SRIM program) [6]. The sum of similar calculations repeated for a specified number of ions allows us to estimate the ion range and the irradiation damage to the target. Usually the incident energy E_0 exceeds the displacement energy E_d, and one ion can dislodge multiple target atoms. TRIM simulation allows excellent visualization of the distribution of implanted material and irradiation induced damage. In most cases the results are very close to the real profiles although TRIM ignores several important features of a real implantation process. The program treats the target as an amorphous and homogeneous material completely disregarding channeling processes. Also, TRIM tends to overestimate the damage produced because defect accumulation or recombinative annihilation of defects is never considered in the frame of TRIM simulation.

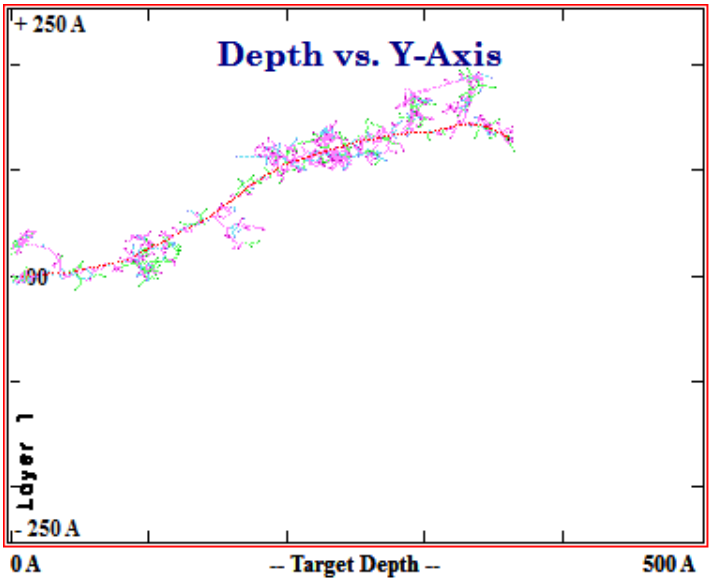

Figure 2.11. Collision cascade simulated by SRIM 2008 following the penetration of a single 30 keV Fe ion in amorphous strontium titanate: red dashed line denotes the primary ion's track; green, blue and pink lines represent trajectories of Sr, Ti and O recoil atoms, respectively.

2.1.6 Particle induced X-ray emission (PIXE)

When a high energy ion beam (typically, 1-4 MeV H^+) hits a target, it excites electrons from the inner atomic shells of the elements. The core hole is then filled with an electron from the upper shell, and the characteristic X-rays are emitted. PIXE as well as RBS analysis provides information about elemental composition of the material, but unlike the latter it does not show the depth distribution of elements because produced X-ray photons are attenuated but do not lose their energy in the solid on the way to the X-ray detector. However, peaks from the individual elements can overlap in RBS spectra which complicates detection of elements with close masses or light elements in a heavy matrix, whereas in PIXE spectral peaks from the individual elements are well identifiable. The main advantage of the PIXE method is that it is sensitive even to low concentration impurities at depths up to several micrometers.

The PIXE sensitivity to different elements varies depending on their position in periodic table, and the type of the detector used. The lowest limit-of-detection (LOD) is between atomic numbers 20 and 40 for K-shell (from Ca to Zr) and between 70 and 80 for L-shell (from Lu to Hg) [17]. The LOD curves for both K and L shells X-rays have generally U-shapes with respect to their atomic number. The characteristic X-rays of the

light elements (Z < 10) are too soft to be reliably detected because of the high absorption of the soft X-rays by materials. Though PIXE is not sensitive to the light elements, the method is suitable to probe the presence of heavy metals in a light target, for example in organic samples and polymers [17].

The intensity of X-ray peaks increases with the incident energy of the proton (cross section increases) but at the same time use of particles of higher energy leads to an increase of the underlying background contribution consisting of bremsstrahlung, nuclear reaction gamma rays and overlapping X-ray peaks. The complete equation for the intensity of PIXE peaks is rather complex. It takes into account the parameters of the experimental measuring system and the specimen properties. The yield *Y(Z)* of the principal characteristic X-ray ($K\alpha_1$ or $L\alpha_1$) depends in an intricate way on the initial ion energy E_0 and the concentration C_X of a particular element X but also on the energy losses of the ions and the attenuation of the emitted X-ray in the target material [17].

Though the PIXE method does not arguably allow an accurate quantitative analysis, some semi-quantitative information can be derived from the intensity of the X-ray peaks if a standard sample with the known concentration of element is used. The simplified formula of the intensity or yield for an element *X* is

$$Y_x = (N_x t) \times \sigma_x \times Q \times A_x \times \Omega_x \times \varepsilon_x , \qquad (2.13)$$

where $N_x t$ is the areal density of the element *X*, σ_x is the ionization cross section, Q is the fluorescent yield, A_x is the attenuation of the element *x*, Ω_x is the detector solid angle, and ε_x is its relative efficiency [1].

For a particular detector, we can consider that $Q_x \times \Omega_x \times \varepsilon_x = Const$ is constant. Then one can get the areal density of the element of interest by comparing it to the yield, Y_{SS} and the areal density, $N_{SS}t$, of the element in the standard sample (*SS*):

$$(N_x t) = \frac{Y_x \sigma_{SS} A_{SS}}{Y_{SS} \sigma_x A_x} (N_{SS} t) , \qquad (2.14)$$

Therefore quantification in PIXE relies on available standard samples with homogeneous distribution of elements of interest.

2.1.7 Ion production at the Tandetron accelerator facility

The Tandetron laboratory at Western University is equipped with a 1.7 MeV Tandem accelerator and several ion beam lines designed for material analysis and ion beam implantation (Fig. 2.12). The ion beam production includes a two-step acceleration process. It can be described using He ions as an example as follows. The initial positive ions He^+ are produced by the duoplasmatron source. Term "duoplasmatron" refers to the design of the ion source where plasma is accelerated through a series of at least two highly charged grids, and becomes an ion beam, moving at fairly high speed from the aperture of the device. As He^+ ions pass through a sodium vapour, they turn into He^-. Then the negative ions accelerate toward the high voltage terminal located in the middle of the "T"-shape tank. The nitrogen stripper gas removes electrons and converts negative ions He^- into positive ions He^+, which then are accelerated toward target.

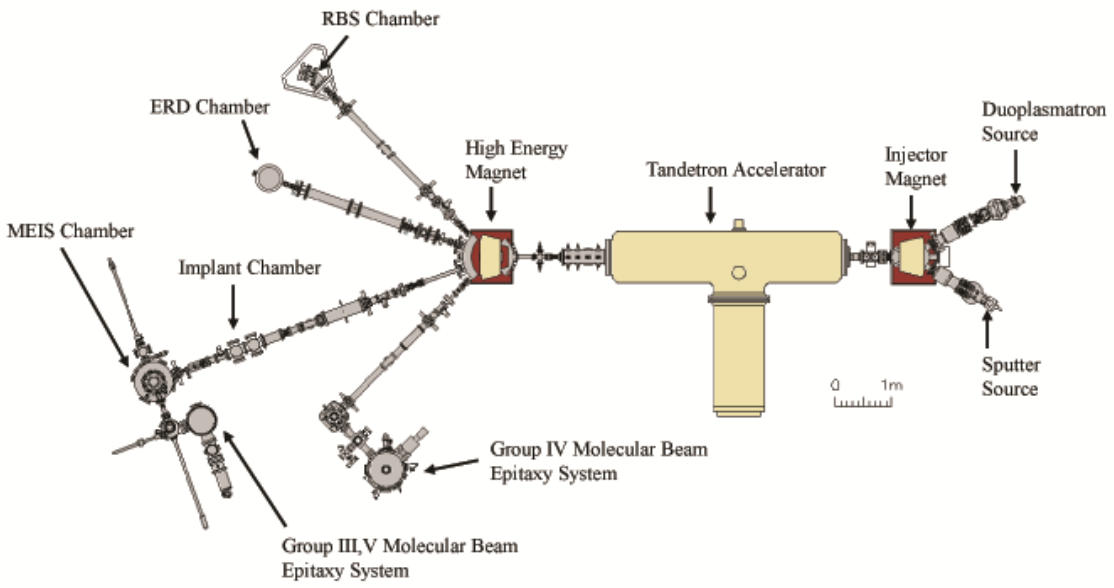

Figure 2.12. Schematic diagram of Tandetron facility (courtesy of J. Hendriks).

Calibration of the accelerator energy is important for RBS because it is related to the determination of the mass of the target atoms. The ability of the method to distinguish between atoms with close masses depends on the energy resolution of the produced ion beam. As a minor issue, the scattering cross section is proportional to the beam energy as $1/E^2$. Error in energy calibration will propagate in the energy resolution and thus in

determining the layer thickness. The same procedure is applied for producing other ions by using different targets in the sputtering source. The quadrupole triplet focuses the high-energy ion beam. High-energy switching magnet directs the ion beam into one of four beam lines: Rutherford backscattering (RBS) chamber, Elastic Recoil Detection (ERD) analysis chamber, Medium Energy Ion Scattering *(*MEIS) chamber, or Particle Induced X-ray Emission (PIXE) chamber. Implantation chamber is inserted in the MEIS beamline.

He and H beams used for material analysis can be collimated to ~0.5×0.1 mm^2 by a system of slits. Any secondary electrons that can be produced if the ion beam hits the aperture and target are suppressed by a bias voltage to provide correct ion beam charge measurements.

In the RBS chamber, a high precision 4-axis manipulator allows precise targeting of the sample (within ±0.1 mm and its orientation relative to the ion beam direction within ±0.1º). A surface barrier silicon detector (Ortec) measures the energy distribution of backscattered ions. It is located inside the chamber in Cornell geometry at 170º above the scattering plane [8]. The PIXE chamber is equipped with a Ge detector to analyze emitted characteristic X-rays. A Be window filter of 13 μm thickness positioned at an angle of 90^o relative to the incident beam is used to suppress the backscattered ions, which helps to reduce the background. The detector resolution is better than 150eV at 5.9 keV.

2.2 X-ray photoelectron spectroscopy

Absorption of a high energy photon leads to emission of optical and fluorescent photons and electrons (photoelectrons and Auger electrons) from the solid surface (Fig. 2.13), which gives rise to a number of analysis techniques: Photoluminescence Spectroscopy (PL), X-ray excited optical luminescence (XEOL), X-ray emission spectroscopy (XES), Auger electron spectroscopy (AES), and X-ray photoelectron spectroscopy (XPS). The last two are surface sensitive.

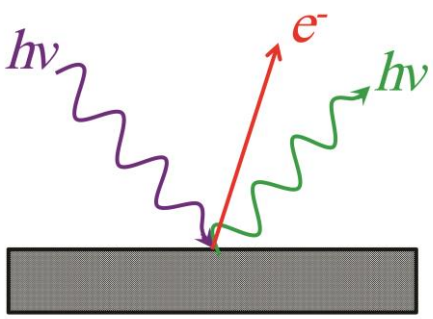

Figure 2.13 General interactions of a photon with a solid

X-ray Photoelectron Spectroscopy (XPS) is a photon in/electron out method. Typically, XPS uses soft X-ray sources (with $h\nu$ ~1200-1400 eV) to excite electrons from the core levels of atoms. If an electron with the binding energy E_b below the vacuum level absorbs a photon with energy $h\nu$, its escape kinetic energy is KE:

$$KE = h\nu - E_b - \phi, \qquad (2.15)$$

where ϕ is the work function of the surface. Both KE and E_b are referenced to the Fermi level of the solid. The elements present on the surface are determined by matching E_b to tabulated values of the core binding energies. As a core level spectroscopy, XPS spectra are dominated by atomic effects. The spectrum has a staircase structure due to inelastic electron scattering [18].

This simple picture is more complicate in practice because of the different probability of photons to be absorbed by the different electron states but in principle any photons with energy above the work function of the solid surface ($h\nu > \phi$) are suitable for photoelectron spectroscopy. The kinetic energy of electron in XPS experiment typically is in the range from few eV to 1000 eV. It is essentially surface sensitive technique because of the small escape length of electrons, which is much shorter than the penetration depth of photons. At this energy range, the escape length of electrons does not exceed 10 Å (Fig. 2.14), resulting in probing depth of 3-5nm [18].

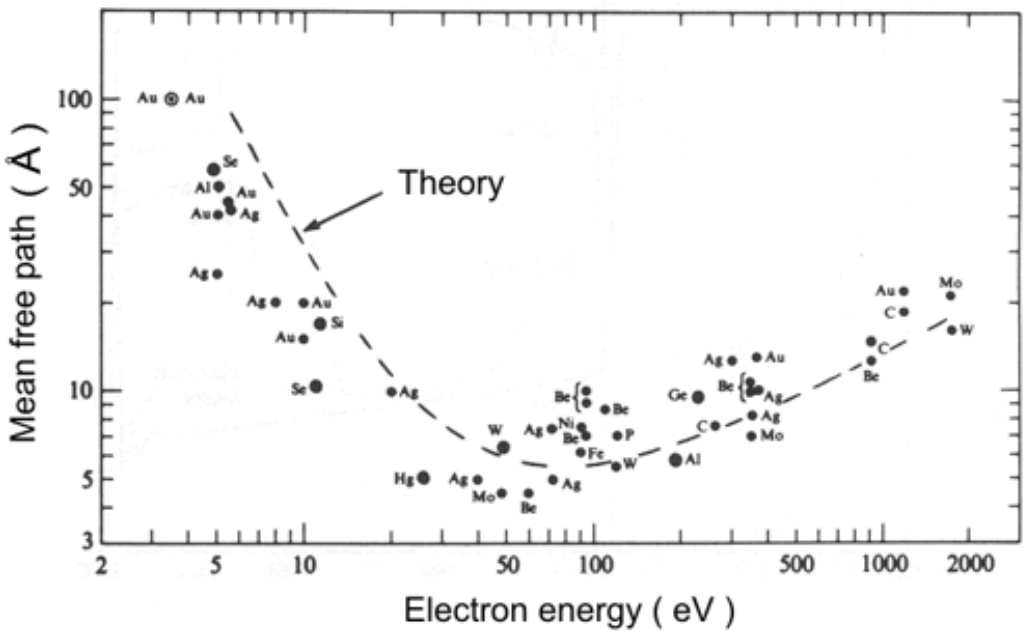

Figure 2.14. Mean free-path of electrons in solids. Reprinted with permission from Ref. [15].

The XPS method is sensitive to the elemental composition of the solid because the core levels are specific for each element. A typical XPS spectrum of a strontium titanate crystal is presented in Fig. 2.15. Besides Sr, Ti and O peaks, there are peaks of Cu and Si impurities, as well as Ar peaks because the surface of STO was modified by Ar sputtering.

Usually, metallic target sources of X-rays (Mg and Al with energy of 1486.6 eV and 1253.6 eV, respectively) are used in XPS experiments. The energy is enough to reach available levels of all materials. Use of higher energy X-rays can reduce surface sensitivity of the method. Tuning the incident energy of the photons to 25-100eV can enhance surface sensitivity but it reduces the number of the accessible levels [18].

Use of synchrotron sources for XPS provides further advantages. Synchrotron X-ray photon beams are more intense and their energy can be finely tuned to the photoionization threshold for a core level of interest of a particular element [19]. In such conditions, the emitted electrons have a kinetic energy around 25–100 eV. It improves the surface specificity, because the mean free path of electrons in matter has a broad

minimum in this energy range (Fig. 2.14) and provides better energy resolution in the electron spectrometer [15].

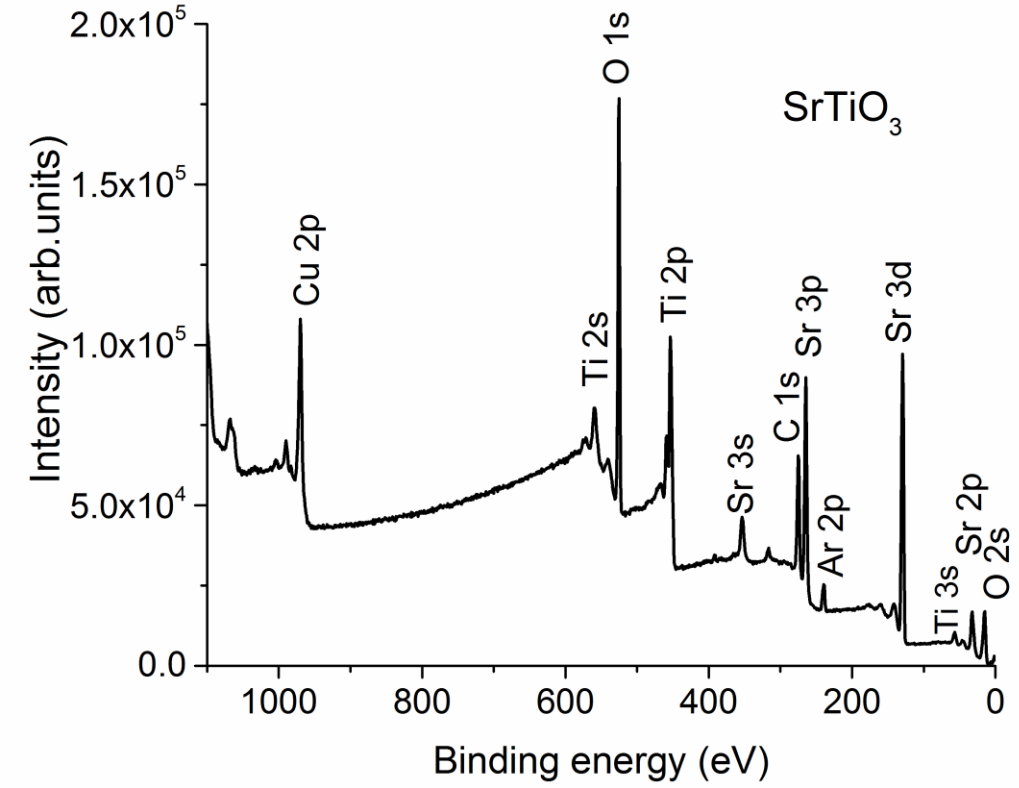

Figure 2.15. Survey XPS spectrum of strontium titanate surface cleaned by Ar sputtering. It shows peaks from Sr, Ti and O, as well as peaks from Cu, Si and Ar impurities.

As mentioned above, the kinetic energy of the emitted electrons is determined by the difference between the photon energy and the binding energy of the core electron (Eq. 2.14). In practice, the kinetic energy of the photoelectrons is always different, and the energy shift ΔE should be taken into account. The full expression for the kinetic energy KE is

$$KE = h\nu - E_b - \phi + \Delta E, \qquad (2.16)$$

There are several phenomena contributing to the energy shift ΔE. First of all, there are intrinsic and extrinsic processes associated with the photoemission itself and

with the transport of photoelectrons through the solid from emitter to the surface. The core hole created by photoionization causes other electrons to relax in energy to lower states providing more energy for the outgoing photoelectrons [18]. There is also the contribution of the solid environment when the atom is placed in or on solid surface. The situation is further complicated by creation of bulk and surface plasmons appearing as the inelastic tail after each photoemission peak [15].

Another source of shift of the emitted kinetic energy is associated with different local and electronic environment of elements in solid, so-called *chemical shifts*. This chemical shift originates from two effects: (i) change in the relaxation energy in the excited state, a final state effect, and (ii) the true chemical shift originated from the shift of the original binding energy in the changed electronic environment of the atom in ionic crystal, an initial state effect [18]. Extensive tabulations of the observed chemical shifts have been compiled to provide the references that allow us to identify the chemical state of the elements in a solid by the absolute position of XPS peaks [15, 20]. In most cases, however, the XPS binding energy shift measures the chemical effect on the core level associated with the chemical environment of the atom.

2.2.1 Depth profiling by sputtering

Since XPS is essentially a surface sensitive method, to get information about the depth distribution of the elements in the target, sputtering of the surface is required. When the incident ion beam hits a target surface, typically under grazing incident angle, it transfers energy to the target atoms which are recoiled with energy high enough to leave the surface. Sputtering yield (the number of emitted atoms per one incident ion) depends on the structure and composition of the target material, the incident ion beam parameters and the geometry of the experiment. The sputtering yield by heavy ions, such as Ar^+ or O^+, with energy in the range of 0.5–20 keV lies between 0.5 and 20, whereas for light ions with MeV energy it does not exceeds 10^{-3} ions per incident ion for most materials.

The probability of a sputtering event depends on the mass ratio of the incident and the target ions. Light elements are removed more easily from the surface than heavier

ones resulting in different sputtering rate of different elements. Thus, *preferential sputtering of oxygen* in oxide material leads to formation of an oxygen depletion area at the surface. As a result of this preferential sputtering the oxidation state of elements becomes different from that in the bulk of material.

2.3 X-ray absorption spectroscopy

X-ray absorption spectroscopy analyses material properties by studying the absorption of X-rays across an absorption edge. It uses synchrotron sources which produce X-ray photons in a wide, continuously tunable energy range from infrared to hard X-rays. Third generation synchrotron sources produce X-ray radiation that is extremely bright, intense, highly collimated and can be easily tuned to a specific energy [21]. X-ray spectroscopy is an element and oxidation state specific method because the electron energy levels are unique for every element. High energy resolution makes synchrotron radiation methods sensitive even to different polytype of the same element [22].

X-ray Absorption Fine Structure (XAFS) reflects the changes in the absorption coefficient with the excitation energy above an absorption edge. XAFS arises from the dipole transitions from core to unoccupied states. X-ray photon absorptions leads to core-to-bound, core-to-quasibound, and core-to-continuum electron transitions that decay via different pathways (Fig. 2.16) [23]. The core hole is created when the excitation energy approaches the threshold energy. The absorption threshold is the ionization energy of a shell of the atom. As the excitation energy exceeds the threshold, electrons can jump from the core level to unoccupied state above the Fermi level. With further increase of photon energy, the excited electron can pass into continuum with some positive kinetic energy (same process is used in XPS).

Absorption of X-ray photon leads to several processes including emission of photoelectrons and Auger electrons, and X-ray fluorescence [23]. Fluorescence photons, Auger and photoelectrons can transmit part of their energy through inelastic interactions to the matter, creating more holes and secondary electrons with low kinetic energy on their path out. Finally, as the result of the thermalization relaxation processes in the

semiconductor materials, the electron appears on the bottom of conductive band, and the hole – on the top of the valence band (or highest occupied molecular orbital (HOMO) and lowest unoccupied molecular orbital (LUMO) in molecular materials) [23]. The electron-hole pair recombination across the energy gap produces optical luminescence photon with energy close to that of the band gap in materials that have an efficient optical deexcitation channel.

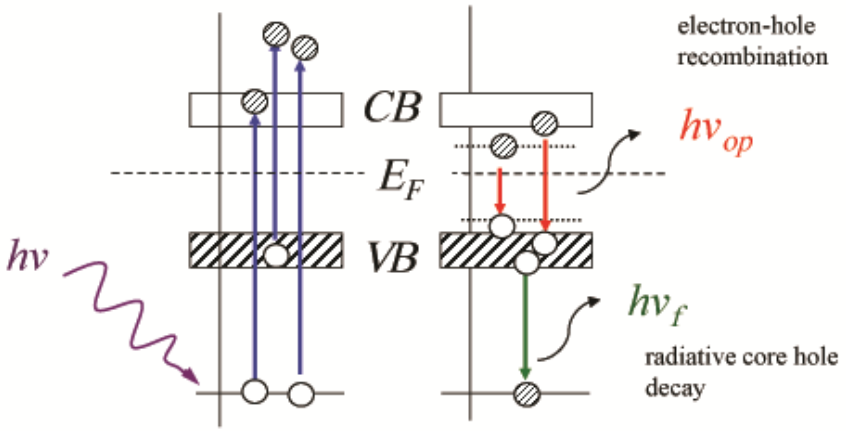

Figure 2.16. Electronic transitions caused by the absorption of X-ray photon absorption: left panel illustrates the creation of the core hole due to excitation of an electron, right panel shows radiative transitions of the cascade process that generates X-ray fluorescence (hv_f) and optical photons (hv_{op}).

2.3.1 X-ray Absorption Near Edge Structure and Extended X-ray Absorption Fine Structure

XAFS is somewhat arbitrarily divided into X-ray Absorption Near Edge Structure (XANES), which studies the near edge region of spectra (about 50 eV above the absorption edge), and Extended X-ray Absorption Fine Structure (EXAFS), which deals with the range from 50 eV to as much as 1000 eV above the absorption edge (Fig. 2.17). The scattering of the excited electrons on neighboring atoms produces fine structure on the dependence of absorption coefficient with the excitation energy. If the electron wave does not encounter another atom, the absorption coefficient $\mu(E)$ changes monotonically

with energy. Thus, absorption spectrum of the isolated atom (for example, in gas phase) does not show any fine structure above the absorption edge. In condensed matter the electron gets scattered by other atoms in the vicinity of the absorbing atom. The forward and backscattered waves interfere with each other, producing oscillation (modulation with constructive and destructive interference) in the absorption coefficient μ.

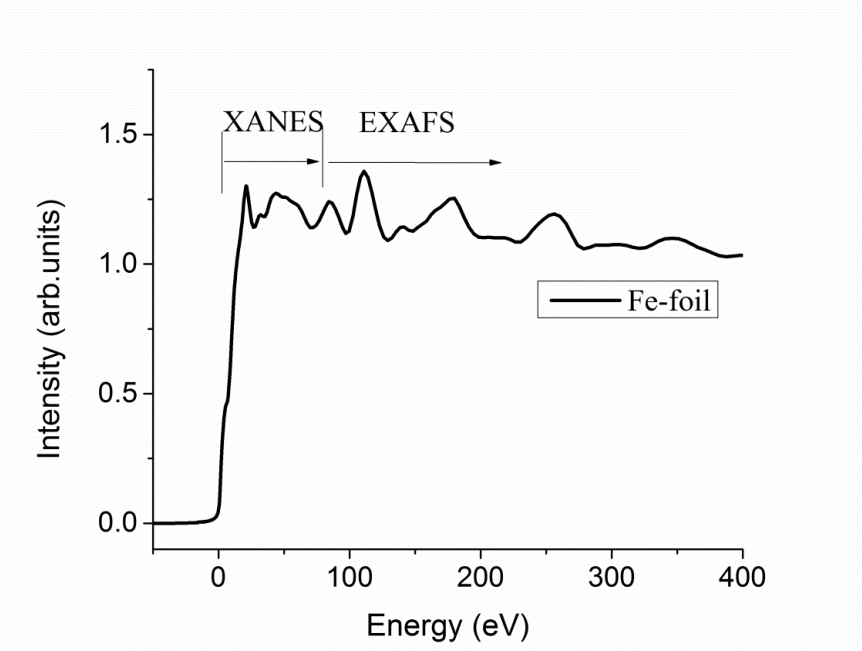

Figure 2.17. XANES and EXAFS parts of X-ray Absorption Fine Structure (XAFS) spectrum.

The XANES part of spectrum is created by photoelectrons with low kinetic energy which can be easily scattered by the surrounding atoms, and multiple scattering of electrons from the nearest neighbours dominates (Fig. 2.18(b)). XANES probes unoccupied densities of states associated with absorbing atoms above the Fermi level via bound to bound and bound to quasi-bound dipole transitions. It produces information about local symmetry and bonding in the material. It is sensitive to the chemical state of elements in compounds, and is often used as a "fingerprint" of a chemical type. XANES is a rather complicated phenomenon, and its interpretation is often semiquantitative at best.

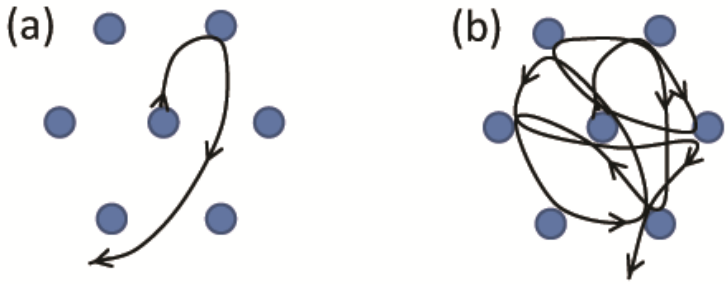

Figure 2.18. Single (a) and multiple (b) scattering processes.

In the EXAFS energy range, the rise of excitation energy leads to an increase in the kinetic energy of photoelectron, and single scattering process becomes dominating (Fig. 2.18(a)). The theory developed for the EXAFS process helps extract information about the magnitude of the scattering, the coordination number of neighbouring atoms, the interatomic distances and the local disorder (the Debye-Waller factor) [24]. In the EXAFS energy range, an electron with kinetic energy $E - E_o$ can be represented as a wave with k vector

$$k = \sqrt{\frac{2m(E - E_o)}{h}}, \qquad (2.17)$$

where E is the photon energy, and E_o is the threshold energy.

2.3.2 Detection modes in XAFS

Measurement of X-ray absorption can be implemented in several different detection modes depending on the nature of the analyzed sample.

For metal foils or thin samples direct measurement of the transmitted rays can be applied. When the incident X-ray beam of intensity I_o interacts with matter, it is partly scattered, partly absorbed by the material and partly transmitted through the sample (Figure 2.19).

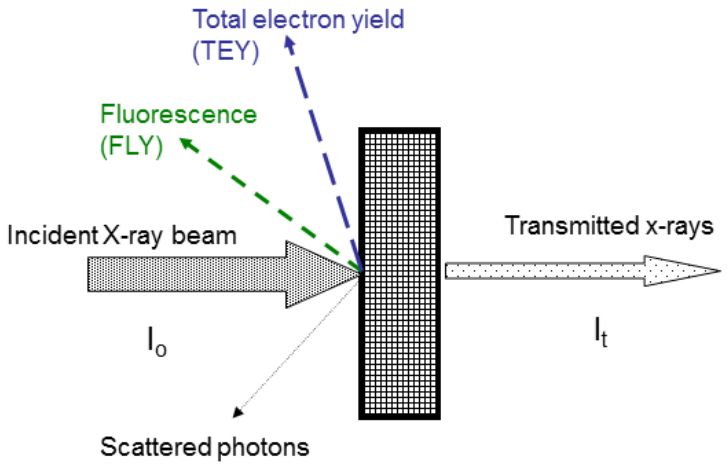

Figure 2.19. Interaction of the incident X-ray beam with sample of the thickness t.

The intensity of the transmitted beam *I*, is:

$$I_t = I_0 e^{-\mu t}, \qquad (2.18)$$

where μ is the absorption coefficient, and *t* is the sample thickness [25].

XAFS spectra are more often acquired by indirect measurement of total electron yield (TEY) and fluorescent yield (FLY). For thick and highly absorbing samples, the incident X-ray beam gets absorbed by the material completely. For soft X-rays, attenuation lengths of different materials can be on the order of 0.1 to 10 microns [26]. For example, at the Ti K-edge the attenuation length of X-rays in strontium titanate decreases from 16 to 10 μm.

The FLY mode measures the intensity of fluorescence, which arises from the de-excitation process of the core hole produced by an X-ray photon. TEY measurement registers electrons emitted by a sample as the result of X-ray photon absorption. The signal consists of photoelectrons and Auger electrons of all energies. Absorption of a single X-ray photon can generate several secondary electrons, because both photoelectrons and Auger electrons can generate the low energy secondary electrons through a process called thermalization in condensed matter solids [24]. Thus, TEY signal

consists mainly of electrons with low kinetic energies (below 20 eV) Such electrons have low mean free path in solid, which ensure that TEY XANES is the surface sensitive. It probes a near surface area, typically no more than 100 Å in depth [22]. The escape depth of the fluorescence photon is much larger than that of electron. Therefore, FLY reflects bulk absorption properties of the sample [22].

2.4 Superconducting Quantum Interference Device (SQUID) magnetometry

A superconducting quantum interference device (SQUID) combines the physical phenomena of flux quantization and the Josephson junction. In a closed superconducting loop, magnetic flux is quantized in the units of $h/2e = 2.07 \times 10^{-15}$ Wb [27]. A Josephson junction consists of two superconducting electrodes divided by an insulating layer. The supercurrent across the junction is:

$$I_s = I_c \sin\theta, \qquad (2.19)$$

where I_c is the maximal super-current, and θ is the phase difference of the superconducting wave functions of the two electrodes.

A SQUID works as a flux-to-voltage transducer. The principles of the method were invented in the middle 1960s and shortly after that appeared in laboratories for measurement of weak magnetic moments [28]. There are principal designs – direct current SQUID and radio frequency SQUID, consisting of two or one Josephson junctions, respectively (Fig. 2.20). Since then a number of improvements have been introduced. The method has become more sensitive, reliable, and quick-operating, with more sophisticated computer control which made acquisition completely programmed.

A SQUID system does not measure the magnetic moments directly but instead it reads the current excited in the superconducting loop (called a flux transformer) by the change of a magnetic flux threading the loop [29]. The actual SQUID sensor is placed away from the sample chamber sheltered in a niobium shield. The sensor is immersed in the liquid helium bath of the SQUID cryostat, whereas in the sample chamber the temperature can be increased up to 400 K (800 K in some models) during temperature-dependent experiments [27].

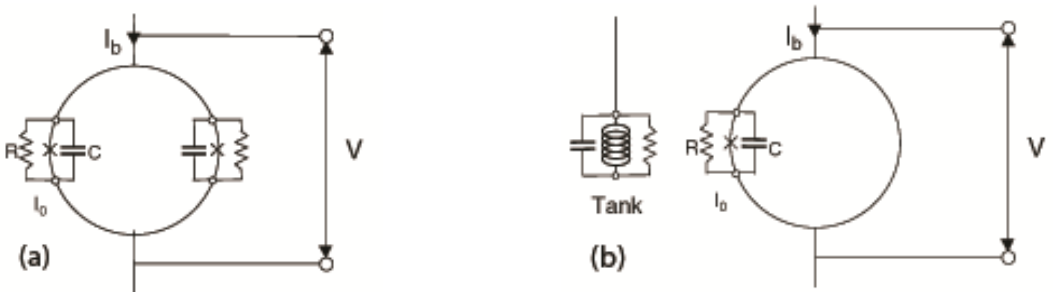

Figure 2.20. Schematic diagram of (a) dc SQUID and (b) rf SQUID. Adopted from Ref. [28].

A modern commercial magnetic property measurement system MPMS-SQUID magnetometer boasts a high sensitivity ($<1x10^{-8}$ emu at zero magnetic field) which has minimal variation over the operational frequency range from 0.1 Hz to 1 kHz. It allows measuring very low magnetic response of thin films, nanoparticles, nanodot arrays and dilute magnetic semiconductor samples deposited on a substrate. The level of the magnetism in such system often is comparable with the sensitivity of the magnetometer which in realistic experimental conditions is dominated by artifacts of about 10^{-7} emu [30]. At such low values of magnetic moments thorough cleaning and careful handling of samples become very important. Magnetic contaminations on the sample surface due to cutting and handling can lead to an overall ferromagnetic signal. Iron and its oxides were found responsible for the ferromagnetism of many commercial oxide substrates [31-35]. It should be noted that often the concentrations of the impurities are below detection level. Sometimes the contaminations reveal themselves by peculiar responses. Ney *et al*. judged the absence of true ferromagnetism using the temperature dependence of magnetization [30].

The pinned magnetic flux within the superconducting magnet (especially, at weak fields) can introduce distortion into measurements and result in "inverted" hysteresis observed for both net-diamagnetic and paramagnetic samples. Remanent field due to the trapped flux in the magnet can cause errors up to 1mT after large field changes. The magnet can be purified by sweeping the field several times with reduction of the field and use of the quench heater. It helps to reduce the trapped flux; however the method works only for operations at $H = 0$.

At high sensitivity of SQUID, the specimen itself can introduce artifacts into measured magnetic moments. When working with specimens consisting of nanostructures or thin layers on a relatively thick substrate, the absolute value of the magnetic moment can be of order of the system sensitivity. In such cases, special care should be taken during the experimental procedure and subsequent data analysis. For a composite sample consisting of a thin layer on a thick diamagnetic substrate, the diamagnetic component can be subtracted from the measured data. However the procedure is only adequate in the absence of paramagnetic impurities [29]. Sample size is usually limited to 5x5 mm^2, and symmetrical form is preferable because the measurement procedure requires the use of corrections factors, which have been calculated for objects of relatively high symmetry (spheres, squares, disks, etc.). The sample should be carefully centered within the gradiometer coils because it can affect a measured value. The centering is usually ensured by the sample holder. But for samples on a bulky substrate or crystals implanted on one side, the position of the substrate center may not coincide with the actual sample. The use of a drinking straw as a holder itself can introduce an additional signal due to indentation on its walls which can be diamagnetic (accumulation of material of the straw) or paramagnetic (lack of material) [29].

In summary, the application of several complimentary methods allows a comprehensive analysis of the material properties. Most of photon and particle techniques available for material analysis are virtually non-destructive and extremely sensitive even to small changes in samples. The combination of the different methods allows to trace structural and chemical changes in result of low dose ion irradiation and see how it affects the material properties.

References

[1] Y. Wang, M.A. Nastasi, Handbook of modern ion beam materials analysis, Materials Research Society, Warrendale, Pa, 2009.
[2] R.W. Kelsall, I.W. Hamley, M. Geoghegan, Nanoscale science and technology, John Wiley & Sons, Chichester, England ;; Hoboken, NJ, 2005.
[3] J.F. van der Veen, Ion beam crystallography of surfaces and interfaces, Surface Science Reports 5 (1985) 199-287.
[4] L.C. Feldman, J.W. Mayer, Fundamentals of surface and thin film analysis, North-Holland, New York, 1986.
[5] J.F. Ziegler, Helium : stopping powers and ranges in all elemental matter, Pergamon, New York, NY, 1977.
[6] J.F. Ziegler, J.P. Biersack, M.D. Ziegler, SRIM, the stopping and range of ions in matter, SRIM Co., Chester, Maryland, 2008.
[7] P. Sigmund, Particle penetration and radiation effects: general aspects and stopping of swift point charges, Springer, Berlin, New York, 2006.
[8] M. Mayer, SIMNRA Home Page, SIMNRA, Max-Planck-Institut für Plasmaphysik, 2011.
[9] W.K. Chu, J.R. Liu, Rutherford backscattering spectrometry: Reminiscences and progresses, Materials Chemistry and Physics 46 (1996) 183-188.
[10] L.C. Feldman, J.W. Mayer, S.T. Picraux, Materials analysis by ion channeling: submicron crystallography, Academic Press, New York ; Toronto, 1982.
[11] Y.T. Wang, X.L. Chen, L. Li, A. Shalimov, W. Tong, S. Prucnal, F. Munnik, Z.R. Yang, W. Skorupa, M. Helm, S.Q. Zhou, Structural and magnetic properties of irradiated SiC, J Appl Phys 115 (2014) 17C104.
[12] M. Ameen, I. Berry, W. Class, H.-J. Gossmann, L. Rubin, Ion Implantation, in: R. Doering, Y. Nishi (Eds.), Handbook of Semiconductor Manufacturing Technology, Second Edition, CRC Press, Boca Raton, London, New York, 2008, pp. 7-1–7-88.
[13] A. Meldrum, L.A. Boatner, W.J. Weber, R.C. Ewing, Amorphization and recrystallization of the ABO_3 oxides, J. Nucl. Mater. 300 (2002) 242-254.
[14] C. Sabathier, J. Chaumont, J.C. Krupa, Dose rate and temperature effects in radiation disorder creation in $SrTiO_3$, Nucl. Instrum. Methods Phys. Res. Sect. B-Beam Interact. Mater. Atoms 196 (2002) 308-314.
[15] Y. Zhang, J. Lian, C.M. Wang, W. Jiang, R.C. Ewing, W.J. Weber, Ion-induced damage accumulation and electron-beam-enhanced recrystallization in $SrTiO_3$, Phys Rev B 72 (2005) 094112.
[16] S. Soulet, J. Chaumont, C. Sabathier, J.C. Krupa, Irradiation-disorder creation in $SrTiO_3$, Journal of Materials Research 17 (2002) 9-13.
[17] S.A.E. Johansson, J.L. Campbell, K.G. Malmqvist, Particle-induced X-ray emission spectrometry (PIXE), Wiley, New York, 1995.
[18] D.P. Woodruff, T.A. Delchar, Modern techniques of surface science, Cambridge University Press, Cambridge ;; New York, 1994.
[19] D.T. Attwood, Soft x-rays and extreme ultraviolet radiation : principles and applications, Cambridge University Press, Cambridge ;; New York, 1999.
[20] A.V. Naumkin, NIST X-ray Photoelectron Spectroscopy Database, 2000.

[21] T.K. Sham, M.L. Rivers, A brief overview of synchrotron radiation, in: P.A. Fenter, M.L. Rivers, N.C. Sturchio, S.R. Sutton (Eds.), Applications of Synchrotron Radiation in Low-Temperature Geochemistry and Environmental Sciences, Mineralogical Soc America, Washington, 2002, pp. 117-147.
[22] T.K. Sham, Nanoparticles and nanowires: synchrotron spectroscopy studies, International Journal of Nanotechnology 5 (2008) 1194-1246.
[23] T.-K. Sham, R.A. Rosenberg, Time-Resolved Synchrotron Radiation Excited Optical Luminescence: Light-Emission Properties of Silicon-Based Nanostructures, ChemPhysChem 8 (2007) 2557-2567.
[24] S.C. Ray, J.W. Chiou, W.F. Pong, M.H. Tsai, The Electronic Properties of Nanomaterials Elucidated by Synchrotron Radiation–Based Spectroscopy, Critical Reviews in Solid State and Materials Sciences 31 (2006) 91-110.
[25] T.-K. Sham, Chemical applications of synchrotron radiation, World Scientific, River Edge, N.J., 2002.
[26] B.L. Henke, E.M. Gullikson, J.C. Davis, X-Ray Interactions: Photoabsorption, Scattering, Transmission, and Reflection at E = 50-30,000 eV, Z = 1-92, Atomic Data and Nuclear Data Tables 54 (1993) 181-342.
[27] J. Clarke, A.I. Braginski, The SQUID handbook, Wiley-VCH, Weinheim, 2004.
[28] V. Pizzella, S.D. Penna, C.D. Gratta, G.L. Romani, SQUID systems for biomagnetic imaging, Superconductor Science and Technology 14 (2001) R79-R114.
[29] M. Sawicki, W. Stefanowicz, A. Ney, Sensitive SQUID magnetometry for studying nanomagnetism, Semiconductor Science and Technology 26 (2011) 064006-064006.
[30] A. Ney, T. Kammermeier, V. Ney, K. Ollefs, S. Ye, Limitations of measuring small magnetic signals of samples deposited on a diamagnetic substrate, Journal of Magnetism and Magnetic Materials 320 (2008) 3341-3346.
[31] D.A. Crandles, B. DesRoches, F.S. Razavi, A search for defect related ferromagnetism in $SrTiO_3$, J Appl Phys 108 (2010) 053908.
[32] R. Salzer, D. Spemann, P. Esquinazi, R. Hohne, A. Setzer, K. Schindler, H. Schmidt, T. Butz, Possible pitfalls in search of magnetic order in thin films deposited on single crystalline sapphire substrates, Journal of Magnetism and Magnetic Materials 317 (2007) 53-60.
[33] S.M.M. Yee, D.A. Crandles, L.V. Goncharova, Ferromagnetism on the unpolished surfaces of single crystal metal oxide substrates, J Appl Phys 110 (2011) 033906.
[34] M. Khalid, A. Setzer, M. Ziese, P. Esquinazi, D. Spemann, A. Poeppl, E. Goering, Ubiquity of ferromagnetic signals in common diamagnetic oxide crystals, Phys Rev B 81 (2010) 214414.
[35] M.A. Garcia, E. Fernandez Pinel, J. de la Venta, A. Quesada, V. Bouzas, J.F. Fernandez, J.J. Romero, M.S. Martin-Gonzalez, J.L. Costa-Kramer, Sources of experimental errors in the observation of nanoscale magnetism, J Appl Phys 105 (2009) 013925.

Chapter 3. Overview of strontium titanate and graphite properties

Most of this thesis is related to the study of the structural, electronic and magnetic properties of strontium titanate single crystal and highly oriented pyrolytic graphite modified by the ion beam implantation method. Both materials have versatile technological applications, and have been widely investigated. Some of the relevant properties of these parental materials are reviewed in this chapter.

3.1 Strontium titanate: crystal structure and properties

Strontium titanate $SrTiO_3$ (or STO) is a technologically important material with exceptional chemical, thermal and radiation stability [1, 2]. It can be used in different areas such as gas sensors, photocatalysis, as substrate for high-T_C superconductors, and radioactive waste storage [2-8]. The high crystal symmetry also makes $SrTiO_3$ a convenient playground for theoretical modeling [9, 10].

3.1.1 Crystal structure of strontium titanate

Strontium titanate is one of a large family of perovskite oxides with formula $A^{2+}B^{4+}O_3^{2-}$ [11]. Pure parental material is diamagnetic and dielectric with high dielectric constant and indirect band gap of 3.25 eV which makes it a good insulator [12]. It has cubic structure with a lattice parameter of 3.905 Å, space group *Pm-3m* (Fig. 3.1). It transforms into a tetragonal structure at temperatures below 105 K. For perovskites, the crystal symmetry is determined by the ratio of the ionic radii (r_A, r_B and r_O) described by the Goldschmidt tolerance factor t [13].

$$t = \frac{(r_A + r_O)}{\sqrt{2}(r_B + r_O)} \qquad (3.1)$$

The closer the tolerance factor is to unity, the closer the structure is to the "ideal" cubic perovskite and the closer are the B-O-B bond angles to 180^o. For cubic $SrTiO_3$ t is equal to 1.002. With deviation of t from unity, lower symmetry is expected. For example, $CaTiO_3$ ($t = 0.97$) and $BaNiO_3$ ($t = 1.13$) have hexagonal structure. In some cases Jahn-

Teller distortion is observed. For instance, in $LaMnO_3$ ($t = 1.01$) the octahedra around Mn are rotated because of odd number of electrons on e_g orbitals of Mn ions (Fig. 3.2) [13].

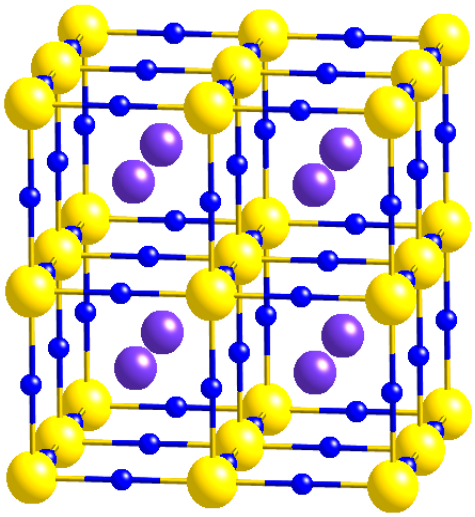

Figure 3.1. Cubic perovskite structure of ABO_3 compound: yellow, purple and blue spheres represent A ion, B ions and oxygen ions, respectively.

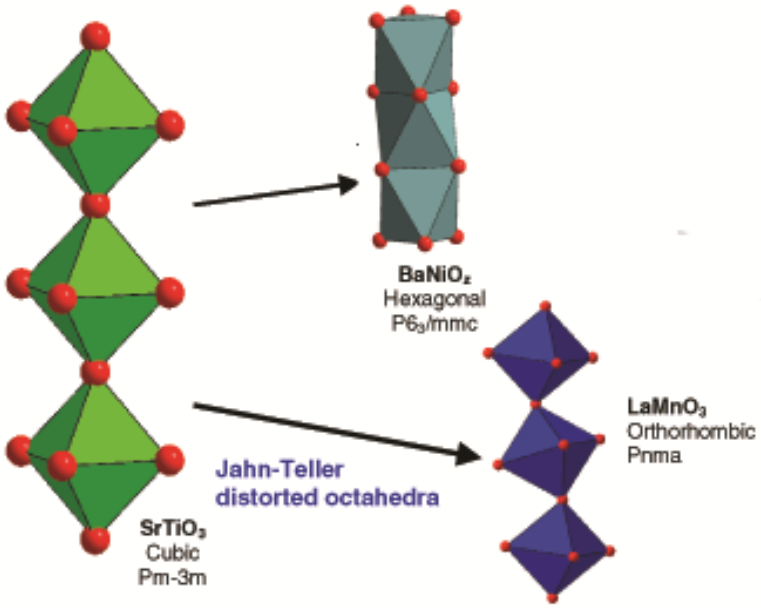

Figure 3.2. Deviation from ideal cubic structure of $SrTiO_3$ (tolerance factor t = 1) in other perovskite compounds due to differences in radii of A and B ions: hexagonal structure of $BaNiO_3$ (t > 1) and Jahn-Teller distortion in $LaMnO_3$ (t < 1) (modified from Ref. [13]).

Strontium ferrate, $SrFeO_x$ ($2.5 \le x \le 3$) with $t = 0.98$ has a tetragonal structure. It is an example of defect perovskite of which the structure is determined by oxygen vacancies because of mixed valences of iron ions. Some Fe ions in $SrFeO_x$ have oxidation state +3 and others +4, which lead to the formation of FeO_5 square pyramids [14]. Upon oxidation the tetragonal structure of defective $SrFeO_x$ is transformed to cubic perovskite structure [14].

Most studies of STO focus on properties of the low index surfaces. The most popular (001) surface features a number of morphologies, reconstructions and chemical compositions. If one looks down the <001> direction, STO crystal consists of alternating layers of TiO_2 and SrO. In principle, both arrangements can terminate the surface with equal probability [15, 16].

The top-most surface structure of STO is sensitive to the surface preparation. Thus argon sputtering or annealing at 830-1030°C can cause rearrangements of the surface with c(4×2) and (2×1) reconstructions [17, 18]. The surface reconstruction can be observed as an electron diffraction pattern which shows a combination of very bright bulk and relatively weak surface diffraction spots. To support the surface reconstruction a model was proposed where TiO_6 octahedra are tilted in the bulk layers underneath the surface. This model is in agreement with electron energy loss spectroscopy (EELS) study conducted by Zhu *et al.* [19] who showed that the topmost layer of STO is spaced at some distance from the crystal. Ti $L_{3,2}$-edge EEL spectra from different depth points inside the STO crystal are shown in Fig. 3.3(a). By collecting spectra at different locations of the sample with different thickness and assuming that the surface contribution is constant in all cases, they have been able to extract the signal from the surface. After extraction of surface and bulk contribution from the spectra, there is a clear peak shift (Fig. 3.3(b)). The authors have estimated the spacing between the topmost and subsurface layer to be (about 2.46 Å compare to bulk value of 1.9 Å) [19].

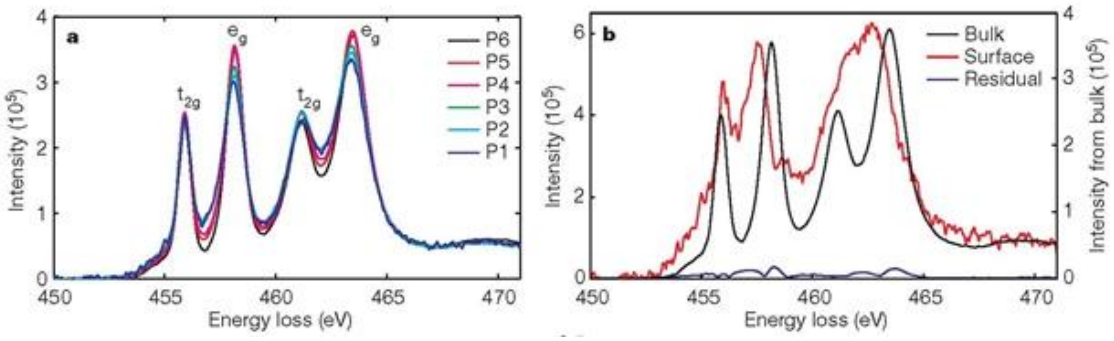

Figure 3.3. Ti L-edge Electron Energy Loss spectra of $SrTiO_3$: (a) EEL spectra collected at different depth of $SrTiO_3$ crystal; (b) the bulk and the surface contribution extracted from the experimental spectra. Adapted from Ref. [19].

3.1.2. Defects and properties of strontium titanate

Properties of strontium oxide can be significantly modified by the presence of oxygen vacancies and doping. Numerous studies report the appearance of metallic conductivity, photoluminescence, semiconducting or even superconducting and magnetic properties of strontium titanate induced by doping with transition metals and defects of crystal structure [20-31]. Vacancies and their complexes are common defects in STO crystals. Most favorable defects are single and double oxygen vacancies (V_o and V_{oo}). Oxygen vacancies form the defect states within the band gap. As followed from analysis of the band structure and the density of states, presence of the vacancies shifts the position of the Fermi level towards the more energetic states and increases the electrical conductivity due to mobility of oxygen within the STO crystal through the vacancy sites [10, 32, 33].

Oxygen vacancies can be produced during thin film fabrication, by reduction annealing in high-vacuum or by ion irradiation. Experiment on Ar ion-bombarded STO crystal showed formation of a highly conductive layer not only at room temperature but also at cryogenic temperatures where thermal diffusion was suppressed [20]. However, the conductivity measured in the experiment was lower than predicted by calculations because of the clustering of the oxygen vacancies in strontium titanate. A recent study has indicated that that most of the oxygen vacancies in $SrTiO_{3-\delta}$ are aggregated already at the amount of the vacancies $\delta < 0.01$ [34]. The first-principles calculations conducted by Liao *et al.* [33] for a 40 atom supercell with two missing oxygen ions have demonstrated that

chain alignment of oxygen vacancies is the most stable configuration. This tendency can reduce the electrical conductivity because the clusters of oxygen vacancies trap electrons.

Although V_O defects are responsible for the donor states in STO and able to give rise to conductivity, the free carrier concentration depends on the presence of other defects and doping [35]. In un-doped STO, the number of strontium vacancies can be comparable with the number of oxygen vacancies, and thus, they compensate the charge associated with the latter. In this case, defect states are mostly empty, and doping is required to fill the donor defect states to provide conductivity [10, 27]. In general, the concentration of defects depends on growth conditions [35].

3.1.3. Luminescent properties of strontium titanate

Another property closely related to the defect states is blue emission observed in doped STO at room temperature. Photoluminescence and cathodoluminescence studies show that pure and electron-doped STO can emit blue light at ~ 430 nm at room temperature when irradiated with Ar^+ ions [22, 23, 36]. Ion irradiation is known to produce oxygen vacancies and cause amorphization in the near-surface layer of the STO crystal. Electron doping can be achieved by ion doping (for example, substitution of La^{3+} on Sr^{2+} or Nb^{5+} on Ti^{4+} sites). Both processes lead to formation of defect states in the forbidden band of STO, which are responsible for the blue emission. When the temperature decreases below 160 K, a sharp band gap emission peak appears in STO spectra. With further decrease of temperature to 60 K, the broad defect peak gradually moves from blue to green (~ 530 nm). The defect emission has been also found in other perovskite materials such as $KTaO_3$, $BaTiO_3$, $LiNbO_3$, and $LiTaO_3$ after irradiation with Ar ions [36, 37].

Blue emission has been also observed in homo-epitaxial thin films of $SrTiO_{3-\delta}$ grown in oxygen-deficient conditions by conventional pulsed laser deposition and by molecular beam epitaxy methods under oxygen deficient conditions [22, 36]. The growth conditions and, consequently, the distribution of defects in STO films affect their emission properties. Kan *et al.* [22] have observed blue emission from the STO films at

room temperature, whereas Xu *et al.* [25] have reported photoluminescence in the red and blue regions of the spectrum.

3.2. Graphite: structure, properties, applications

Carbon exists in various allotropic forms with sp , sp^2 and sp^3 hybridized bonding between atoms. Graphite is the most thermodynamically stable phase at ambient conditions. Perfect graphite consists of layers with a honeycomb structure. Within in-plane layers, carbon atoms are strongly bonded by sp^2 hybridized orbitals forming the hexagonal network (σ states). The remaining out-of-plane p_z orbitals provide weak bonding between adjacent layers (π states). The layers can be stacked in hexagonal (ABA) or rhombohedral (ABC) arrangement (Fig. 3.4). The in-plane nearest neighbor distance is 1.421 Å, and the interplanar distance is 3.354 Å (for ABA arrangement, unit cell has an in-plane lattice constant 2.462 Å, and a c-axis lattice constant 6.708Å) [38].

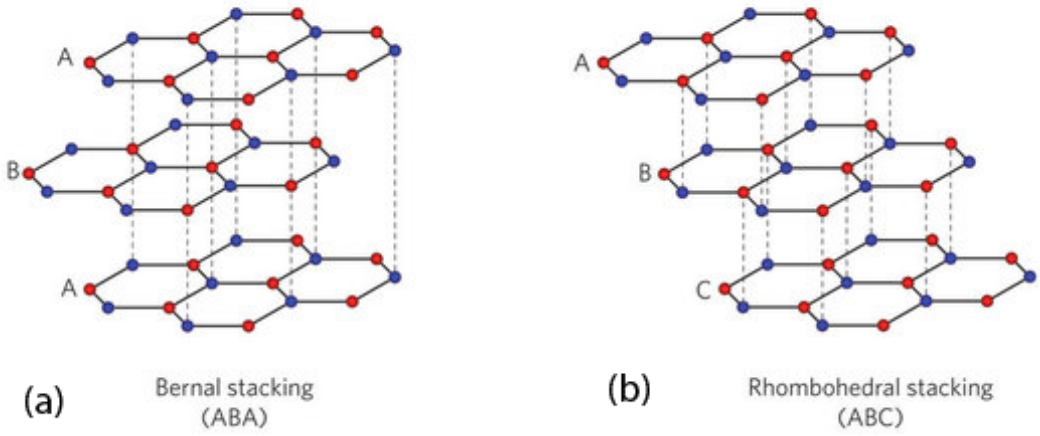

Figure 3.4. Structure of graphite: (a) ABA (Bernal stacking) and (b) ABC (Rhombohedral stacking) arrangement [37].

Properties of graphite are determined by strong in-plane bonding between atoms. Its structural anisotropy produces likewise anisotropic lattice, transport, optical and thermal properties [38]. Electronic and transport properties are determined by two π-bands lying close to the Fermi level. Graphite has a relatively good electric conductivity within the plane of the layers. The high in-plane tensile strength of graphite is used in

applications of carbon fibers in construction materials. Graphite as well as all other pure carbon allotropes is diamagnetic.

Crystal defects of graphite affect its electronic, optical, thermal, mechanical and magnetic properties [38]. Some quantity of defects is usually always present in crystals or they can be deliberately introduced into the crystal structure, for example, by ion irradiation or chemical treatment. Scattering of electron waves on defects reduces the electrical and thermal conductivity of graphite. Dopant atoms can further modify the electronic structure of graphite. Defects can improve mechanical properties of graphite which has inherently low shear strength. The amorphous layer created by ion irradiation increases the surface hardness of graphite [38]. Defect sites can be chemically functionalized by adatoms and different functional groups.

3.2.1 Defects in graphite materials

As graphite properties strongly depend on defects, let us consider some possible configurations that can be observed in its structure. Graphite can form a variety of structural defects. Because of the weak bonding between graphene layers in graphite, it easily splits and shears along the layers, and stacking disorder is very common. As a result, ideal graphite single crystals are usually very small (with lateral dimensions on a millimeter scale and with thickness on the order of several 0.1 mm). Due to high interplanar distances in graphite structure, interstitial atoms can be easily accommodated between graphite layers, and such defects can be very mobile [39].

The single isolated layer of graphite is called graphene. It is regarded as a basic construction element for other carbon structures. Point defects are convenient to consider on the example of graphene structure. A number of point defects can be formed within a graphene sheet despite strong sp^2 in-plane bonds between carbon atoms. The native and physically introduced defects have been experimentally observed using transmission electron microscopy and scanning tunneling microscopy [40].

Point defects. As a result of the in-plane rotation of carbon bonds**,** four hexagons transform into two pentagons and two heptagons. The resulting configuration is known as Stone-Wales (SW) defect (Fig. 3.5) [40]. The defect is unique to graphene layers.

However, because of the high formation energy (E_f = 5eV or 10eV if we consider that the transformation involves simultaneous movement of the two involved atoms), these defects have a low equilibrium concentration (at least at temperatures below 1000 ^{o}C).

Another point defect is a single vacancy V_1. One missing carbon atom leaves three unsaturated σ bonds. Jahn-Teller distortion leads to the saturation of two dangling bonds towards the missing atom, forming a 5-membered ring and a nine-membered ring (V_1(5-9)) (Fig. 3.5(b)). The presence of an under-coordinated carbon atom results in a high formation energy, E_f = 7.5 eV, which is higher than in many other materials (compare for example, E_f = 4 eV in Si). A single vacancy in a graphene sheet has a low migration barrier E_m=1.3eV which leads to high mobility of the defects already at moderate temperature (100-200ºC).

Two missing atoms produce the double vacancy. Figure 3.5(c) shows V_2(5-8-5) defect. Actually several surface configurations are possible for double vacancies with very close formation energies from 7 eV to 8 eV. The activation barrier of migration of double vacancies is ~7 eV (compare to 1.5 eV for single vacancy), which makes V_2 defects practically immobile [40].

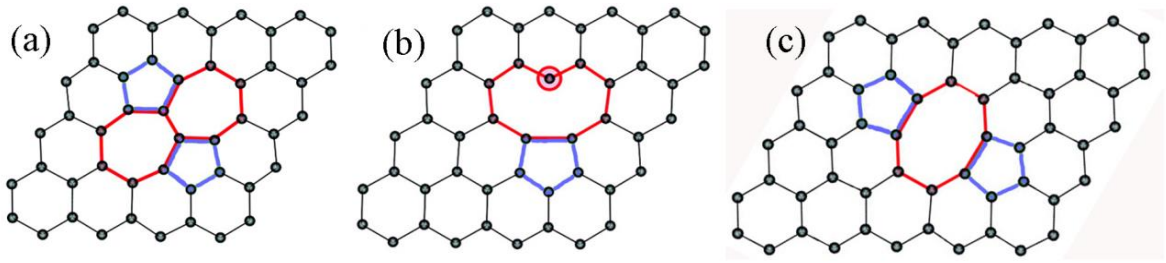

Figure 3.5. Point defects in a graphite layer: (a) Stone-Wales defect SW(55-77), formed by rotating a carbon-carbon bond by 90°; (b) single vacancy V_1(5-9); (c) Double vacancy V_2(5-8-5). Redrawn with permission from Ref. [40].

Nanoholes. Due to the high mobility of single vacancies in a graphene sheet, there is a high probability for aggregation of the defects. The formation of nanoholes within a graphene layer is more energetically preferable than complex surface reconstructions. They are more stable than complex multi-vacancy defects [39]. Cui *et al.* [41] have calculated formation energies of nanosize holes with different numbers of missing carbon atoms. Figure 3.6 shows the formation energy per vacancy *versus* number of missing

carbon atoms, n, considering the most compact form of the hole. The formation energy E_f decreases with increase of nanohole size, and there are local minima for n=4 and n=28. On the whole, a hole in graphene exhibits the complex behaviour of atoms at a boundary. Experiments show that carbon atoms have high mobility along the hole edges, and they tend to form a zigzag arrangement which is more stable compared to the arm-chair one [42].

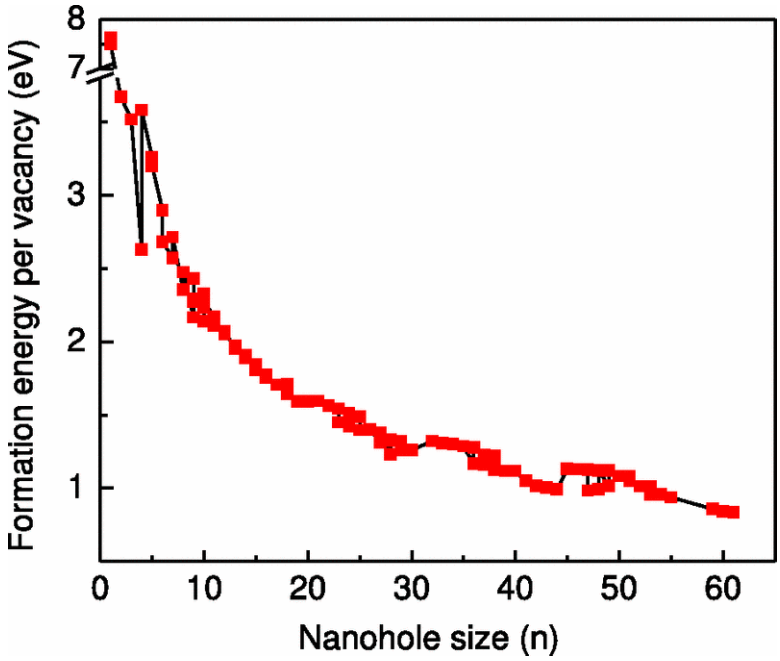

Figure 3.6. Formation energy per vacancy as a function of the nanohole size. The size is measured as the number n of vacancies that constitute the nanoholes. Adapted from Ref. [41].

Adatoms on the graphene layer. Another point defect is carbon adatoms. There are two energetically favored positions: (a) bridge configuration (Fig. 3.7(a)), and (b) dumbbell configuration (Fig. 3.7(b)). Adatoms tends to migrate (the migration barrier is about 0.4 eV) along the surface hopping from one configuration to another.

Foreign atoms can be present on graphite surface as adatoms or substitute carbon atoms and be incorporated into graphene sheet. The weak van der Waals interaction leads to physisorption, stronger interaction – to covalent bonding. If foreign atom meets structural defects, it can form a substitutional impurity. The foreign atoms can be trapped by vacancy defects on the surface forming stable configurations. Possible configurations

of foreign adatoms built into a single vacancy and into a double vacancy are shown in Fig 3.7(c) and in Fig 3.7(d), respectively.

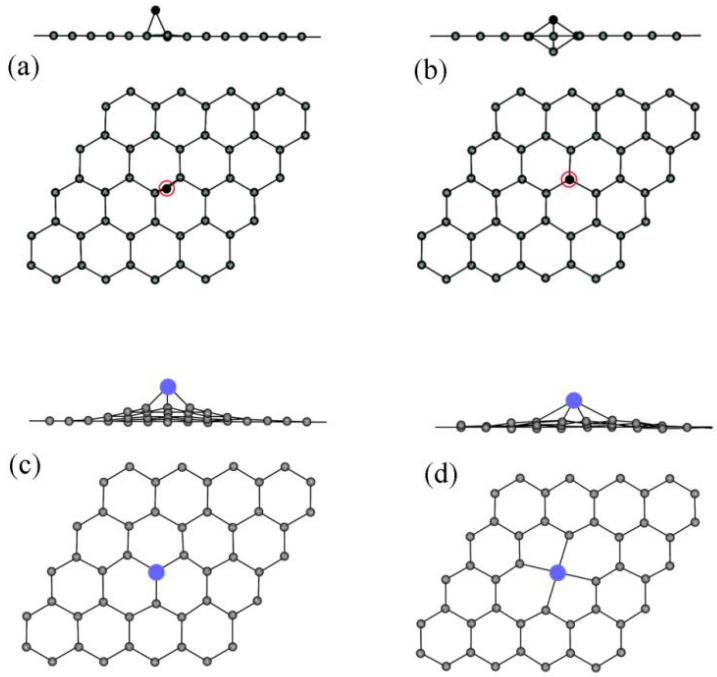

Figure 3.7. Atomic configurations of adatoms on the graphite surface. Carbon adatoms: (a) single carbon adatom in the bridge configuration; (b) single carbon adatom in the dumbbell configuration; (c) typical configuration of metal adatom adsorbed on single vacancy; and (c) typical configuration of metal adatom adsorbed on double vacancy. Side view shows that all the configurations are non-flat. The small dark circles denote carbon atoms; big (blue) lighter circles correspond to metal atoms. Redrawn with permission from Ref. [40].

3.2.2. Defects induced by ion irradiation.

Ion implantation is a convenient method to study defects and their influence on graphite properties, because the method allows some level of control of the concentration and distribution of defects [43-52]. Density functional theory (DFT) was used to study defects in 2D graphene sheet irradiated with noble gas ions (He, Ne, Ar, Kr, and Xe) in a wide range of energies (from 10 eV to 10^6 eV) [44]. Calculation results showed that ion bombardment should produce mostly single and double vacancies, though the probability to create complex defects increased with increasing incident ion energy (E > 10 keV). However in graphite self-annealing effects must be taken into account because they lead to partial healing of irradiation damage. Ahlgren et al. [45] studied the possibility of

incorporating foreign ions of different energies into the plane of the graphene sheet. As it followed from classical molecular dynamics simulations and DFT total energy calculations there is a higher possibility for nitrogen (N) and boron (B) atoms to be incorporated into the graphene sheet or stay on the surface as an adatom than to create other defect combinations. The probability of ions to form a perfect substitution in a graphene sheet has a sharp peak in low energy range. Authors calculated that there is 55 % probability for N and 40 % probability for B to substitute carbon atoms in graphene sheet (Fig. 3.8(a)). The probability to form adatom defects on the graphene surface rapidly decreases with incident ion energy and becomes zero for the incident ions with energy higher than 70eV (Fig. 3.8(b)) [45].

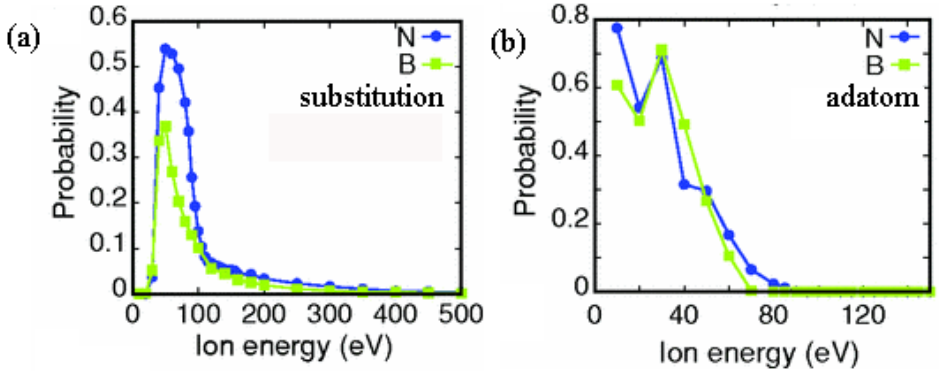

Figure 3.8. Irradiation of graphene sheet with N and B ions: probabilities for different defect configurations as functions of the ion energy: (a) perfect substitution; (b) dopant as an adatom on top of the graphene sheet. Adapted from Ref. [45].

3.2.3. Catalytic properties of defective graphite

Defective carbon materials are interesting for their catalyst applications. Carbon-based materials are very attractive as a cheap and environmentally friendly replacement of costly platinum catalysts. They can be used in different fields including hydrocarbon conversion, chemical production, fuel cells, and solar energy in a variety of catalytic processes including gas phase, liquid phase, oxygen reduction, and photocatalytic reactions [53-56].

Catalytic activity of the surface defects can be increased by oxygen and nitrogen heteroatoms and functional groups. Heteroatoms (O, N, H, Cl, S etc.) can be intentionally

doped into carbon materials during fabrication by using appropriate precursors or by ion implantation. O function groups can be formed inadvertently when carbon material is exposed to the atmosphere. Chemical and thermal treatment can be used to change concentrations of the functional groups. Figure 3.9 shows nitrogen and oxygen groups that can be found on a carbon surface. They include carboxyl-, carbonyl-, ether-, and phenolic-type oxygen functionalities and doped N functionalities [52].

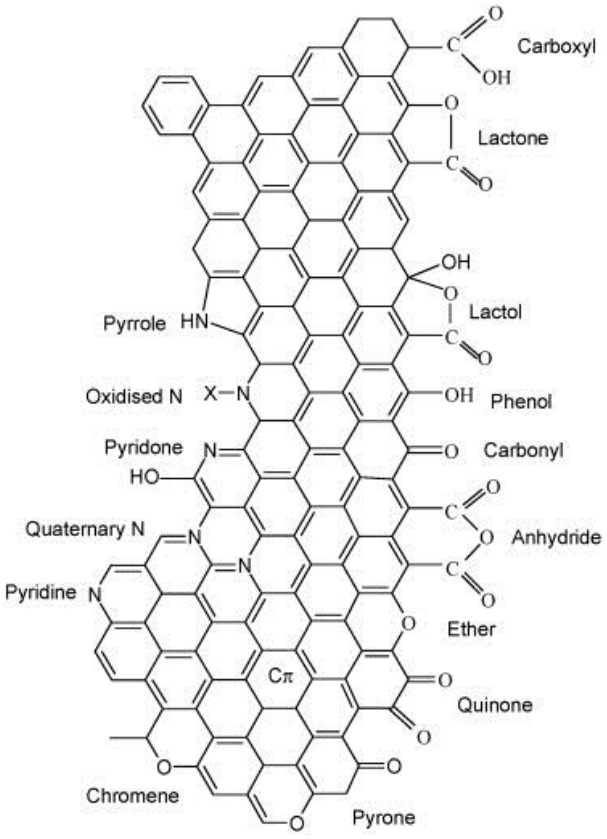

Figure 3.9. Nitrogen and oxygen groups on the surface of graphite [55].

These sites have different activity for surface reactions compared to a pure graphite surface. For instance, carboxylic acid groups have been identified as active sites for dehydration of alcohols [55, 57]. Basic sites, such as pyrone and chromene sites, can be used for NO oxidation [55]. N-containing groups in activated carbon have a high capacity for adsorption and further oxidation of SO_2 to SO_3 [58]. Nitrogen doped carbon materials can be used as non-Pt catalysts in fuel cell anodes [46, 59-61]. N is able to catalyze the oxygen reduction reactions through oxygen adsorption on the carbon atoms

adjacent to the nitrogen dopant in the carbon matrix. Calculations show that nitrogen doped into basal planes of graphite has higher activity than N in the edge of graphene layers because of the larger number of available doping sites [60].

In summary, the review of the recent research done in this field showed that properties of strontium titanate and graphite can be tailored by suitable doping and by careful structure control. Ion beam implantation is one of the methods routinely used not only to introduce doping but also to modify the crystal structure. The method allows convenient control of experimental parameters, and well-developed theoretical foundations enable simulations of the ion irradiation effect on the crystal structure. In strontium titanate, structural defects have been found to change electrical, magnetic and emission properties. The early theoretical predictions of defect-induced magnetism in both oxide and carbon based materials promote great interest to studies of influence of defects on their properties. Hence the next chapters of this thesis will be dedicated to the ion-beam modification of strontium titanate and graphite, and investigations of the structural and magnetic properties.

References

[1] Y. Zhang, J. Lian, C.M. Wang, W. Jiang, R.C. Ewing, W.J. Weber, Ion-induced damage accumulation and electron-beam-enhanced recrystallization in $SrTiO_3$, Phys Rev B 72 (2005) 094112.

[2] A. Meldrum, L.A. Boatner, W.J. Weber, R.C. Ewing, Amorphization and recrystallization of the ABO_3 oxides, J. Nucl. Mater. 300 (2002) 242-254.

[3] R. Moos, N. Izu, F. Rettig, S. Reiss, W. Shin, I. Matsubara, Resistive Oxygen Gas Sensors for Harsh Environments, Sensors 11 (2011) 3439-3465.

[4] F. Napolitano, A.L. Soldati, J. Geck, D.G. Lamas, A. Seyquis, Electronic and structural properties of $La_{0.4}Sr_{0.6}Ti_{1-y}Co_yO_{3\pm\delta}$ electrode materials for symmetric SOFC studied by hard X-ray absorption spectroscopy, International Journal of Hydrogen Energy 38 (2013) 8965-8973.

[5] A. Kosola, M. Putkonen, L.S. Johansson, L. Niinisto, Effect of annealing in processing of strontium titanate thin films by ALD, Applied Surface Science 211 (2003) 102-112.

[6] L.V. Goncharova, D.G. Starodub, E. Garfunkel, T. Gustafsson, V. Vaithyanathan, J. Lettieri, D.G. Schlom, Interface structure and thermal stability of epitaxial $SrTiO_3$ thin films on Si(001), Journal of Applied Physics 100 (2006) 014912-014912.

[7] C. Aruta, J. Zegenhagen, B. Cowie, G. Balestrino, G. Pasquini, P.G. Medaglia, F. Ricci, D. Luebbert, T. Baumach, E. Riedo, L. Ortega, R. Kramer, J. Albrecht, Structure of superconducting $[BaCuO_x]_2/\ [CaCuO_2\ ]_n$ superlattices on $SrTiO_3$(001) investigated by X-ray scattering, Phys. Status Solidi A-Appl. Mat. 183 (2001) 353-364.

[8] H. Liu, H. Dong, X. Meng, F. Wu, First-principles study on strontium titanate for visible light photocatalysis, Chemical Physics Letters 555 (2013) 141-144.

[9] C.X. Yang, T.Y. Liu, Z.J. Cheng, H.X. Gan, J.Y. Chen, Study on Mn-doped $SrTiO_3$ with first principle calculation, Physica B 407 (2012) 844-848.

[10] M. Djermouni, A. Zaoui, S. Kacimi, B. Bouhafs, Vacancy defects in strontium titanate: Ab initio calculation, Computational Materials Science 49 (2010) 904-909.

[11] R.W.G. Wyckoff, Crystal structures, Interscience Publishers, New York, 1963.

[12] K. van Benthem, C. Elsasser, R.H. French, Bulk electronic structure of $SrTiO_3$: Experiment and theory, J Appl Phys 90 (2001) 6156-6164.

[13] M. Johnsson, P. Lemmens, Perovskites and thin films - crystallography and chemistry, Journal of Physics-Condensed Matter 20 (2008) 264001-264001.

[14] P. Adler, S. Eriksson, Structural properties, Mossbauer spectra, and magnetism of perovskite-type oxides $SrFe_{1-x}Ti_xO_{3-y}$, Z Anorg Allg Chem 626 (2000) 118-124.

[15] P.A.W. van der Heide, Q.D. Jiang, Y.S. Kim, J.W. Rabalais, X-ray photoelectron spectroscopic and ion scattering study of the $SrTiO_3$(001) surface, Surf. Sci. 473 (2001) 59-70.

[16] J.D. Baniecki, M. Ishii, K. Kurihara, K. Yamanaka, T. Yano, K. Shinozaki, T. Imada, K. Nozaki, N. Kin, Photoemission and quantum chemical study of $SrTiO_3$(001) surfaces and their interaction with CO_2, Phys Rev B 78 (2008) 195415.

[17] N. Erdman, O. Warschkow, M. Asta, K.R. Poeppelmeier, D.E. Ellis, L.D. Marks, Surface structures of $SrTiO_3$ (001): A TiO_2-rich reconstruction with a c(4 x 2) unit cell, Journal of the American Chemical Society 125 (2003) 10050-10056.

[18] N. Erdman, K.R. Poeppelmeier, M. Asta, O. Warschkow, D.E. Ellis, L.D. Marks, The structure and chemistry of the TiO_2-rich surface of $SrTiO_3$(001), Nature 419 (2002) 55-58.
[19] G.-z. Zhu, G. Radtke, G.A. Botton, Bonding and structure of a reconstructed (001) surface of $SrTiO_3$ from TEM, Nature 490 (2012) 384-387.
[20] H. Gross, N. Bansal, Y.-S. Kim, S. Oh, In situ study of emerging metallicity on ion-bombarded $SrTiO_3$ surface, J Appl Phys 110 (2011) 073704.
[21] M.D. Drahus, P. Jakes, E. Erdem, R.-A. Eichel, Defect structure of the mixed ionic-electronic conducting $Sr[Ti,Fe]O_x$ solid-solution system - Change in iron oxidation states and defect complexation, Solid State Ionics 184 (2011) 47-51.
[22] D.S. Kan, T. Terashima, R. Kanda, A. Masuno, K. Tanaka, S.C. Chu, H. Kan, A. Ishizumi, Y. Kanemitsu, Y. Shimakawa, M. Takano, Blue-light emission at room temperature from Ar+-irradiated SrTiO3, Nature Materials 4 (2005) 816-819.
[23] D. Kan, R. Kanda, Y. Kanemitsu, Y. Shimakawa, M. Takano, T. Terashima, A. Ishizumi, Blue luminescence from electron-doped $SrTiO_3$, Appl Phys Lett 88 (2006) 191916.
[24] Y. Yamada, Y. Kanemitsu, Band-edge luminescence from $SrTiO_3$: No polaron effect, Thin Solid Films 520 (2012) 3843-3846.
[25] W. Xu, J. Yang, W. Bai, K. Tang, Y. Zhang, X. Tang, Oxygen vacancy induced photoluminescence and ferromagnetism in $SrTiO_3$ thin films by molecular beam epitaxy, J Appl Phys 114 (2013) 154106.
[26] D. Choudhury, S. Mukherjee, P. Mandal, A. Sundaresan, U.V. Waghmare, S. Bhattacharjee, R. Mathieu, P. Lazor, O. Eriksson, B. Sanyal, P. Nordblad, A. Sharma, S.V. Bhat, O. Karis, D.D. Sarma, Tuning of dielectric properties and magnetism of $SrTiO_3$ by site-specific doping of Mn, Phys Rev B 84 (2011) 125124.
[27] M. Valant, T. Kolodiazhnyi, I. Arcon, F. Aguesse, A.-K. Axelsson, N.M. Alford, The Origin of Magnetism in Mn-Doped $SrTiO_3$, Advanced Functional Materials 22 (2012) 2114-2122.
[28] E.N. Dulov, N.G. Ivoilov, O.A. Strebkov, L.R. Tagirov, V.I. Nuzhdin, R.I. Khaibullin, S. Kazan, F.A. Mikailzade, Magnetic phase composition of strontium titanate implanted with iron ions, Materials Research Bulletin 46 (2011) 2304-2307.
[29] W. Zhang, H.-P. Li, W. Pan, Ferromagnetism in Electrospun Co-doped $SrTiO_3$ Nanofibers, Journal of Materials Science 47 (2012) 8216-8222.
[30] Z.Q. Liu, W.M. Lu, S.L. Lim, X.P. Qiu, N.N. Bao, M. Motapothula, J.B. Yi, M. Yang, S. Dhar, T. Venkatesan, Ariando, Reversible room-temperature ferromagnetism in Nb-doped $SrTiO_3$ single crystals, Phys Rev B 87 (2013) 220405.
[31] Y. Zhang, J. Hu, E. Cao, L. Sun, H. Qin, Vacancy induced magnetism in $SrTiO_3$, Journal of Magnetism and Magnetic Materials 324 (2012) 1770-1775.
[32] M. Choi, F. Oba, Y. Kumagai, I. Tanaka, Anti-ferrodistortive-Like Oxygen-Octahedron Rotation Induced by the Oxygen Vacancy in Cubic $SrTiO_3$, Adv Mater 25 (2013) 86-90.
[33] X.-X. Liao, H.-Q. Wang, J.-C. Zheng, Tuning the Structural, Electronic, and Magnetic Properties of Strontium Titanate Through Atomic Design: A Comparison Between Oxygen Vacancies and Nitrogen Doping, Journal of the American Ceramic Society 96 (2013) 538-543.

[34] F. Cordero, Hopping and clustering of oxygen vacancies in $SrTiO_3$, Materials Science and Engineering A-Structural Materials Properties Microstructure and Processing 521-22 (2009) 77-79.
[35] E. Ertekin, V. Srinivasan, J. Ravichandran, P.B. Rossen, W. Siemons, A. Majumdar, R. Ramesh, J.C. Grossman, Interplay between intrinsic defects, doping, and free carrier concentration in $SrTiO_3$ thin films, Phys Rev B 85 (2012) 195460.
[36] Y. Yamada, Y. Kanemitsu, Photoluminescence spectra of perovskite oxide semiconductors, Journal of Luminescence 133 (2013) 30-34.
[37] A. Yacoby, GRAPHENE Tri and tri again, Nat. Phys. 7 (2011) 925-926.
[38] M.S. Dresselhaus, R. Kalish, Ion implantation in diamond, graphite, and related materials, Springer-Verlag, Berlin ;; New York, 1992.
[39] R.H. Telling, M.I. Heggie, Radiation defects in graphite, Philos. Mag. 87 (2007) 4797-4846.
[40] F. Banhart, J. Kotakoski, A.V. Krasheninnikov, Structural Defects in Graphene, Acs Nano 5 (2011) 26-41.
[41] X.Y. Cui, R.K. Zheng, Z.W. Liu, L. Li, B. Delley, C. Stampfl, S.P. Ringer, Magic numbers of nanoholes in graphene: Tunable magnetism and semiconductivity, Phys Rev B 84 (2011) 125410.
[42] C.O. Girit, J.C. Meyer, R. Erni, M.D. Rossell, C. Kisielowski, L. Yang, C.-H. Park, M.F. Crommie, M.L. Cohen, S.G. Louie, A. Zettl, Graphene at the Edge: Stability and Dynamics, Science 323 (2009) 1705-1708.
[43] P. Esquinazi, D. Spemann, R. Hohne, A. Setzer, K.H. Han, T. Butz, Induced magnetic ordering by proton irradiation in graphite, Physical Review Letters 91 (2003) 227201.
[44] O. Lehtinen, J. Kotakoski, A.V. Krasheninnikov, A. Tolvanen, K. Nordlund, J. Keinonen, Effects of ion bombardment on a two-dimensional target: Atomistic simulations of graphene irradiation, Phys Rev B 81 (2010) 153401.
[45] E.H. Ahlgren, J. Kotakoski, A.V. Krasheninnikov, Atomistic simulations of the implantation of low-energy boron and nitrogen ions into graphene, Phys Rev B 83 (2011) 115424.
[46] P.O. Lehtinen, A.S. Foster, Y.C. Ma, A.V. Krasheninnikov, R.M. Nieminen, Irradiation-induced magnetism in graphite: A density functional study, Physical Review Letters 93 (2004) 187202.
[47] R. Hohne, P. Esquinazi, V. Heera, H. Weishart, A. Setzer, D. Spemann, The influence of iron, fluorine and boron implantation on the magnetic properties of graphite, J Magn Magn Mater 320 (2008) 966-977.
[48] X.M. Yang, H.H. Xia, X.B. Qin, W.F. Li, Y.Y. Dai, X.D. Liu, M.W. Zhao, Y.Y. Xia, S.S. Yan, B.Y. Wang, Correlation between the vacancy defects and ferromagnetism in graphite, Carbon 47 (2009) 1399-1406.
[49] M.A. Ramos, J. Barzola-Quiquia, P. Esquinazi, A. Munoz-Martin, A. Climent-Font, M. Garcia-Hernandez, Magnetic properties of graphite irradiated with MeV ions, Phys Rev B 81 (2010) 214404.
[50] X.M. Yang, Z.T. He, W.F. Li, H.H. Xia, Y. Song, X.T. Zhou, X.D. Liu, M.W. Zhao, T.W. Wang, K.Y. Hou, Localized defects closely related with the magnetism of graphite induced by $^{12}C^{+}$ ion implantation, J Appl Phys 109 (2011) 083933.

[51] N. Shukla, M. Sarkar, N. Banerji, A.K. Gupta, H.C. Verma, Inducing large ferromagnetic ordering in graphite by 1 MeV C-12^{+} ion irradiation, Carbon 50 (2012) 1817-1822.
[52] Z. He, X. Yang, H. Xia, T.Z. Regier, D.K. Chevrier, X. Zhou, T.K. Sham, Role of defect electronic states in the ferromagnetism in graphite, Phys Rev B 85 (2012) 144406.
[53] X.Y. Sun, R. Wang, D.S. Su, Research progress in metal-free carbon-based catalysts, Chin. J. Catal. 34 (2013) 508-523.
[54] D. Chen, A. Holmen, Z.J. Sui, X.G. Zhou, Carbon mediated catalysis: A review on oxidative dehydrogenation, Chin. J. Catal. 35 (2014) 824-841.
[55] J.L. Figueiredo, M.F.R. Pereira, The role of surface chemistry in catalysis with carbons, Catal. Today 150 (2010) 2-7.
[56] R.A. Sidik, A.B. Anderson, N.P. Subramanian, S.P. Kumaraguru, B.N. Popov, O_2 reduction on graphite and nitrogen-doped graphite: Experiment and theory, J. Phys. Chem. B 110 (2006) 1787-1793.
[57] S. Biniak, G. Szymanski, J. Siedlewski, A. Swiatkowski, The characterization of activated carbons with oxygen and nitrogen surface groups, Carbon 35 (1997) 1799-1810.
[58] E. Raymundo-Pinero, D. Cazorla-Amoros, A. Linares-Solano, The role of different nitrogen functional groups on the removal of SO_2 from flue gases by N-doped activated carbon powders and fibres, Carbon 41 (2003) 1925-1932.
[59] B. Wang, Recent development of non-platinum catalysts for oxygen reduction reaction, J. Power Sources 152 (2005) 1-15.
[60] Y. Okamoto, First-principles molecular dynamics simulation of O_2 reduction on nitrogen-doped carbon, Applied Surface Science 256 (2009) 335-341.
[61] W.Y. Wong, W.R.W. Daud, A.B. Mohamad, A.A.H. Kadhum, K.S. Loh, E.H. Majlan, Recent progress in nitrogen-doped carbon and its composites as electrocatalysts for fuel cell applications, International Journal of Hydrogen Energy 38 (2013) 9370-9386.

Chapter 4. Surface modification of strontium titanate single crystals by Fe implantation

4.1 Introduction

Strontium titanates have recently attracted significant attention due to their outstanding electrical and ionic transport properties [1, 2]. Pure $SrTiO_3$ (or STO) has a perovskite crystal structure, and is a wide band semiconductor with an indirect band gap of 3.25eV. Many other structural and physical properties of strontium titanate were discussed in Chapters 1 and 3. When Ti is substituted by another transition metal, such as Fe, it can substantially change the transport properties of STO [3].

Fe-doped STO forms the solid solution series $SrTi_{1-x}Fe_xO_{3-\delta}$, $0 \le x \le 1$. $SrTi_{1-x}Fe_xO_{3-\delta}$ (or STF) is an interesting system covering the range of properties from large band gap semiconductor for low *x*, to a good electronic and ionic conductor for high *x* [4-8].The Fe-rich phase maintains both the good electronic and the ionic conductivity typical for strontium ferrate, and the Ti-rich phase represents an acceptor-doped large band gap insulator. $SrFeO_{3-\delta}$ has several ordered phases, which can accept cubic, tetragonal or Brownmillerite structure depending on the amount of oxygen vacancies [9-11]. Fe substitution for Ti stabilizes the perovskite phase, and mixed compound $SrTi_{1-x}Fe_xO_{3-\delta}$ can retain a cubic perovskite structure in a wide range of *x* [12]. This structural stability in reducing environments even at elevated temperature in combination with good conductivity, both ionic and electronic, makes $SrTi_{1-x}Fe_xO_{3-\delta}$ an attractive material for various applications, including gas sensors [1, 13, 14], oxygen permeation membranes [4, 7], fuel cell electrodes [15, 16], catalysts [17], resistive switching memory [18-20] and spintronics [6, 21].

Iron can accept two different oxidation states in STF (Fe^{3+}/Fe^{4+}). Substitution of Fe^{3+}on the titanium site, which has a Ti^{4+} state, requires oxygen vacancies to be an integral part of the perfect $SrTi_{1-x}Fe_xO_{3-\delta}$lattice to keep charge neutrality. If one uses

stoichiometry $SrTi_{1-x}Fe_xO_{3-x/2}$ then half of the Fe^{3+} ions should have mobile oxygen vacancies V_O^{**} (where V_O^{**} stands for an oxygen vacancy with double positive charge in Kröger-Vink notation) [3, 22]. Therefore, one can expect to have three types of coordination around oxygen sites: (i) *Fe-O-Fe*; (ii) *Ti-O-Ti*; and (iii) *Ti-O-Fe*. As a result, iron can be in 4-, 5-, and 6-coordination in $SrTi_{1-x}Fe_xO_{3-x/2}$ with different defect energies of the oxygen vacancies corresponding to these configurations [23].

The electronic structure of pure $SrTiO_3$ is determined by the hybridization of Sr *3d*, Ti *3d* and O *2p* states. The top of the valence band is dominated by O *2p* states with mixture of Sr *3d* and Ti *3d*, and the bottom of the unoccupied conduction band consists mainly of Sr *3d* and Ti *3d* orbitals [24, 25]. Defects in $SrTi_{1-x}Fe_xO_{3-\delta}$ narrow slightly the band gap and raise the Fermi level into the conduction band, which ensures the conductivity of the material [24-26].

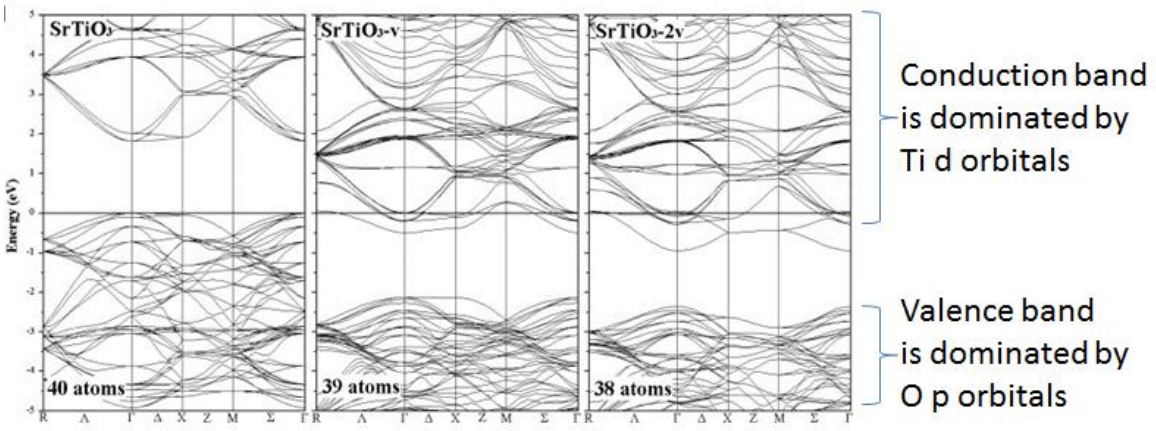

Figure 4.1 Strontium titanate band structure calculated for 40 atom supercell for pure STO and STO with oxygen vacancies. Modified from Ref. [24].

With an increase of iron content in $SrTi_{1-x}Fe_xO_{3-\delta}$, Fe ions cannot be considered as an impurity. The contribution from Fe *3d* states appears in the band structure of the system. Rothschild *et al.* [3] proposed that the top of the valence band is formed by the mixtures of Fe *3d* and O *2p* states, and the bottom of the conduction is assigned to Ti *3d* with mixture of Fe *3d* states.

Several recent studies have indicated that the properties of $SrTi_{1-x}Fe_xO_{3-\delta}$ depend on both the Fe doping concentration and on the oxygen content as well as on the oxidation state and the local symmetry of Fe atoms. Careful control of the doping and defect concentrations will open possibility to tune the material properties and to induce new properties such as magnetism.

In present study ion beam implantation method with following recrystallization annealing was used to modify properties of STO single crystals. Several low doses of Fe ion were chosen to be consistent with the typical levels of Fe contaminations for commercially available un-polished single crystal STO samples, as measured by particle-induced X-ray emission spectroscopy [27]. Using several complimentary analysis methods, the study aims to clarify the effect of Fe irradiation on the STO structure, the oxidation state and local coordination of the implanted Fe as well as the correlation between the Fe doping and the induced magnetic properties. The detailed understanding of transition metal doping and defects in STF system is important for practical applications of STF mixed oxide system such as gas sensors, oxygen permeation membranes and solid oxide fuel-cells [1, 2, 4, 14-16].

4.2 Fabrication of Fe doped strontium titanate samples

4.2.1 Ion beam implantation

Strontium titanate (STO) crystals were commercially acquired from MTI corporation ($SrTiO_3$(001) $5\times5\times0.5 mm^3$, two sides polished). $SrTiO_3$ single crystals were grown by the Verneuil process (flame fusion) [28, 29]. The principle of the process involves melting a finely powdered substance using an oxyhydrogen flame, and crystallizing the melted droplets into a boule. The MSDS datasheet for STO crystals from the manufacturer indicated bulk impurity levels less than 100 parts per million (ppm) with metallic impurities less than 50 ppm. STO crystals were implanted with 30 keV Fe^+ ions at several doses. To avoid channeling, implantation was conducted at 7° off the surface normal (Fig. 4.2(a)). During implantation the chamber pressure was no more than $p= 5\times10^{-8}$ Torr. The implantation stage was air cooled during the sample fabrication to minimize recrystallization processes and prevent possible diffusion and segregation of

iron. According to the thermocouple reading, the sample temperature was typically close to 25-30^{o}C and never exceeded 50°C. Several sets of samples were prepared with implantation doses of 2×10^{14} Fe/cm^2, 8×10^{14} Fe/cm^2, 1×10^{16} Fe/cm^{2}and 2×10^{16} Fe/cm^2 labeled as STO-Fe2e14, STO-Fe8e14, STO-Fe1e16 and STO-Fe2e16, respectively. The doses were chosen to be below concentrations at which individual metallic Fe crystals can be formed in the host material. Formation of metal clusters during ion irradiation depends on the parameters of the ion beam and the host material as well as post-implantation treatment. For instance, for 40 keV Fe implanted STO, metallic Fe cluster has been reported at implantation dose of 7.5×10^{16} Fe/cm^2 [21]. In our studies, implanted STO samples were then annealed for 2 h in oxygen atmosphere at 350^{o}C. The temperature was chosen to heal irradiation damage and to prevent formation of additional oxygen vacancies, and also to avoid diffusion of implanted iron and phase separation [30-33]. Implanted and annealed samples were marked as STO-Fe2e14-350C, STO-Fe8e14-350C, STO Fe-1e16-350C, and STO-Fe2e16-350C.

4.2.2 SRIM calculations of extended damage

According to SRIM simulation, 30 keV implanted Fe is in the near-surface layer of ~50 nm thick with a maximum concentration at ~17 nm (Fig. 4.2 (b)). Defects produced during implantation were mostly oxygen vacancies located in the ~40 nm layer in the near-surface area with maximum distribution at ~10 nm. SRIM calculations tend to overestimate the irradiation damage, giving in this case ~ 440 vacancies per each incident ion Fe ion incident to the surface. In practice self-healing processes lead to partial recombination of the defects produced.

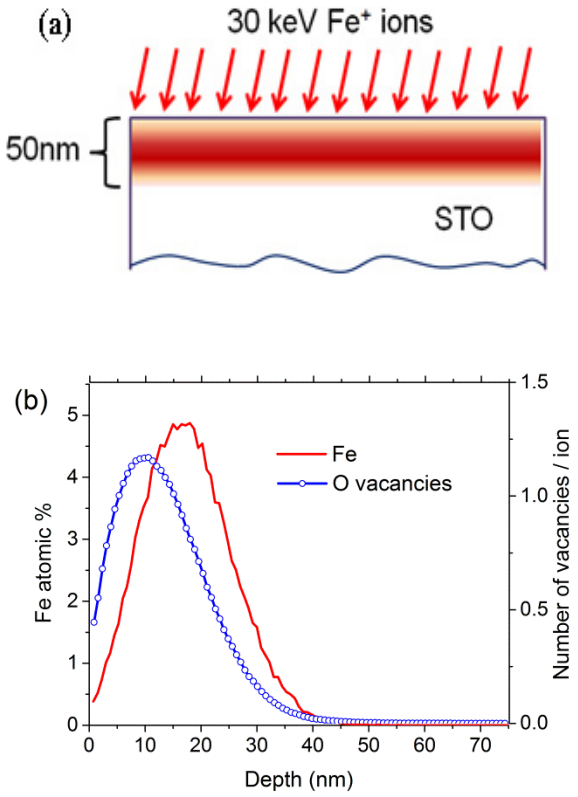

Figure 4.2. (a) Schematics of Fe ion implantation in strontium titanate crystal. (b) SRIM simulation of distribution of Fe ion and oxygen vacancies produced during implantation as function of depth.

4.3 PIXE analysis of STO samples

PIXE spectra were acquired at the Tandetron facility at the University of Western Ontario. 1 MeV H^+ particles were used to collect PIXE spectra from STO samples. The spectra were acquired with a liquid nitrogen (LN2) cooled high-purity Ge detector (resolution 135 eV at 5.9 keV) and a 5 mm diameter Be entrance window 13 μm in thickness positioned at the angle of 90° relative to the incident beam. The acquisition doses were typically 40 μC.

PIXE analysis showed that virgin STO crystals have a low concentration of impurities. Our PIXE spectrum from a virgin (before Fe implantation) STO crystal revealed the presence of K, Ca and Mn contaminations (Fig. 4.3). The Fe K_α peak is clearly noticeable in the PIXE spectrum of the STO-Fe2e16 sample after implantation (Fig. 4.3). However Fe peaks are not noticeable in spectra of samples with lower

implantation doses (STO-Fe2e14 and STO-Fe8e14) due to the high level of Ti pile-up (Figs. 4.4(a,b)).

The pile-up distortion of PIXE spectra is a result of the finite processing time of Ge detector. At high counting rates, pair of X-ray photons that arrives within the processing time of the electronic system is registered as a single event. It results in a continuum to the right of the main peaks. The continuum is terminated at an energy close to double the energy of the main peak which corresponds to the perfect overlapping of two emitted X-ray photons [34]. The special techniques (such as, the electronic pile-up rejector and the beam deflector technique) have been developed to reduce the pile-up intensity but it is impossible to remove it completely [35-37].

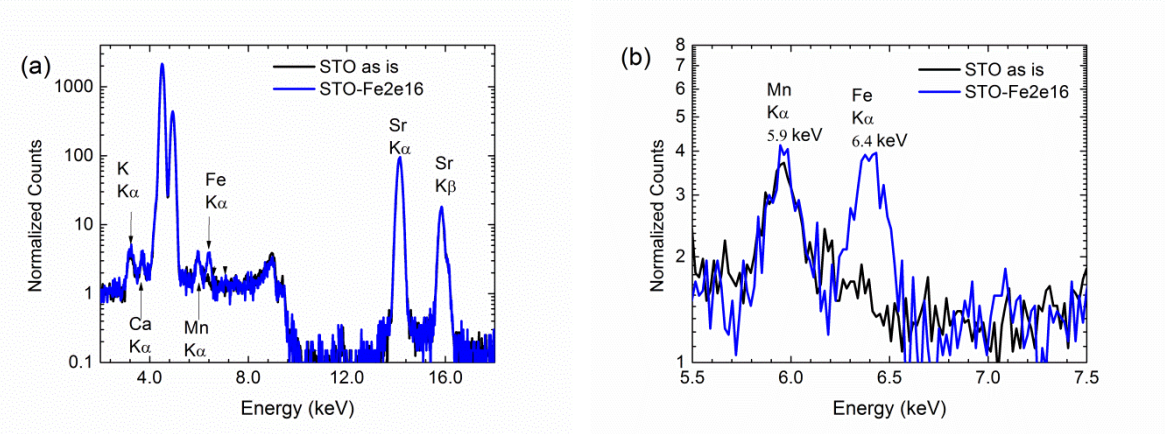

Figure 4.3. (a) PIXE spectra of un-implanted STO crystal and Fe implanted sample STO-Fe2e16. (b) Magnified portion with Fe K_α and Mn K_α peaks

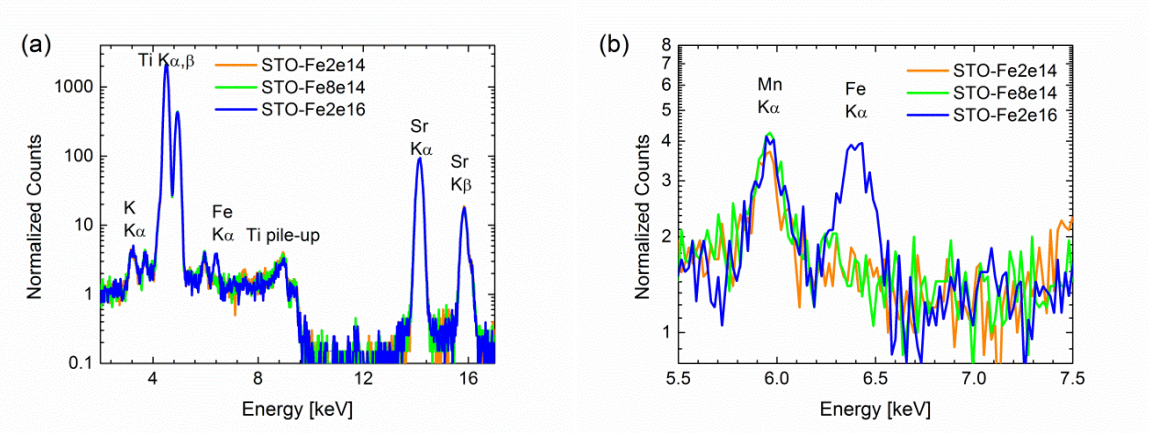

Figure 4.4. (a) PIXE spectra of Fe implanted samples STO-Fe2e14, STO-Fe8e14 and STO-Fe2e16. (b) Enlarged image of Fe K_α and Mn K_α peaks.

Comparison of PIXE spectra of implanted and annealed samples with highest implantation dose demonstrates that intensity of Fe K_α peaks do not change after annealing at 350°C (Figs. 4.5(a,b)). The visible decrease on Mn K_α peak intensity for STO-Fe2e16-350C sample (Fig. 4.5(b)) is caused by deviation in the impurity concentration in different STO crystal substrates prior to implantation treatment. The difference in Mn K_α peak intensity measured in different STO crystal was ~20%.

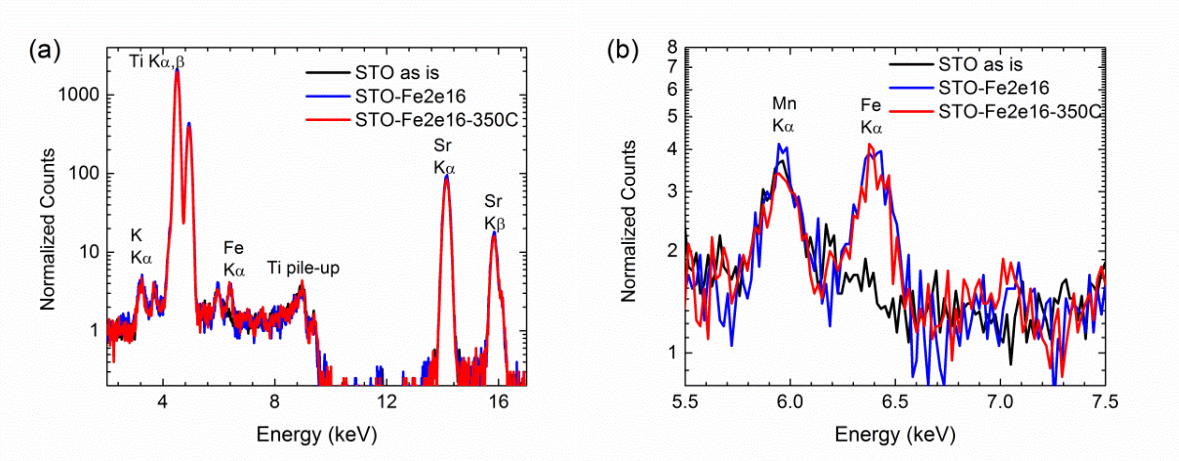

Figure 4.5. (a) PIXE spectra of Fe implanted sample STO-Fe2e16 and implanted and annealed samples STO-Fe2e16-350C. (b) Magnified portion with Fe K_α and Mn K_α peaks.

The standard sample with 58 mg/cm^2 or 6.3×10^{17} Fe/cm^2 in Al was used to estimate the atomic density of Fe and other transition metal impurities in the STO samples (Table 4.1). The atomic densities of Mn and Fe in STO and STO-Fe2e16 samples were estimated using the standard sample with known atomic density of Fe and equation (2.13) $(N_x t) = \frac{Y_x \sigma_{SS} A_{SS}}{Y_{SS} \sigma_x A_x}(N_{SS} t)$, where $N_x t$ is the areal density, σ_x is the ionization cross section, Q is the fluorescent yield, A_x is the attenuation factor, and Y_x is the intensity of the element x in PIXE spectrum. The subscript *SS* is referring to the standard sample. The values of the ionization cross section σ_x and the X-ray attenuations of the elements in Al and Be filters A_{Al}×A_{Be} indicated in Table 4.2.

The accuracy of the quantification in PIXE always depends on the depth of the element and how uniform its distribution is a function of depth. The probing depth of the method is on the order of several tens of microns. The intensity of X-rays emitted from the elements inside the target attenuates on the way out. The attenuation depends on the wavelength of X-ray photons as well on the depth from where they have been emitted. If the element is distributed inhomogeneously inside the target, it complicates the analysis. In general the uncertainty of the calculated atomic densities in the PIXE method is always higher compared to RBS. The calculated value of the atomic density of Fe 2.4×10^{16} atoms/cm^2 is within 20 % of the implantation dose. PIXE results showed that amount of Ni and Mn impurities is the same order of magnitude as the implanted Fe. Fe has a Gaussian-like distribution in STO in a ~50 nm layer in the near-surface area (SRIM simulation) whereas Ni and Mn impurities may be uniformly spread in the first several microns of the top crystal layer. Since the probing depth of PIXE is several μm, the local concentration of Fe in the implanted layer is considerably larger than that of Ni or Mn.

Table 4.1. Values of the atomic densities of elements in the standard sample 58 mg/cm^2 Fe in Al, unimplanted STO crystal and Fe implanted sample STO-Fe2e16.

Sample	Element	Channels (keV)	Integrated Area A	Atomic Density (10^{16} atoms/cm^2)
58 mg/cm^2 Fe in Al	Fe	6.18-6.70	30335	63±3
STO	Mn	5.70-6.18	818	1.5±0.1
	Ni	7.22-7.78	390	1.1±0.1
STO-Fe2e16	Mn	5.70-6.18	1107	2.0±0.1
	Ni	7.22-7.78	467	1.4±0.1
	Fe	6.18-6.70	1183	2.4±0.1

Table 4.2.Values of the ionization cross section and the X-ray absorption in Al and Be filters [38].

	σ_x	$A_{Al} \times A_{Be}$
Ni	9.738	0.664
Co	12.890	0.605
Fe	17.142	0.530
Mn	22.792	0.449

4.4 RBS analysis of strontium titanate samples

Rutherford Backscattering analysis was performed to estimate the irradiation damage and the distribution of the implanted iron. RBS spectra of STO samples were collected using 0.5 MeV and 3.03 MeV He^+ ion beams in random (5^o off the normal to the $SrTiO_3$ (001) surface) and aligned to the <001> direction geometry. The energy of the He^+ ion beam of 0.5 MeV was chosen as a compromise to provide a good separation of the surface peaks from Sr and Ti and a reasonably short time acquisition in the channeling RBS experiment. It is experimentally easier to find the channeling minimum at lower incident energy, at which the width of the channeling minimum is broader. The sample aligning procedure itself is more time consuming that the data acquisition time. The non-Rutherford cross section for oxygen at 3.03 MeV (sensitivity enhancement by a factor of ~ 14) allowed as to see the oxygen peak more clearly and also resolve Fe and Ti peaks.

For quantitative analysis, a Sb-implanted standard sample with a known Sb content of 4.93×10^{15} Sb^+ ions/cm^2 located 23 nm below the surface was measured to calibrate collected spectra using SIMNRA simulations.

RBS spectra of STO samples collected in random geometry with 0.5 MeV He^+ are shown in Figure 4.6. Vertical arrows show the positions of the Sr, Ti, and O surface peaks and the position of Fe peaks in the implanted samples. There is little difference between the STO, STO-Fe2e14, STO-Fe8e14 spectra, however there is a noticeable change in the intensity for Fe and Sr peaks for the STO-Fe2e16 sample.

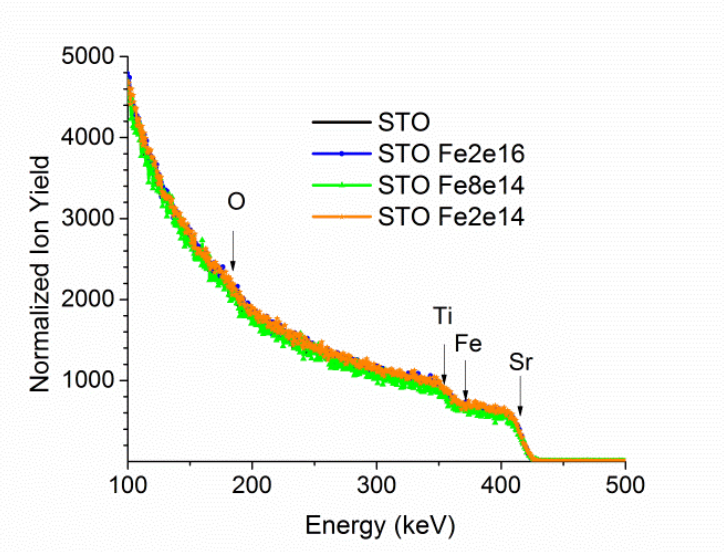

Figure 4.6. RBS spectra of virgin STO crystal and STO samples implanted with different Fe^{+}doses (STO-Fe2e14, STO-Fe8e14, and STO-Fe2e16) collected in random geometry.

SIMNRA simulation allows us to calculate the contributions from the individual elements in the targets. Figure 4.7 presents RBS spectra of virgin STO and STO-Fe2e16 acquired in random geometry with 0.5 MeV He^{+} beams. All three features due to Sr, Ti and O can be fitted well using stoichiometric $SrTiO_3$ composition. The peak from the implanted Fe layer is overlapping with the Ti features at the surface which makes it difficult to discern the Fe peak (Fig. 4.7(b)). Note that the simulated curve for Sr yield is significantly higher than experimental data if we use exact $SrTiO_3$ stoichiometry. This effect is mostly pronounced for the sample with the highest implantation dose STO-Fe2e16, also noticeable for STO-Fe1e16-350C, and was not detected for lower Fe concentrations: 8×10^{14} and 2×10^{14} Fe/cm^2.

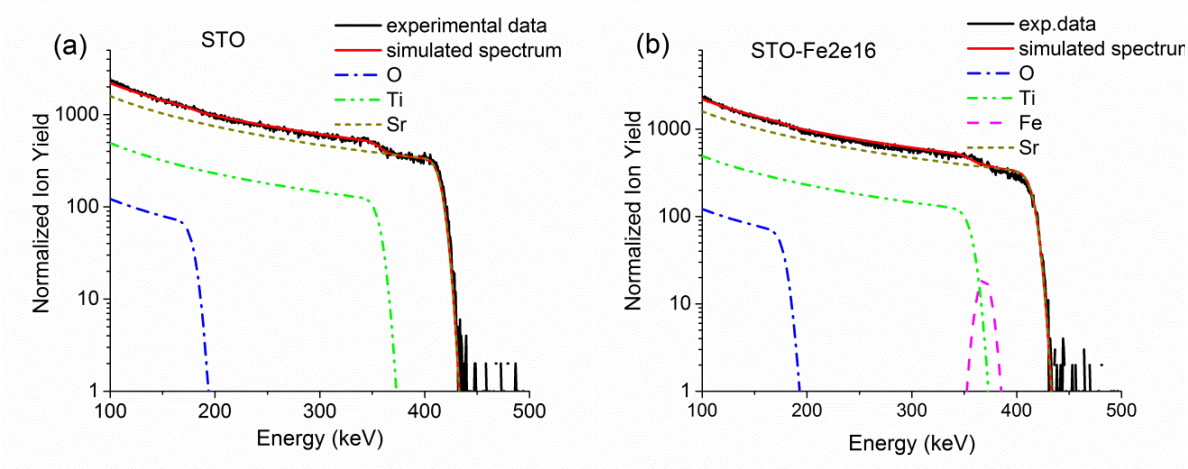

Figure 4.7. RBS spectra collected in random geometry with 0.5 MeV He^+ beams: (a) STO and (b) STO Fe2e16 with element contributions calculated in SIMNRA program.

When single crystals are irradiated with an ion beam, it produces disordering (amorphization) and recrystallization in crystal structure. A change in the ion scattering yields is anticipated in the channeling (aligned) geometry. However the decrease in the ion yields in the random geometry was unexpected; therefore we took special care to make sure that it is reproducible by repeating these RBS measurements several times (during several different days) with different samples.

Figure 4.8 compare RBS spectra of STO samples with two highest implantation doses (STO-Fe1e16, STO-Fe2e16) and following crystallization anneal (STO-Fe1e16-350C and STO-Fe2e16-350C) collected in random geometry (Fig. 4.8 (a)). Spectra of a virgin STO crystal are shown for the reference. A slight decrease in the Sr peaks is noticeable at the surface of the samples (Fig. 4.8 (a) insert). The decrease of Sr yield after implantation and post-implantation annealing for near-surface region was quantified (see Table 4.3). In comparison to virgin STO crystal, implanted sample, STO-Fe2e16, lost ~9 % in the integrated area of the surface Sr peak, and STO-Fe2e16-350C lost ~11 %. Similar trends were observed in the RBS spectra of STO-Fe1e16 and STO-Fe1e16-350C (Fig. 4.8 (b)). The mechanism of Sr loss from near-surface region will be discussed further below, in section 4.6.

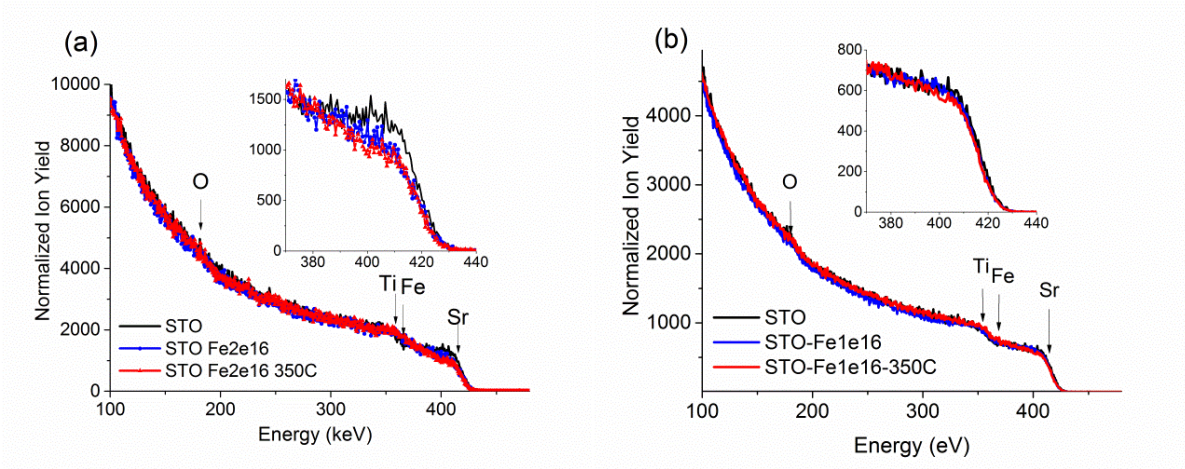

Figure 4.8. RBS spectra of (a) STO, STO-Fe2e16 and STO-Fe2e16-350C samples; and (b) STO, STO-Fe1e16 and STO-Fe1e16-350C samples collected in random geometry with 0.5 MeV He^+ beams.

Table 4.3. Change in the integrated area of Sr peak for STO samples after implantation and post-implantation annealing.

Sample	Counts integrated for channels [630—680]	Loss of Sr compared to unimplanted (virgin) STO (%)
STO	14856	0
STO-Fe2e16	13579	9%
STO-Fe2e16-350C	13247	11%
STO (10×10)	14884	0
STO-Fe1e16	14129	7%
STO-Fe1e16-350	13235	10%

RBS spectra collected with a 500 keV He^+ ion beam aligned along the STO [001] axis are shown in Figure 4.9 for virgin STO crystal, STO-Fe2e16 and STO-Fe2e16-350C samples. Three surface peaks from Sr, Ti and O can be distinguished in the channeling spectrum of virgin STO. The ion yield in the channeling spectrum from virgin STO

sample is much lower than the yield in spectrum from the same sample collected in random geometry. The ratio of ion yield in the channeling spectrum to the random spectrum yields, or the minimum yield χ_{min}, is ~6±1% for the virgin STO crystal. It proves an excellent crystallinity of the crystal prior to ion implantation.

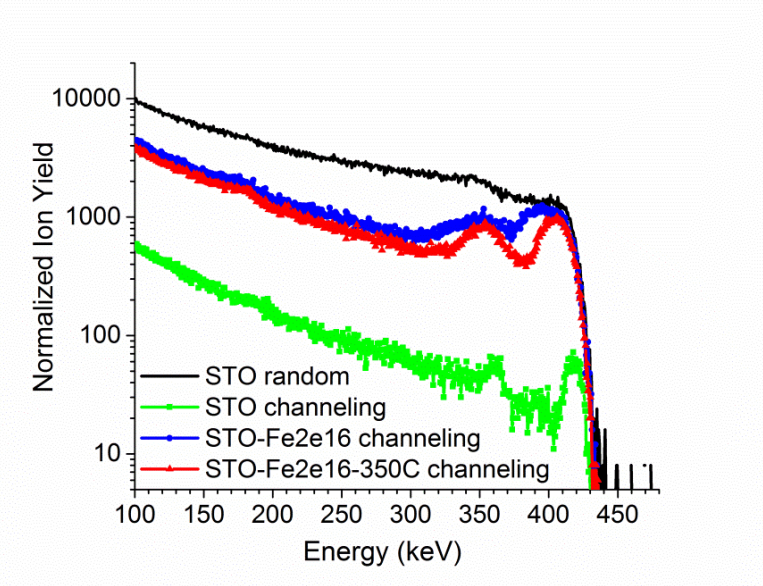

Figure 4.9. RBS spectra of STO, STO-Fe2e16 and STO-Fe2e16-350C samples collected in channeling geometry with 0.5 MeV He^+ beams.

Distinct peaks of strontium, titanium and oxygen can be observed corresponding to the top surface layer of the STO sample. Iron implantation caused considerable irradiation damage to STO crystal. As we use a channeling geometry, we do not detect subsurface atoms in their ideal lattice positions. However atoms in disordered regions or even amorphous regions will be visible to the ion beam. Therefore, we see a systematic increase in the detected ion yields for the implanted sample (STO-Fe2e16), both in the top-surface layer yields, and in the bulk of the STO sample. Crystallinity of the samples improved after annealing in oxygen. However it does not reach the initial (prior-to-implantation) value. The RBS spectrum for the STO-Fe2e16-350C sample shows that the minimum yield χ_{min} is 26±1% from the random RBS spectrum of virgin STO. Post-implantation annealing only partially healed the irradiation damage and improved crystal structure.

RBS spectrum collected at 3.03 MeV ion beam energy in random geometry for the STO-Fe2e16 sample is presented in Figure 4.10. Sr, Ti, and O features were fitted using the stoichiometric $SrTiO_3$ composition. At this energy the Fe peak and Ti peak from the surface are well resolved, and we can estimate that Fe areal density is 2×10^{16} atoms/cm^2 The energy 3.03 MeV corresponds to the non-Rutherford cross section for O. As a result, the surface peak from O is noticeably intensified as compared to that of a RBS spectrum collected at 0.5 MeV (Fig. 4.7).

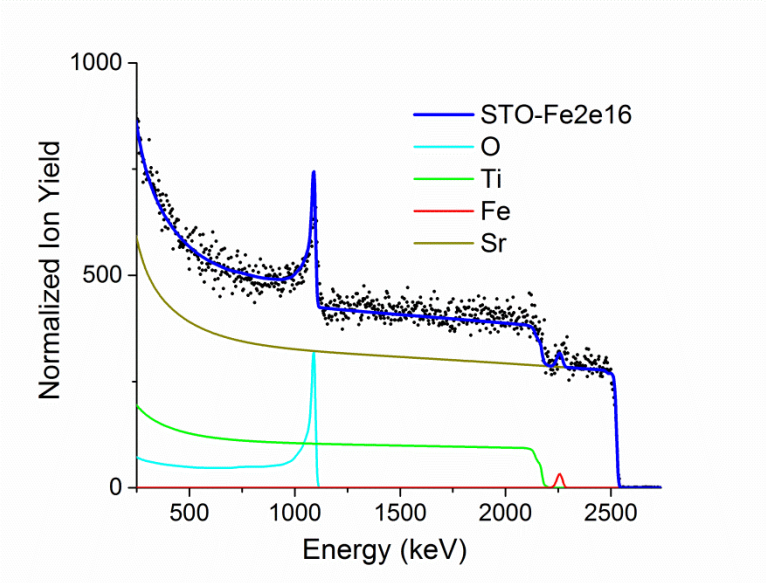

Figure 4.10. RBS spectrum of STO-Fe2e16 sample collected at random geometry with 3.03 MeV He^+ beam.

4.5 XPS analysis of STO samples

XPS analysis of STO samples were performed at Surface Science Western center at the University of Western Ontario with a Kratos Axis Ultra spectrometer. A monochromatic Al K_α source (15 mA, 14 kV) with a photon energy 1486.7 eV was used in all of XPS measurements presented here. Instrument pressure during the spectra acquisition was better than 8×10^{-10} Torr. Charge neutralization was performed for all analyses by monitoring of the C 1s peak for adventitious carbon using the Kratos charge neutralizer system. The C 1s peak position was set to 285 eV. High-resolution spectra were obtained using an analysis area of ~300μm×700μm and either a 10 eV or 20 eV pass

energy which corresponds to a Ag $3d_{5/2}$ FWHM of 0.47 eV and 0.55 eV, respectively [39-41].

To perform depth resolved analysis, surface of the samples was sputtered with Ar^+ ion beam. Sputtering rates were calculated based on an Al_2O_3/Al standard (1.32 nm/min). Analyses were carried out on the surface and at 10, 20, 30 and 40 nm depths on virgin STO, Fe-implanted STO-Fe2e16 and implanted and annealed STO-Fe2e16-350C samples.

Spectra were analyzed using CasaXPS software [42]. All spectra are replotted as a function of binding energy. High-resolution XPS spectra were measured for Sr 3d, Ti 2p, Fe 2p, C 1s, and O 1s peaks. Spectra were charge corrected to the Ti 2p3/2 peak for Ti(IV) ($SrTiO_3$) set to 458.1 eV (based on a SrTiO3 standard sample). Ti 2p, Fe 2p and O 1s fitting is carried out using Gaussian-Lorentzian profiles according to the procedure described elsewhere [39, 40].

4.5.1 Ti 2p peaks

The Ti $2p_{3/2}$ and Ti $2p_{1/2}$ peaks are located at 458.1 eV and 463.82 eV (Fig. 4.11(a)), respectively, for all samples, and well in agreement with reported values for Ti(IV) state, assigned in agreement with the NIST database [41]. These peak positions and line splitting are consistent with the values reported for the $SrTiO_3$ in the literature [43, 44], however there is a decrease in peaks intensities following implantation (Fig. 4.11(b)).

Figure 4.12 presents the Ti 2p spectrum of a STO crystal after sputtering of 10 nm layer demonstrating asymmetric shape caused by the lower binding energy contributions, corresponding to Ti(III) and Ti(II). This is expected due to the different sputtering rates for different elements. Light elements, such as oxygen or carbon, are removed more easily during sputtering process. Therefore, sputtering leaves the STO surface in an oxygen depleted condition, which is reflected in XPS spectra by the presence of different oxidation states for Ti. Similar trends were observed for other implanted and sputtered STO samples.

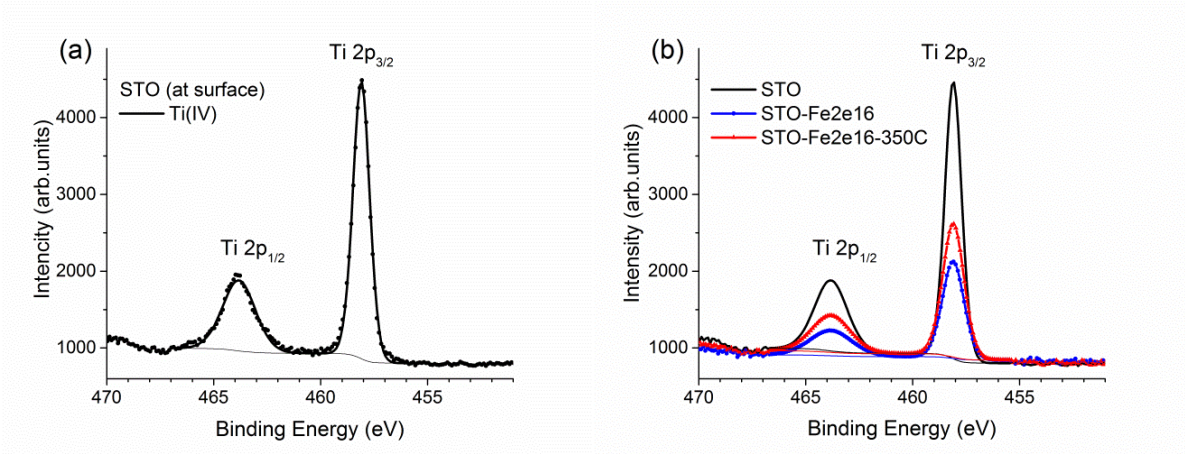

Figure 4.11. (a) Ti 2p peaks in XPS spectra of un-implanted STO crystal; (b) comparison of un-implanted STO, implanted STO-Fe2e16 and implanted and annealed STO-Fe2e16-350C samples collected at the surface.

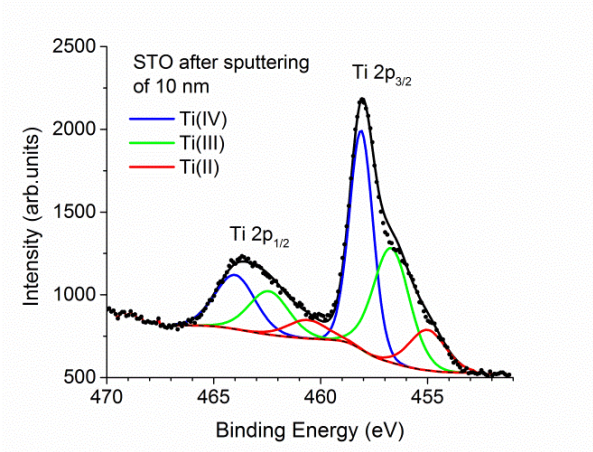

Figure 4.12. XPS 1s Sr peaks of STO crystal collected after sputtering of 10 nm layer.

4.5.2 Sr 3d peaks

Sr 3d peaks of virgin STO were fitted with Sr $3d_{3/2}$ and Sr $3d_{5/2}$ peak components as shown in Figure 4.13 (a). However Sr 3d spectra of implanted and oxygen annealed samples (STO-Fe2e16 and STO-Fe2e16-350C) exhibited high binding energy (HBE) contributions. The spectra were fitted by two Gaussians doublets separated by ~1 eV (Fig. 4.13(b) and (c)). Therefore, Sr exists in two different chemical environments on the surface in these samples.

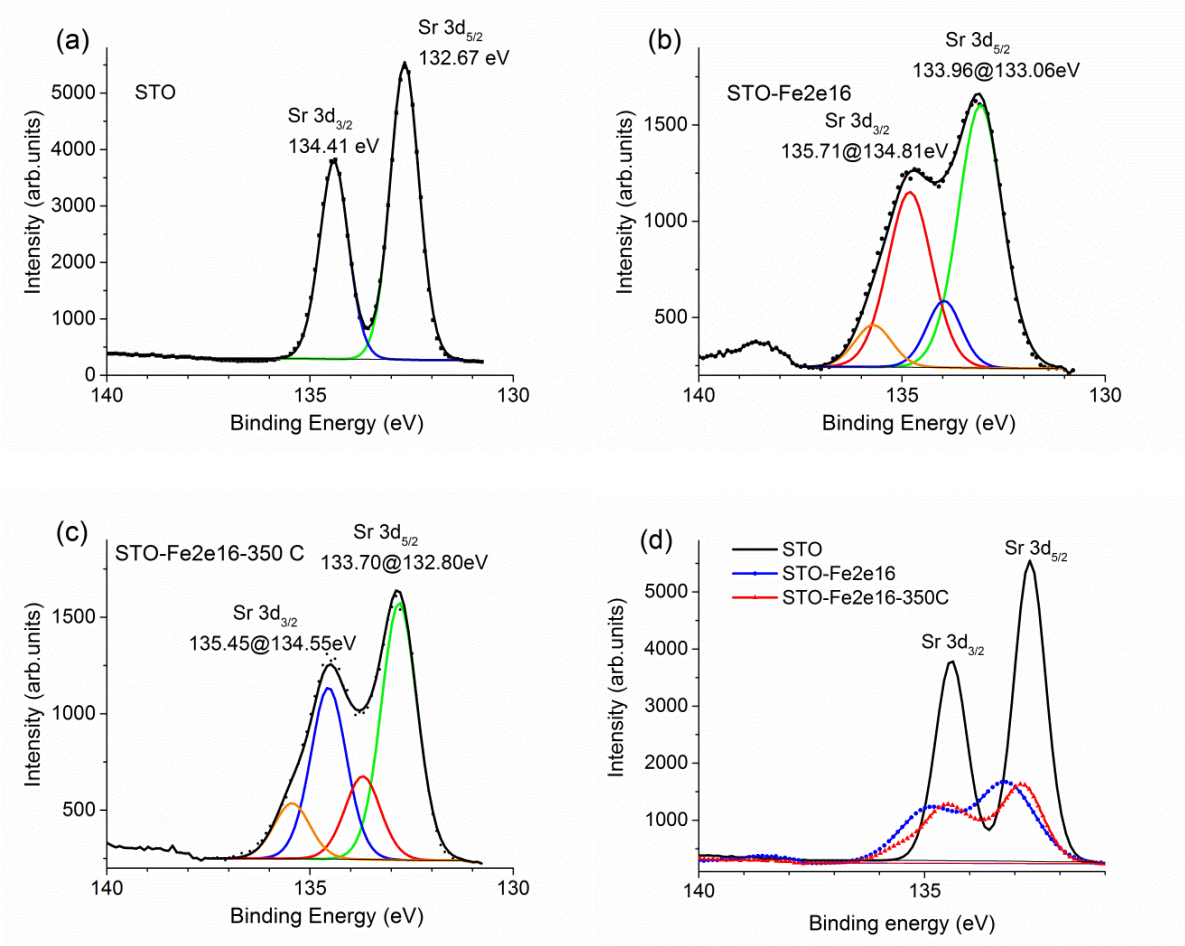

Figure 4.13. Sr 3d peaks in XPS spectra of (a) virgin STO crystal, (b) implanted STO-Fe2e16 and (c) implanted and annealed STO-Fe2e16-350C samples collected at the surface; (d) comparison of the three STO samples following Fe implantation and anneal.

Chemical shifts of Sr 3d peaks are detected in STO, STO-Fe2e16 and STO-Fe2e16-350C spectra on the surface, reflecting changes in the local chemical environment for Sr after Fe implantation. We also note that there is a significant decrease in Sr peak intensities, consistent with our RBS results. Upon Fe implantation Sr 3d peaks showed a shift toward higher binding energy. In the implanted and annealed sample (STO-Fe216-350C), Sr 3d peaks moved back to lower binding energies (though still higher than the initial value registered for virgin STO crystals). The position of the more intense Sr $3d_{5/2}$ peak was at ~ 132.67 eV, ~ 133.06 eV, and ~ 132.80 eV for STO, STO-Fe2e16 and STO-

Fe2e16-350C samples, respectively (see Table 4.4). Annealing in O_2 decreased the relative intensity of HBE components comparing to Sr 3d peaks from surface oxide SrO.

After Ar sputtering, Sr 3d peaks were observed at higher binding energy (see Fig.4.14 showing spectrum of STO after sputtering of 10 nm layer). Positions of Sr $3d_{5/2}$ and Sr $3d_{3/2}$ peaks become 135.0 eV and 133.3 eV, respectively, for all of STO samples after sputtering, regardless of previous treatment of the samples or of the sputtered depth (Fig.4.14). Note that this is the opposite trend to the reduction effects observed for Ti 2p peaks. After sputtering the intensities of the Sr peaks increased due to removal of carbon and oxygen containing functional group on the surface (as we will show below).

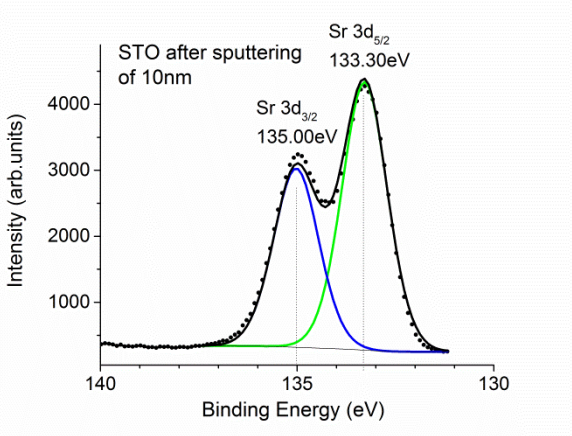

Figure 4.14. Sr 3d peaks in XPS spectra of STO crystal after sputtering of 10nm layer.

Table 4.4 Position of Sr $3d_{3/2}$ and Sr $3d_{5/2}$ peaks for STO samples, eV.

Sample	Sr $3d_{3/2}$ (eV)	Sr $3d_{5/2}$ (eV)	Sr $3d_{3/2}$ HBE (eV)	Sr $3d_{5/2}$ HBE (eV)
STO	134.41	132.67		
STO-Fe2e16	134.81	133.06	135.71	133.96
STO-Fe2e16-350C	134.55	132.80	135.45	133.70
STO after sputtering	135.00	133.30		

4.5.3. Fe 2p peaks

As predicted by SRIM simulation, 30 keV Fe^+ is implanted below the surface of STO crystal in a layer less then ~50 nm, with the maximum at ~17 nm, and extremely small Fe concentrations on the surface. No Fe peaks are detected in the XPS spectra of implanted samples collected at the surface before sputtering. Fe 2p peaks can be detected only after sputtering of the 10 nm layer. Fe 2p spectra collected after sequential sputtering at different depth of the two implanted samples are presented in Figure 4.15(a). The intensity of the Fe peaks became negligible at a depth of 40 nm. No Fe peaks were detected at a depth of 50 nm. Similar to Ti, because of the preferential sputtering, all Fe is reduced to the oxidation state Fe^0.

The depth distributions of the implanted Fe were derived from the intensity of XPS Fe peaks, and it is in agreement with SRIM simulation, most of Fe was found on the depth of 20 nm below the samples surface (Fig. 4.15(b)). No significant diffusion of the implanted Fe is detected after annealing to 350°C.

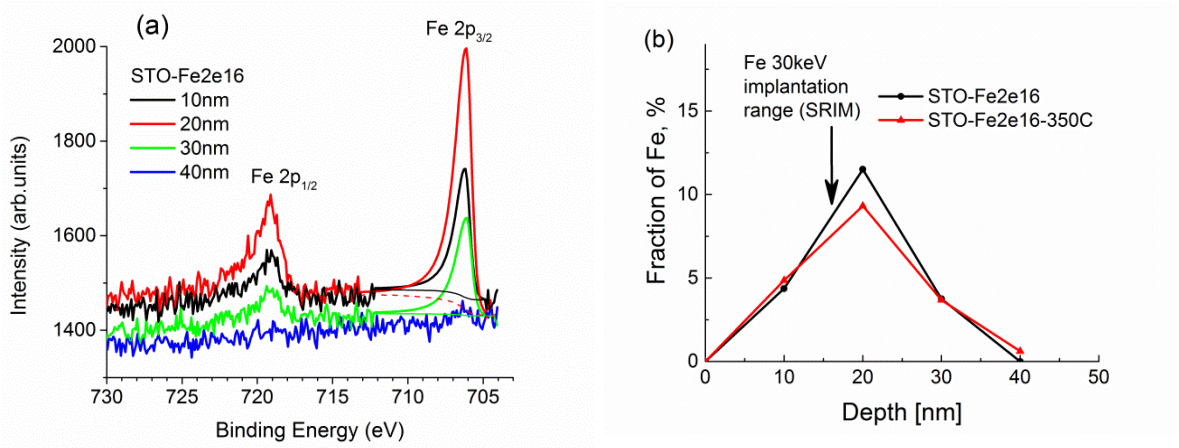

Figure 4.15 (a) XPS Fe 2p peaks for STO-Fe2e16 sample collected at 10 nm, 20 nm, 30 nm and 40 nm depth after sputtering. (b) Depth distribution of implanted Fe derived from the intensities of Fe 2p XPS peaks.

4.5.4 O 1s peaks

The O 1s peak of a $SrTiO_3$ crystal can have several contributions from oxygen that belongs to (a) $SrTiO_3$, (b) hydroxide and/or defective oxides, and (c) to water and/or organic compounds on the surface. Accordingly, the O 1s peak of the virgin STO crystal was fitted with three components, with the most intensive peak at ~ 529.2 eV originating from the regular oxygen sites in $SrTiO_3$, and two weaker peaks at ~ 530.9 eV from the hydroxide/defective contributions and at ~ 532.0 eV from water/organic contributions (Fig. 4.16(a)).

The spectra for implanted STO-Fe2e16 and implanted and annealed STO-Fe2e16-350C samples showed that the oxide peaks decreased and the water/organic oxygen peaks increase compared to the un-implanted STO sample (Figs. 4.16(b), (c) and (d)). Studies of the interaction of water with pure $SrTiO_3$(100) surfaces have shown that that defect-free surfaces do not interact with water at temperatures below 200 K [45]. However H_2O readily adsorbs on the STO surface defects (for example, created by sputtering). The implanted and annealed STO-Fe2e16-350C sample had the less intense water/organic oxygen since it was annealed in oxygen (Fig. 4.16(b-c)). Positions of O 1s peaks moved to the higher binding energies after implantation (see Table 4.5).

Table 4.5 Position of O 1s peaks for STO samples, eV.

Sample	O 1s Oxide (eV)	O 1s Defective Oxides, Hydroxide (eV)	O 1s Water, Organic oxygen, (eV)
STO	529.20	530.90	532.00
STO-Fe2e16	529.56	531.19	532.28
STO-Fe2e16-350C	529.55	531.20	532.28
STO after sputtering	529.75	531.12	

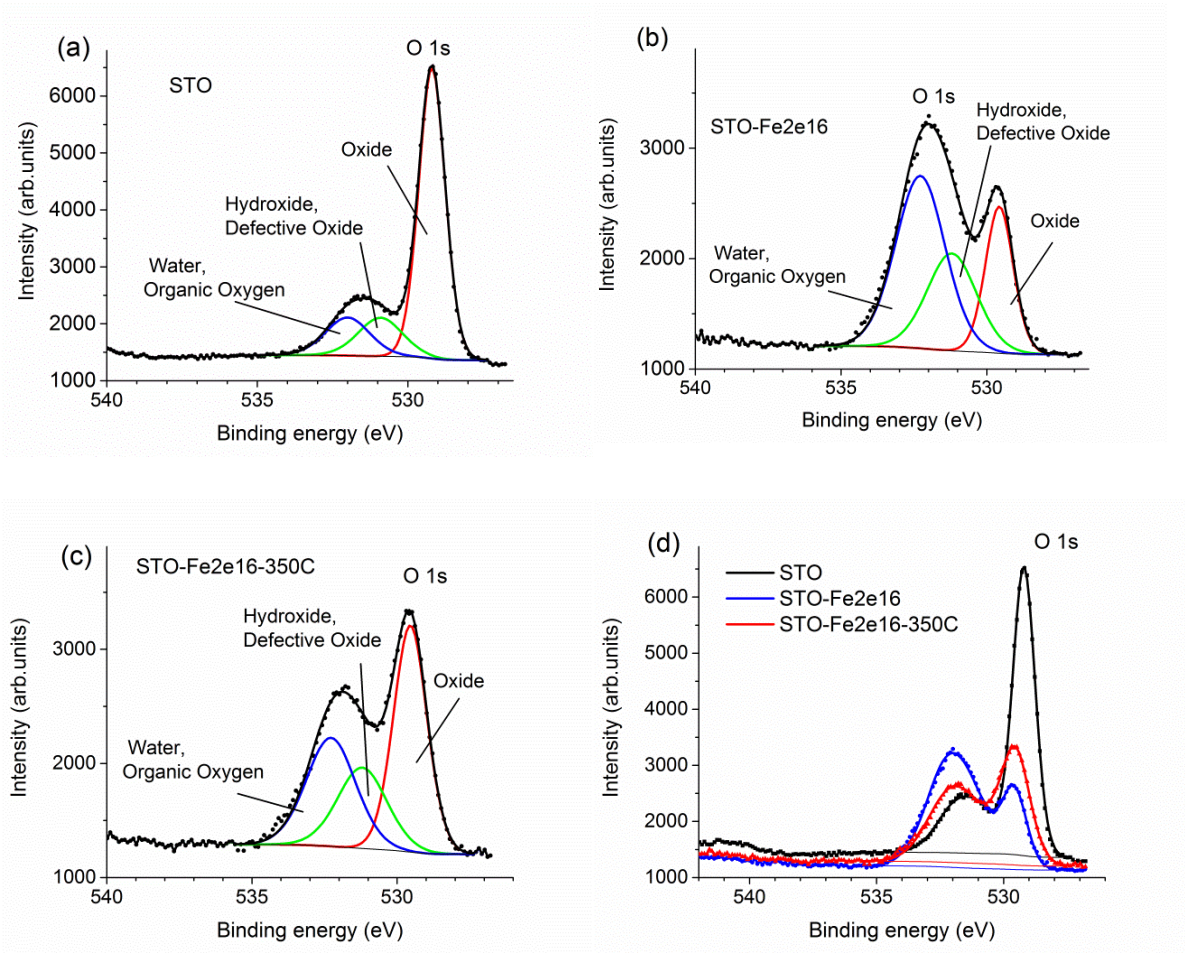

Figure 4.16. O 1s peaks in XPS spectra of (a) STO crystal, (b) implanted STO-Fe2e16 and (c) implanted and annealed STO-Fe2e16-350C samples collected at the surface; (d) comparison of the three STO samples following Fe implantation and anneal.

No difference was observed between the O 1s spectra of STO, STO-Fe2e16 and STO-Fe2e16-350C samples collected after sputtering (Fig. 4.17). All spectra collected after sputtering displayed only the $SrTiO_3$ oxide and defective oxide contributions. Even though there are slight variations (±5%) in the peak intensities, the position of the O 1s peaks were the same (~ 529.75 eV and ~ 531.1 eV for oxide and defective oxide contributions, respectively) in all XPS spectra acquired at different sputtering depths (20 nm, 30 nm and 40 nm) for all $SrTiO_3$ samples. Therefore, only O 1s spectra of STO samples collected after sputtering of the 10 nm layer are shown in Figure 4.17.

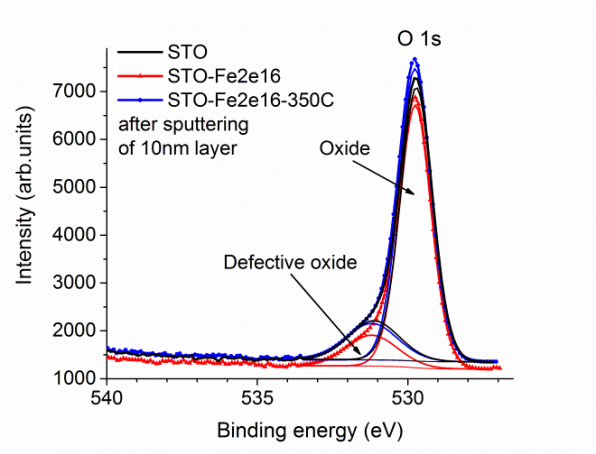

Figure 4.17. XPS 1s O peaks of STO crystal, implanted STO-Fe2e16 and implanted and annealed STO-Fe2e16-350C samples collected after sputtering of 10nm layer.

4.5.5 C 1s peaks

Strong carbon peaks are present in XPS spectra collected on the surface of all our strontium titanate samples. Carbon contamination is inevitable when samples are exposed to atmosphere [46, 47]. C 1s XPS spectrum of STO-Fe2e16 samples is presented in Figure 4.18(a). The spectrum was fitted with several components from different carbon functional groups (Fig. 4.18(a)). The most intensive peak in the spectrum belongs to alkyl-type carbon with sp^3 hybridization (C-C and C-H bonds) [48]. Additional peaks above it are ascribed to alcohol(C–OH) and/or ester (C–O–C), to carbonyl (C=O) and to carboxyl (O-C=O) functionalities.

Figure 4.18(b) compares C 1s peak for virgin STO crystal, implanted STO-Fe2e16 and implanted and annealed STO-Fe2e16-350 C samples. C peak is significantly higher for the STO-Fe2e16 and STO-Fe2e16-350C samples compared to the virgin STO crystal (Fig. 4.18(b)) due to a large number of defects on the surface of implanted samples. Carbon-containing molecules were more readily absorbed on the defect sites on the surface of implanted samples. Studies of STO surface with defects created by sputtering have shown that CO and CO_2 can adsorb on defect sites even at room temperature. The surface reactions have led to dissociation of the molecules with further formation of $SrCO_3$ [46, 49, 50]. The increase of carboxyl (O-C=O) component is clearly seen in STO-

Fe2e16 spectrum. After oxygen annealing the carboxyl component became less intense (Fig. 4.18(b)).

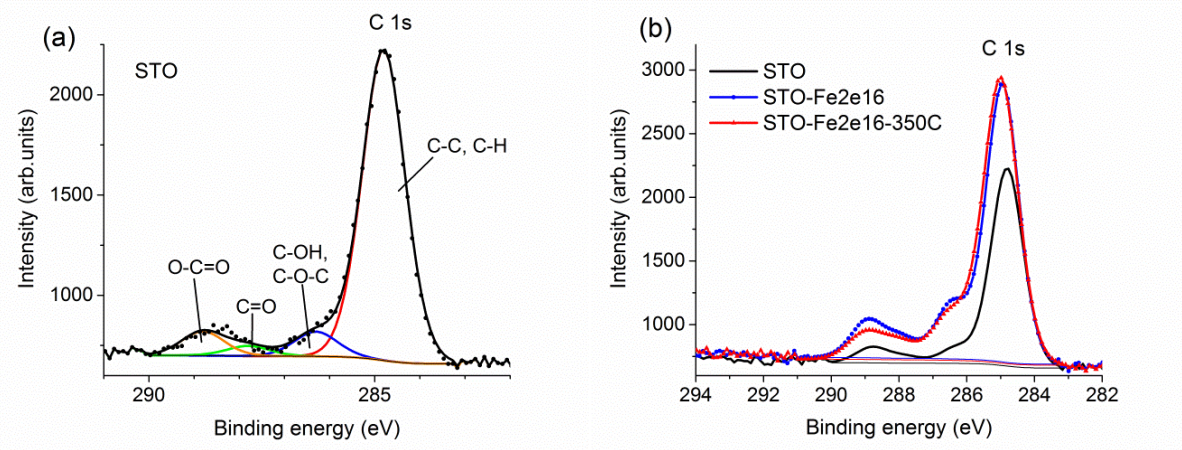

Figure 4.18. C 1s peaks in XPS spectra of (a) STO crystal, collected at the surface; (b) comparison of STO, STO-Fe2e16 and STO-Fe2e16-350C samples following Fe implantation and anneal.

After sputtering, the intensity of C 1s peaks goes down almost to the XPS limit of detection level, as evident from XPS spectra for STO shown in Figure 4.19. Sputtering removes carbon functional groups from the surface of the STO samples, and because it was done inside XPS apparatus in ultra-high vacuum, there was no formation of adventitious carbon adsorbate layer on the sputtered surfaces of STO samples. C 1 s spectra of STO-Fe2e16 and STO-Fe2e16-350C after sputtering are identical to the virgin STO samples indicating that carbon environment is only different on the surfaces.

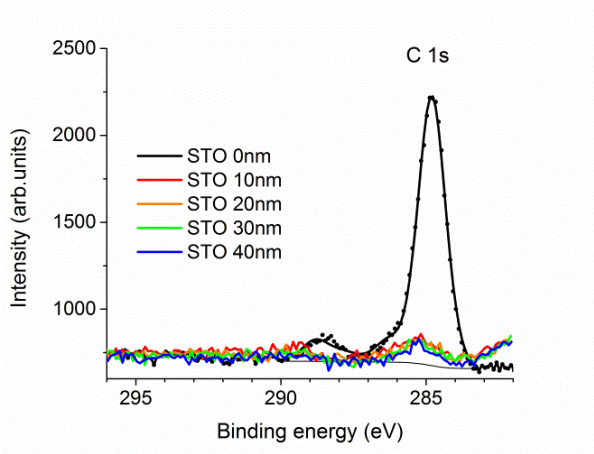

Figure 4.19. XPS 1s C peaks of STO crystal collected at surface and after sputtering at depth 10nm, 20 nm, 30 nm and 40 nm.

4.6 Discussion

The distribution of implanted Fe predicted by SRIM simulation was confirmed by XPS analysis. The step-by-step sputtering of STO-Fe2e16 surface showed that Fe could be found in the 40 nm deep layer with maximum at ~20 nm depth in agreement with SRIM predictions. Annealing at 350^{o}C did not cause any significant diffusion of the implanted Fe.

Unfortunately, Ar sputtering itself introduced considerable damage to the STO surface. Thus, there was preferential sputtering of O as the lightest constituent of STO. As a result it did not allow taking advantage of the XPS capacity to show the oxidation states of elements in the bulk of STO. As one can see from Ti 2p peaks after sputtering up to 50 % of Ti was reduced from Ti^{4+} to $Ti^{3+}$and Ti^{2+} (Fig. 4.12). For the same reason the oxidation state of implanted Fe were Fe^{0} as identified from Fe 2p XPS peaks (Fig. 4.15).

Notably, Fe implantation also increased the reactivity of STO surface [2, 43, 45, 46, 50]. Different carbon and oxygen groups from the ambient atmosphere were adsorbed on the defect sites created by ion irradiation. It can be seen from the increase of O 1s and C 1s peaks intensity in XPS spectra of STO-Fe-2e16 and STO-Fe-2e16-350C samples (Figs.4.16 and 4.18). The position of the peaks indicated the possible formation of alcohol(C–OH) and/or ester (C–O–C), carbonyl (C=O) and carboxyl (O-C=O) functionalities. The thermal treatment changed the amount of different functional groups

but did not remove them completely. Ar sputtering conducted in vacuum cleaned STO surface of carbon contaminations, which lead to a decrease of C 1s peaks intensity (Fig.4.19). The sputtering also removed any traces of water molecules absorbed on the STO surface.

The high binding energy components were observed in Sr 3d peak in addition to the main components due to strontium titanate for STO-Fe2e16 and STO-Fe2e16-350C samples (Fig.4.13). At the same time the shift of the main components of Sr 3d peaks to higher binding energy due to SrO was noticed in the STO-Fe2e16 and STO-Fe2e16-350C XPS spectra.

Depending on the samples treatment, the Sr 3d peak shift has been ascribed to hydroxyl species Sr-COH [49, 51], SrO_x layers [52] or strontium carbonate $SrCO_3$, formed due to the reaction of $SrTiO_3$ surface with CO and CO_2 [43, 44]. Pilleux *et al.* have observed the Sr 3d peak shifts from 132.7 eV for as-grown STO films on Ti foil to 133.0 eV for Ar sputtered surface. The authors explained it by the presence of hydroxyl groups adsorbed on the surface prior to Ar ion irradiation. In a more recent study of $SrTiO_3$(001) surface, the Sr peak shift was explained by the change in the Madelung potential due to oxygen vacancies formed by ion irradiation [49, 53, 54]. The electrostatic potential of the cationic sites diminishes and the atomic screening of the core hole increases with a decrease of the coordination number of a metal atom. These effects should effectively decrease the binding energy in the metal atom. However when the coordination number of a metal atom decreases, the negative Madelung potential at the cationic sites and the polarization screening of the final state become lower as well. These processes result in increase of the binding energy in the metal atom.

These considerations can explain our experimentally observed increase of the Sr binding energy in Fe-implanted STO crystal and, likewise, the presence of Sr 3d doublets in the spectrum of implanted and annealed samples. The appearance of HBE components in STO-Fe2e16 and STO-Fe2e16-350C Sr 3d spectra can be ascribed to $SrCO_3$ formed due to reactions with CO and CO_2 on STO surface [43, 46, 50], while shift of the main component of Sr 3d peaks to higher binding energy can be explained by the decrease of the Madelung potential (see Table 4.4).

Decrease of intensity of the Sr edge in a near-surface layer affected by implantation was noticed in RBS spectra collected in random geometry. The effect was proportional to the implantation dose and to the post-implantation annealing. Thus, the most profound change in the Sr content on surface was observed for STO implanted with highest dose STO-Fe2e16 (9 %) and STO-Fe2e16-350C (11 %). Surface reactions involving CO and CO_2 from the ambient atmosphere can explain the unexpected loss of Sr on the surface after Fe implantation and subsequent thermal treatment.

There were several reports of the surface instability and phase separation for $SrTiO_3$ under the influence of ion and electron irradiation and thermal treatment [55-58]. However, in several studies there were reports on a possible Sr segregation (as the opposite of Sr loss observed in our case), either as SrO or reconstructed Sr excess phases $SrO \cdot n(SrTiO_3)$. For instance, Sabathier *et al.* [56] have identified Sr_2TiO_4 and TiO_2 phase separation induced by 320 keV Pb^{2+} ions irradiation.

SrO can desorb from the $SrTiO_3$ (001) surface in vacuum at temperatures as low as 450-500^oC, leading to some loss of Sr from the surface [59]. SrO desorption was also observed by Shin *et al.* [55] in epitaxial $SrRuO_3$ /$SrTiO_3$ films with desorption peak at 480^oC, accompanied by surface roughening. The authors have emphasized the role of hydrocarbon contaminations as one of conditions for $SrRuO_3$ surface roughening and decomposition into SrO and Ru phases [55]. Decrease of Sr content accompanied with Fe segregation at the surface as a result of oxygen annealing has been also reported in Fe-doped STO thin films [58]. However the driving force of the transformation was unclear.

As a separate argument, the Sr loss in Fe-implanted $SrTiO_3$ observed in the present experiments can be due to relative decrease of Sr content as the result of different near-surface layer formation. As follows from our XPS results, defects created by ion irradiation are active sites for reaction of CO, CO_2 and H_2O with the STO surface. The new phase which probably contains strontium carbonate and strontium hydroxide has lower density than STO. As a result, the surface layer of STO-Fe2e16 and STO-Fe2e16-350C as measured by RBS analysis appears as Sr deficient. The dependence of Sr loss effect on the implantation dose is clearly connected to the different concentration of defects produced during ion irradiation.

In summary, the effect of the ion beam irradiation on STO crystal structure is clearly observed in RBS spectra. Fe implantation caused disordering in Sr and Ti sublattices. Annealing in O_2 at 350°C only partially healed the irradiation damage. Ion irradiation and post-implantation annealing caused relative decrease of Sr content in the near surface area. XPS analysis showed that ion irradiation and post-implantation annealing increased the surface reactivity. In presence of oxygen vacancies, strontium carbonate $SrCO_3$ formed on the STO surface in result of the reaction with the gases from the ambient atmosphere.

References

[1] W. Menesklou, H.J. Schreiner, K.H. Hardtl, E. Ivers-Tiffee, High temperature oxygen sensors based on doped $SrTiO_3$, Sensor Actuat B-Chem 59 (1999) 184-189.

[2] R. Merkle, J. Maier, How is oxygen incorporated into oxides? A comprehensive kinetic study of a simple solid-state reaction with $SrTiO_3$ as a model material, Angew. Chem.-Int. Edit. 47 (2008) 3874-3894.

[3] A. Rothschild, W. Menesklou, H.L. Tuller, E. Ivers-Tiffee, Electronic structure, defect chemistry, and transport properties of $SrTi_{1-x}Fe_xO_{3-y}$ solid solutions, Chem Mater 18 (2006) 3651-3659.

[4] J.R. Jurado, F.M. Figueiredo, B. Gharbage, J.R. Frade, Electrochemical permeability of $Sr_{0.7}(Ti,Fe)O_{3-\delta}$ materials, Solid State Ionics 118 (1999) 89-97.

[5] S. Steinsvik, R. Bugge, J. Gjonnes, J. Tafto, T. Norby, The defect structure of $SrTi_{1-x}Fe_xO_{3-y}$ (x=0-0.8) investigated by electrical conductivity measurements and electron energy loss spectroscopy (EELS), J. Phys. Chem. Solids 58 (1997) 969-976.

[6] P. Adler, S. Eriksson, Structural properties, Mossbauer spectra, and magnetism of perovskite-type oxides $SrFe_{1-x}Ti_xO_{3-y}$, Z Anorg Allg Chem 626 (2000) 118-124.

[7] V.V. Kharton, A.P. Viskup, A.V. Kovalevsky, J.R. Jurado, E.N. Naumovich, A.A. Vecher, J.R. Frade, Oxygen ionic conductivity of Ti-containing strontium ferrite, Solid State Ionics 133 (2000) 57-65.

[8] M.D. Drahus, P. Jakes, E. Erdem, R.-A. Eichel, Defect structure of the mixed ionic-electronic conducting $Sr[Ti,Fe]O_x$ solid-solution system - Change in iron oxidation states and defect complexation, Solid State Ionics 184 (2011) 47-51.

[9] Y. Takeda, K. Kanno, T. Takada, O. Yamamoto, M. Takano, N. Nakayama, Y. Bando, Phase Relation in the Oxygen Nonstoichiometric System, SrFeOx ($2.5 \leq x \leq 3.0$), J Solid State Chem 63 (1986) 237-249.

[10] M. Takano, T. Okita, N. Nakayama, Y. Bando, Y. Takeda, O. Yamamoto, J.B. Goodenough, Dependence of the Structure and Electronic State of SrFeOx ($2.5 \leq x \leq 3$) on Composition and Temperature, J Solid State Chem 73 (1988) 140-150.

[11] A. Sendilkumar, P.D. Babu, M.M. Raja, V.R. Reddy, A. Gupta, S. Srinath, Structural and Mossbauer Investigation of Nanocrystalline $SrFe_{1-x}Ti_xO_{3-\delta}$, J Am Ceram Soc 96 (2013) 2973-2978.

[12] A. Sendilkumar, P.D. Babu, M.M. Raja, V.R. Reddy, A. Gupta, S. Srinath, Structural and Mossbauer Investigation of Nanocrystalline $SrFe_{1-x}Ti_xO_{3-delta}$, J Am Ceram Soc 96 (2013) 2973-2978.
[13] G. Hripcsak, A.S. Rothschild, Agreement, the F-measure, and reliability in information retrieval, J Am Med Inform Assn 12 (2005) 296-298.
[14] K. Sahner, R. Moos, M. Matam, J.J. Tunney, M. Post, Hydrocarbon sensing with thick and thin film p-type conducting perovskite materials, Sensor Actuat B-Chem 108 (2005) 102-112.
[15] D.P. Fagg, V.V. Kharton, A.V. Kovalevsky, A.P. Viskup, E.N. Naumovich, J.R. Frade, The stability and mixed conductivity in La and Fe doped $SrTiO_3$ in the search for potential SOFC anode materials, J Eur Ceram Soc 21 (2001) 1831-1835.
[16] N.Q. Minh, Ceramic Fuel-Cells, J Am Ceram Soc 76 (1993) 563-588.
[17] X. Wei, G. Xu, Z.H. Ren, C.X. Xu, W.J. Weng, G. Shen, G.R. Han, Single-Crystal-like Mesoporous $SrTiO_3$ Spheres with Enhanced Photocatalytic Performance, J Am Ceram Soc 93 (2010) 1297-1305.
[18] R. Waser, R. Dittmann, G. Staikov, K. Szot, Redox-Based Resistive Switching Memories - Nanoionic Mechanisms, Prospects, and Challenges, Adv Mater 21 (2009) 2632-2663.
[19] A. Beck, J.G. Bednorz, C. Gerber, C. Rossel, D. Widmer, Reproducible switching effect in thin oxide films for memory applications, Appl Phys Lett 77 (2000) 139-141.
[20] M. Janousch, G.I. Meijer, U. Staub, B. Delley, S.F. Karg, B.P. Andreasson, Role of oxygen vacancies in Cr-doped $SrTiO_3$ for resistance-change memory, Adv Mater 19 (2007) 2232-2235.
[21] E.N. Dulov, N.G. Ivoilov, O.A. Strebkov, L.R. Tagirov, V.I. Nuzhdin, R.I. Khaibullin, S. Kazan, F.A. Mikailzade, Magnetic phase composition of strontium titanate implanted with iron ions, Materials Research Bulletin 46 (2011) 2304-2307.
[22] F.A. Kroger, H.J. Vink, Relations between the Concentrations of Imperfections in Crystalline Solids, Solid State Physics 3 (1956) 307-435.
[23] E. Bakken, N.L. Allan, T.H.K. Barron, C.E. Mohn, I.T. Todorov, S. Stolen, Order-disorder in grossly non-stoichiometric $SrFeO_{2.50}$ - a simulation study, Phys Chem Chem Phys 5 (2003) 2237-2243.
[24] M. Djermouni, A. Zaoui, S. Kacimi, B. Bouhafs, Vacancy defects in strontium titanate: Ab initio calculation, Computational Materials Science 49 (2010) 904-909.
[25] X.-X. Liao, H.-Q. Wang, J.-C. Zheng, Tuning the Structural, Electronic, and Magnetic Properties of Strontium Titanate Through Atomic Design: A Comparison Between Oxygen Vacancies and Nitrogen Doping, Journal of the American Ceramic Society 96 (2013) 538-543.
[26] R.A. Evarestov, S. Piskunov, E.A. Kotomin, G. Borstel, Single impurities in insulators: Ab initio study of Fe-doped $SrTiO_3$, Phys Rev B 67 (2003) 064101.
[27] D.A. Crandles, B. DesRoches, F.S. Razavi, A search for defect related ferromagnetism in $SrTiO_3$, J Appl Phys 108 (2010) 053908.
[28] H.J. Scheel, Historical aspects of crystal growth technology, Journal of Crystal Growth 211 (2000) 1-12.
[29] M. Ueltzen, The Verneuil flame fusion process: substances, Journal of Crystal Growth 132 (1993) 315-328.

[30] A. Meldrum, L.A. Boatner, W.J. Weber, R.C. Ewing, Amorphization and recrystallization of the ABO_3 oxides, J. Nucl. Mater. 300 (2002) 242-254.
[31] C. Sabathier, J. Chaumont, J.C. Krupa, Dose rate and temperature effects in radiation disorder creation in $SrTiO_3$, Nucl. Instrum. Methods Phys. Res. Sect. B-Beam Interact. Mater. Atoms 196 (2002) 308-314.
[32] Y. Zhang, J. Lian, C.M. Wang, W. Jiang, R.C. Ewing, W.J. Weber, Ion-induced damage accumulation and electron-beam-enhanced recrystallization in $SrTiO_3$, Phys Rev B 72 (2005) 094112.
[33] S. Soulet, J. Chaumont, C. Sabathier, J.C. Krupa, Irradiation-disorder creation in $SrTiO_3$
Journal of Materials Research 17 (2002) 9-13.
[34] S.A.E. Johansson, J.L. Campbell, K.G. Malmqvist, Particle-induced X-ray emission spectrometry (PIXE), Wiley, New York, 1995.
[35] H. Thibeau, J. Stadel, W. Cline, T.A. Cahill, On-Demand Beam Pulsing for an Accelerator, Nuclear Instruments & Methods 111 (1973) 615-617.
[36] W.J. Teesdale, J.L. Campbell, An On-Demand Beam Deflection System for Microbeam PIXE Analysis, Nucl. Instrum. Methods Phys. Res. Sect. B-Beam Interact. Mater. Atoms 52 (1990) 93-97.
[37] G.I. Johansson, Modifications of the HEX Program for last Automatic Resolution of PIXE-SPECTRA, X-Ray Spectrom. 11 (1982) 194-200.
[38] G. Basbas, W. Brandt, R. Laubert, Universal cross-sections for K-shell ionization by heavy charged particles. 2. Intermediate particle velocities, Physical Review A 17 (1978) 1655-1674.
[39] M.C. Biesinger, L.W.M. Lau, A.R. Gerson, R.S.C. Smart, Resolving surface chemical states in XPS analysis of first row transition metals, oxides and hydroxides: Sc, Ti, V, Cu and Zn, Applied Surface Science 257 (2010) 887-898.
[40] M.C. Biesinger, B.P. Payne, A.P. Grosvenor, L.W.M. Lau, A.R. Gerson, R.S. Smart, Resolving surface chemical states in XPS analysis of first row transition metals, oxides and hydroxides: Cr, Mn, Fe, Co and Ni, Applied Surface Science 257 (2011) 2717-2730.
[41] C.D. Wagner, A.V. Naumkin, A. Kraut-Vass, J.W. Allison, C.J. Powell, J.R. Rumble Jr., NIST Standard Reference Database 2003.
[42] N. Fairley, CasaXPS: Processing Software for XPS, AES, SIMS and More, Casa Software Ltd, 2009.
[43] J.D. Baniecki, M. Ishii, K. Kurihara, K. Yamanaka, T. Yano, K. Shinozaki, T. Imada, K. Nozaki, N. Kin, Photoemission and quantum chemical study of $SrTiO_3$(001) surfaces and their interaction with CO_2, Physical Review B 78 (2008) 12.
[44] S. Bhaskar, D. Allgeyer, J.A. Smythe, Depth profiling of dielectric SrTiO3 thin films by angle-resolved x-ray photoelectron spectroscopy, Appl Phys Lett 89 (2006) 254103.
[45] F. Voigts, C. Argirusis, W. Maus-Friedrichs, The interaction of H_2O with Fe-doped $SrTiO_3$(100) surfaces, Surf. Interface Anal. 43 (2011) 984-992.
[46] F. Voigts, C. Argirusis, W. Maus-Friedrichs, The interaction of CO_2 and CO with Fe-doped $SrTiO_3$(100) surfaces, Surf. Interface Anal. 44 (2012) 301-307.
[47] D.J. Miller, M.C. Biesinger, N.S. McIntyre, Interactions of CO_2 and CO at fractional atmosphere pressures with iron and iron oxide surfaces: one possible mechanism for surface contamination?, Surf. Interface Anal. 33 (2002) 299-305.

[48] S.T. Jackson, R.G. Nuzzo, Determining hybridization differences for amorphous carbon from the XPS C 1s envelope, Applied Surface Science 90 (1995) 195-203.
[49] P.A.W. van der Heide, Q.D. Jiang, Y.S. Kim, J.W. Rabalais, X-ray photoelectron spectroscopic and ion scattering study of the $SrTiO_3$(001) surface, Surface Science 473 (2001) 59-70.
[50] S. Azad, M.H. Engelhard, L.Q. Wang, Adsorption and reaction of CO and CO_2 on oxidized and reduced $SrTiO_3$(100) surfaces, J. Phys. Chem. B 109 (2005) 10327-10331.
[51] M.E. Pilleux, C.R. Grahmann, V.M. Fuenzalida, Hydrothermal Strontium-Titanate Films on Titanium - An XPS and AES Depth-Profiling Study Journal of the American Ceramic Society 77 (1994) 1601-1604.
[52] K. Szot, W. Speier, U. Breuer, R. Meyer, J. Szade, R. Waser, Formation of micro-crystals on the (100) surface of $SrTiO_3$ at elevated temperatures, Surface Science Reports 460 (2000) 112-128.
[53] R.M. Tromp, M. Copel, M.C. Reuter, M.H. Vonhoegen, J. Speidell, R. Koudijs, A New 2-Dimensional Particle Detector for a Toroidal Electrostatic Analyzer, Review of Scientific Instruments 62 (1991) 2679-2683.
[54] R.E. Watson, J.W. Davenport, M.L. Perlman, T.K. Sham, Madelung Effects at Crystal-Surfaces - Implications for Photoemission, Physical Review B 24 (1981) 1791-1797.
[55] J. Shin, S.V. Kalinin, H.N. Lee, H.M. Christen, R.G. Moore, E.W. Plummer, A.P. Baddorf, Surface stability of epitaxial $SrRuO_3$ thin films in vacuum, J. Mater. Res. 19 (2004) 3447-3450.
[56] C. Sabathier, J. Chaumont, S. Rouziere, A. Traverse, Characterisation of Ti and Sr atomic environments in $SrTiO_3$ before and after ion beam irradiation by X-ray absorption spectroscopy, Nucl. Instrum. Methods Phys. Res. Sect. B-Beam Interact. Mater. Atoms 234 (2005) 509-519.
[57] W. Jung, H.L. Tuller, Investigation of surface Sr segregation in model thin film solid oxide fuel cell perovskite electrodes, Energy Environ. Sci. 5 (2012) 5370-5378.
[58] Y. Chen, W.C. Jung, Y. Kuru, H. Tuller, B. Yildiz, Chemical, electronic and nanostructure dynamics on $Sr(Ti_{1-x}Fe_x)O_3$ thin-film surfaces at high temperature, ECS Transactions 35 (2011) 2409-2416.
[59] L.V. Goncharova, D.G. Starodub, E. Garfunkel, T. Gustafsson, V. Vaithyanathan, J. Lettieri, D.G. Schlom, Interface structure and thermal stability of epitaxial $SrTiO_3$ thin films on Si(001), J. Applied Physics 100 (2006) 014912.

Chapter 5. Local structure analysis of Fe-implanted STO by X-ray absorption near edge structure spectroscopy

In Chapter 4, we summarized our results from Rutherford backscattering spectrometry with an unusual loss of Sr during implantation and post-implantation anneals at high temperatures in an oxygen environment. Sr loss is dependent on the Fe implantation dose and most noticeable at the highest implantation doses and after 350^{o}C anneal. Local chemical environments of implanted and annealed samples were evaluated with X-ray absorption near edge structure (XANES) spectroscopy. While XPS allows us to monitor changes on the surface, XANES gives us additional information about structural changes within the whole layer thickness affected by implantation. Due to the chemical selectivity of X-ray absorption spectroscopy, we can characterize the local surrounding of Ti, Fe and O atoms independently. XANES is particularly suitable to study ion-irradiated systems, which can be highly disordered or even amorphous, since no-long-range crystal order is necessary to get information about local coordination and ordering.

5.1 X-ray absorption near edge structure experimental procedure

X-ray absorption near edge structure spectroscopy is a powerful analytical method. It provides information about the oxidation state and local symmetry of the absorbing atom using bright, tunable and highly collimated synchrotron X-rays.

XANES experiments were conducted at the Canadian Light Source (CLS) (Saskatoon, Canada) and at the Advanced Photon Source (APS) at the Argonne National Laboratory (Argonne, IL, USA). Both are insertion devices based on the third generation electron storage rings. CLS has a circumference of 171 m and operates at 2.9 GeV with a storage beam current 200–300 mA. APS has a larger diameter of the storage ring (approximately 1100 m) operating at 7 GeV.

O K-edge, Ti $L_{3,2}$-edge and Fe $L_{3,2}$-edge XANES experiments were performed at the CLS at the high resolution Spherical Grating Monochromator (SGM) beamline which

uses a 45 mm planar undulator and three gratings covering an X-ray photon energy range from 250 to 2000 eV. It provides resolving power greater than 5000 E/ΔE at energies below 1500 eV and better than 10000 E/ΔE at the O K-edge. The photon energy was calibrated at the C K-edge at 284.2 eV.

Ti K-edge and Fe K-edge were measured at the APS at the PNC/XSD beamline (20-BM). The beamline uses a Si double-crystal monochromator to cover a photon energy range of ~ 5-25 keV and offers resolving power greater than 7000 E/ΔE. The double-crystal monochromator photon energy was calibrated at the Fe K-edge threshold of an iron foil at 7110.6 eV.

The absorption spectra were collected in total fluorescence yield (TFY) and total electron yield (TEY) at the CLS. XANES spectra were collected in TFY mode using a Si drift fluorescence detector. TEY is more surface sensitive than TFY due to the short escape depth of electrons in matter (for the same reason which explains the surface sensitivity of XPS method). In XANES of STO samples, the use of total fluorescence yield and total electron yield allows discerning the bulk and surface signals, respectively. However, significant charging of STO samples during acquisition caused distortion to XANES spectra collected in TEY mode in some cases.

All XANES spectra were normalized to the intensity of the incident beam I_0, measured as the current emitted from a refreshing gold mesh simultaneously with spectrum acquisition. Continuous background was subtracted from data as an extrapolated linear curve fitted in the pre-edge area. In some cases it was impossible (or impractical), and the spectra were normalized to unity by the intensity of the first sharp intense peak (traditionally referred as the "white line"). For a consistent data processing and better comparison of spectra they were normalized to unity above absorption edge (~40 eV above the white line). For better interpretation of XANES spectra at the Fe K-edge, FEFF9 calculations were performed using Density Functional Theory (DFT) together with the Generalized Gradient Approximation (GGA). The calculations are based on the Real Space Multiple-Scattering (RSMS) formalism which takes advantage of the close connection between XAS and electronic structure [1-4].

5.2 Ti K-edge XANES

Ti K-edge XANES spectra of the Fe-doped STO samples exhibit a pattern typical for the STO cubic perovskite structure (Fig. 5.1). The main x-ray absorption occurs due to the dipole-allowed excitation of the 1*s* electron to the states with *p* character [5]. White line intensity (the sharp spike at the threshold) decreased slightly in spectra of STO-Fe2e16 and STO-Fe2e16-350C samples comparing to un-implanted STO crystal. The influence of the iron implantation and the post-implantation annealing is mostly noticeable in the pre-edge area (Fig. 5.1, inset). For perovskite structure, a group of four feature $A_{1,2}$ and $B_{1,2}$ can be distinguished in the pre-edge area of the Ti K-edge XANES which have dipole and quadrupole origin [5, 6]. The pre-peaks $A_{1,2}$ are known to be sensitive to displacements of the absorbing atoms from the centrally-symmetric position relative to neighbouring atoms for perovskites [7]. In STO-Fe2e16 and STO-Fe2e16-350C, iron implantation and subsequent annealing leads to an increase in the intensity of the $A_{1,2}$ features compared to the un-implanted STO. Our observations of growth of the $A_{1,2}$ pre-edge peaks intensity resulting from Fe doping is consistent with the findings of Ghaffari *et al.* [8] and Vracar *et al.* [5] who investigated $SrTi_{1-x}Fe_xO_{3-\delta}$ powders ($0 \leq x \leq 1$).

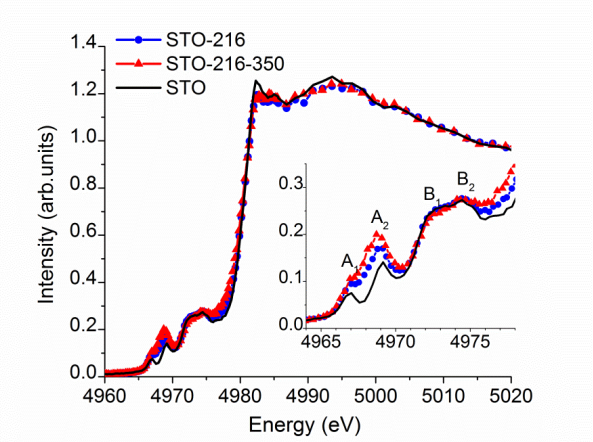

Figure 5.1. Ti K-edge XANES spectra of virgin STO, STO-Fe2e16 and STO-Fe2e16-350C samples. Inset shows enlarged pre-edge features.

5.3 Ti L-edge XANES

Ti $L_{3,2}$-edge XANES of STO samples are shown in Figure 5.2. The Ti $L_{3,2}$-edge spectra are dominated by dipole transitions between Ti 2*p* and Ti 3*d* levels. The position and shape of the L-edge resonances are sensitive to the local electronic structure, symmetry and the oxidation state [9]. The $L_{3,2}$ edges of 3*d* metals are dominated by very intense "white line" features due to *p-d* dipole transitions into the unoccupied *d* states. This transition is governed by a combined effect of the dominant crystal field splitting, band formation, spin orbit coupling and final state exchange interaction [9, 10]. Crystal field splitting of the *d* states can be observed as a splitting of the "white line" feature related to the t_{2g} and e_g final states in the octahedral field as is the case in STO.

Ti $L_{3,2}$-edge spectra collected in TFY mode clearly reflect the influence of ion implantation (Fig. 5.2(a)). There is a noticeable broadening and shift of the e_g peaks in the spectrum of the implanted STO-Fe2e16 sample suggesting local distortion. The e_g peak position are 461.2 eV and 460.5 eV for un-implanted STO and STO-Fe2e16 sample, respectively. During ion irradiation, a large amount of defects, mainly oxygen vacancies, was produced in the STO crystal [11]. To compensate for this, Ti ions move away from the oxygen vacancies and increase the effective Ti-O distance, and therefore e_g peaks shift to lower energies [12]. This is accompanied by a distortion of the O_h symmetry locally as has been shown the case in the Ti $L_{3,2}$ edge of TiO_2 rutile and anatase [13].

In the spectrum of the annealed STO-Fe2e16-350C sample, the peak narrows and the position of e_g peaks moves back toward that of the un-implanted STO crystal. This indicates that oxygen anneal removes most of the oxygen vacancies but not completely.

Spectra collected in TEY mode display the shift of e_g peaks for STO-Fe2e16 and STO-Fe2e16-350C samples indicating that the oxygen vacancies in the near-surface area of the samples remained even after annealing in the oxygen atmosphere (Fig. 5.2(b)).

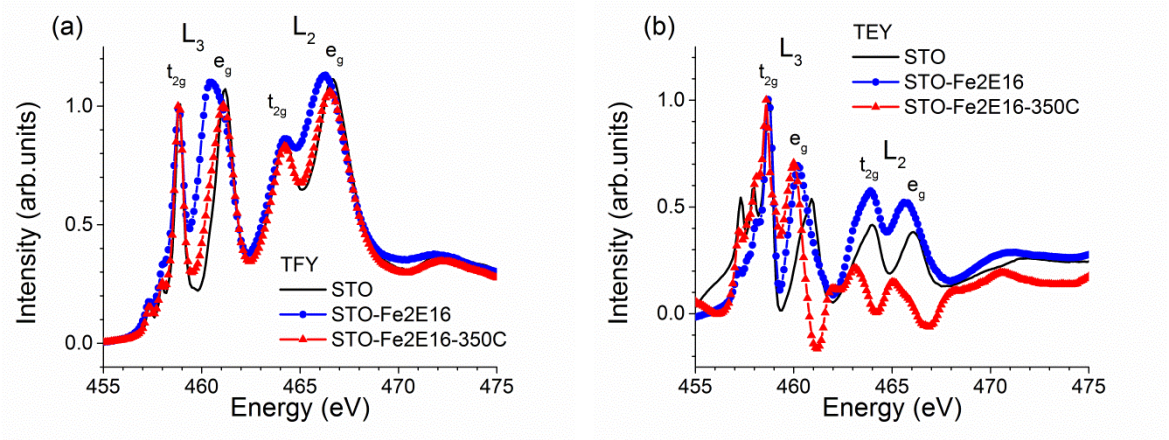

Figure 5.2. Ti $L_{3,2}$-edge XANES spectra of virgin STO, STO-Fe2e16 and STO-Fe2e16-350C samples: (a) collected in total fluorescence yield; (b) collected in total electron yield.

5.4 Fe K-edge XANES

Fe K-edge XANES spectra were collected for STO samples with the highest Fe dose. No iron peaks were detected in STO samples prior to implantation. Figure 5.3 shows the Fe K-edge XANES of the implanted STO-Fe2e16 and annealed STO- Fe2e16-350C. For comparison, the spectra of iron foil and iron oxide Fe_2O_3 are also presented for comparison.

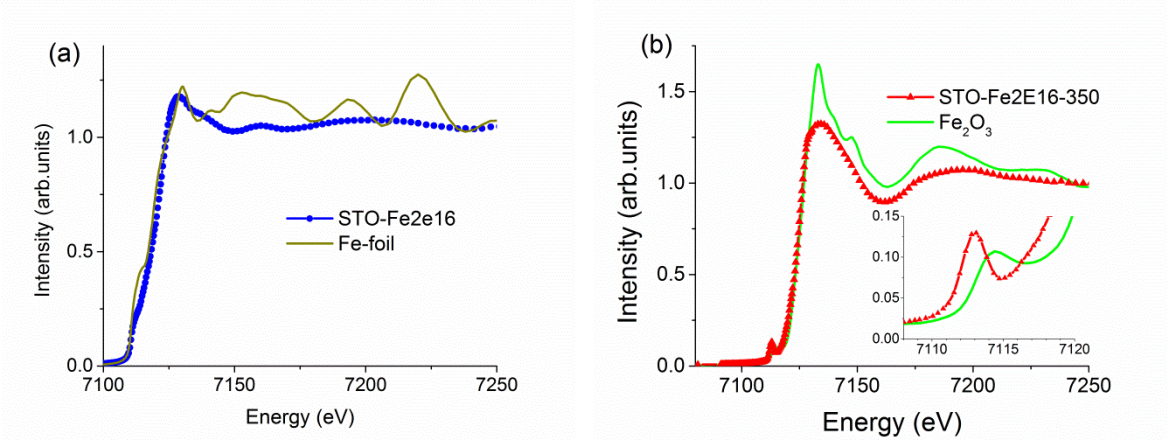

Figure 5.3. Fe K-edge TEY XANES spectra of STO samples: (a) implanted sample STO-Fe2e16; (b) implanted and annealed sample STO-Fe2e16-350C. Iron foil and iron oxide Fe_2O_3 spectra are shown for comparison.

There is a distinct difference between the Fe K-edge spectra of STO- Fe2e16 and STO- Fe2e16-350C. The spectrum of STO-Fe2e16 has a shoulder at ~7112 eV in the pre-

edge region which indicates that in the as-implanted sample iron is in the Fe^0 oxidation state and is metallic (Fig. 5.3(a)). The spectrum of the STO- Fe2e16-350C has a sharp pre-edge peak at ~7113 eV, demonstrating that iron becomes Fe^{3+} after annealing in oxygen atmosphere (Fig. 5.3(b)). The broadening and disappearance of the oscillations above the absorption edge strongly suggest that implanted iron does not have long-range order in either of the samples.

In *3d* metals, the pre-edge feature in the K-edge range is attributed to the *s-d* quadrupole transition due to *d-p* mixing. The pre-edge peaks provides information about oxidation state and the local coordination geometry of the metal atom (e.g. tetrahedral versus octahedral) [13, 14]. A comparison with the Fe_2O_3 standard spectrum (Fig. 5.3(b) inset) shows that the pre-edge feature of STO-Fe2e16-350C is more intense and moves to a lower energy, presenting further evidence that the Fe sites of STO-Fe2e16-350C increasingly deviate from the centrosymmetric O_h geometry [14, 15].

5.5 Fe L-edge XANES

Fe $L_{3,2}$-edge spectra of STO samples implanted with different Fe doses are shown in Figure 5.4. Note that Fe concentration was below the detection level in STO-Fe2e14 and STO-Fe2e14-350C samples. However for higher implantation doses, iron peaks were clearly present in Fe $L_{3,2}$-edge spectra.

As I mentioned before, $L_{3,2}$-edge spectra of the transition metals are sensitive to the local electronic structure, symmetry and the oxidation state [9]. The shape of the Fe $L_{3,2}$-edge spectra confirms the conclusion about the iron oxidation state before and after annealing deduced from the Fe K-edge XANES. The lack of splitting of the "white line" feature of Fe $L_{3,2}$ absorption peaks showed that iron is in the metallic state Fe^0 in the as-implanted strontium titanate samples, STO-Fe8e14 and STO-Fe2e16 (Fig. 5.4(a)). After annealing in oxygen atmosphere at 350°C, the Fe $L_{3,2}$ absorption peaks of the STO-Fe8e14-350C and STO-Fe2e16-350C sample change into doublets, characteristic of Fe^{2+} /Fe^{3+} states [16].

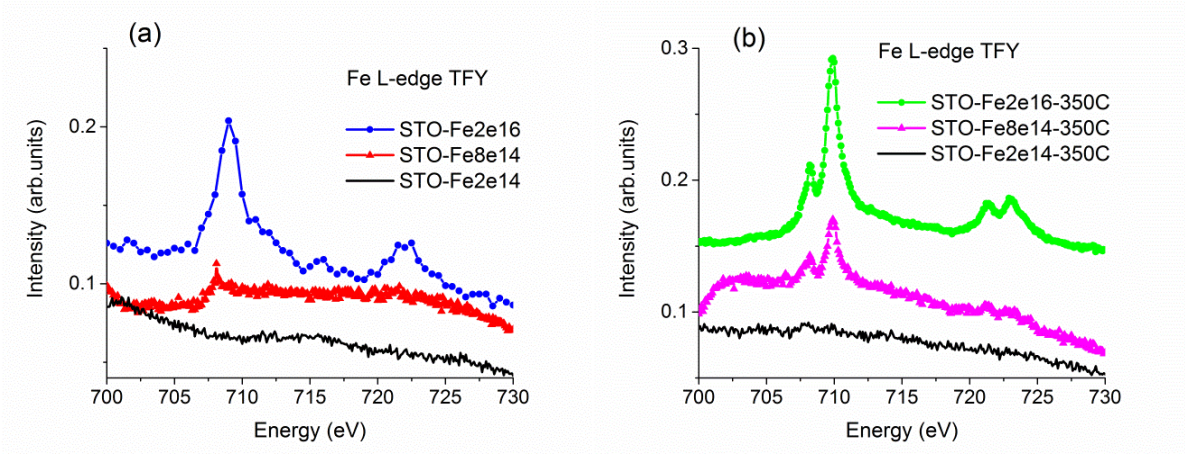

Figure 5.4. (a) Fe $L_{3,2}$-edge XANES spectra of STO implanted with different Fe^{+} doses; (b) Fe $L_{3,2}$-edge XANES spectra of STO implanted with different doses and annealed, collected at the total fluorescent yield.

The Fe $L_{3,2}$-edge XANES spectra are easier to analyze using the example of STO samples with the highest implantation dose (Fig. 5.5). Fe $L_{3,2}$-edge spectra of STO-Fe2e16 and STO-Fe2e16-350C were collected in the total fluorescent and in the total electron yields where latter is more surface sensitive compared to the former. TFY and TEY Fe $L_{3,2}$-edge spectra of STO-Fe2e16 are identical. However, the intensity ratios of the doublets are different in TFY and TEY spectra of STO-Fe2e16-350C. The intensity distributions of these doublets show that the first near edge peak of TEY is higher than that of TFY spectra. This feature is characteristic of Fe^{2+} and indicates that the iron oxidation state in the annealed sample of STO-Fe2e16-350C corresponds to dominantly Fe^{2+} on TEY spectrum and Fe^{3+} on TFY spectrum [17]. Since TEY is more surface sensitive compared to the TFY, this corresponds to higher oxygen deficiency near the surface area of STO crystal compared to its bulk. This is a fairly unusual observation since STO-Fe2e16-350C was annealed in an oxygen atmosphere.

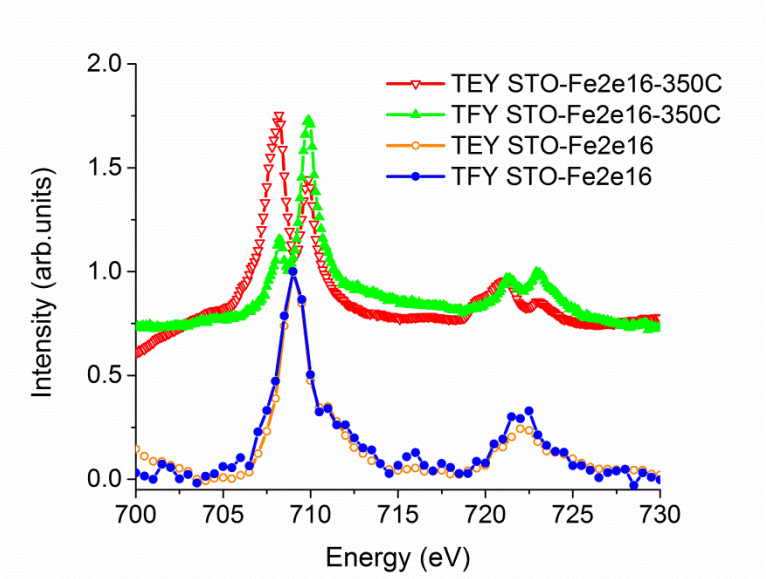

Figure 5.5. Fe $L_{3,2}$-edge XANES spectra of STO-Fe2e16 and STO-Fe2e16-350C collected in total fluorescence yield and in total electron yield.

5.6 O K-edge XANES

Figure 5.6(a) shows O K-edge TFY spectra of STO samples implanted with different Fe doses. O K-edge XANES of virgin STO had four sharp features (A-D) typical for strontium titanate crystal with well-defined cubic crystal structure [18, 19]. In STO there is a tightly bonded octahedral arrangement of O atoms around the Ti atom (TiO_6^{8-} cluster). The O-K edge fine structure is produced by O 1s→2p transitions and is proportional to the unoccupied O p-density of states in the presence of a core hole. In comparison to virgin STO crystal, absorption features became wider and less intense as Fe implantation dose increased from 2×10^{14} to 2×10^{16} Fe ion/cm^2, when irradiation damage created distortion in TiO_6^{8-} octahedral geometry.

O K-edge spectra of STO samples implanted with different Fe doses and annealed in oxygen were almost identical implying that there was similarity in local structure of all implanted and annealed samples (Fig. 5.6(b)).

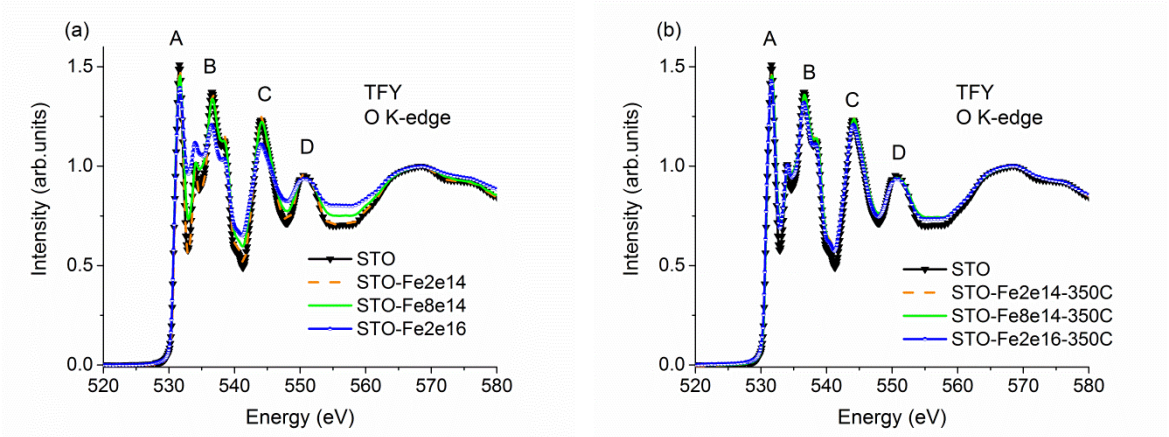

Figure 5.6. O K-edge XANES spectra collected in total fluorescence yield of: (a) STO samples implanted with different Fe^{+} doses, and (b) STO samples implanted and annealed in oxygen atmosphere at 350°C.

Figure 5.7(a) presents the O K-edge TFY spectra of virgin STO, STO-Fe2e16 and STO-Fe2e16-350C samples. As can be seen from the comparison of implanted and un-implanted STO crystals, Fe implantation at 2×10^{16} ion/cm^2 dose introduces some degree of disordering into the STO crystal structure, though annealing at oxygen at 350°C healed the implantation damage. However, the comparison of O K-edge TFY spectra of virgin STO and STO-Fe2e16-350C samples showed that there was little difference between their crystal structure. This is consistent with our RBS results reported in Chapter 4. Electron energy loss near-edge structure (EELNES) study of SrTiO3 crystals have shown that peaks B and C reflect the changes in the local atomic and electronic structure [20]. The calculations showed that in presence of grain boundaries, dopants and defects relative intensity of the features changed as compared to the peak. In particular the study demonstrated that the shape of peak B with prominent shoulders on both sides and decrement of its intensity corresponded to oxygen vacancies in STO structure.

Unfortunately, there was significant charging of the STO sample surface during spectrum acquisition, which made XANES spectra collected in total electron yield mostly useless for analysis. Although the edge peaks were at the same energy on TFY and TEY O K-edge spectra, the rest of the TEY features were completely distorted (Fig. 5.7(b)).

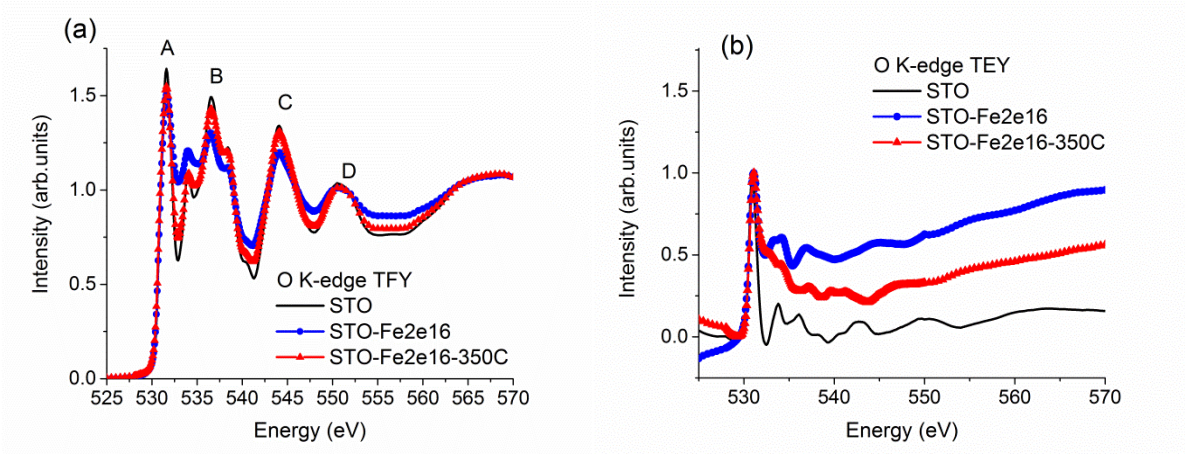

Figure 5.7. O K-edge XANES spectra of virgin STO, STO-Fe2e16 and STO-Fe2e16-350C samples: (a) collected in total fluorescence yield; (b) collected in total electron yield.

5.7 Comparison of experimental data and FEFF calculations.

As was demonstrated by O K-edge, Ti K-edge and Ti L-edge XANES spectra of STO samples, Fe ion irradiation resulted in disordering and defects in STO crystals. Though annealing in O_2 atmosphere improved crystal structure, there were significant differences observed between XANES spectra of virgin STO and STO-Fe2e16-350C. It shows that thermal treatment the system did not restore it to initial state but a new phase was formed in the ion implanted area.

Fe K-edge and Fe L-edge spectra indicated that the oxidation state of implanted Fe changed after O_2 anneal at 350°C from metallic Fe^0 state to Fe^{3+} state (with Fe^{2+} state in the near-surface region).

The studies of $SrTi_{1-x}Fe_xO_{3-\delta}$ system have shown that Fe can accept the oxidation states between Fe^{2+}, Fe^{3+} and Fe^{4+}. Dulov et al. [21] have studied the phase composition of strontium titanate implanted with iron using Mossbauer spectroscopy. They have identified Fe^{3+} states in their STO samples and observed the formation of α-Fe metallic nanoparticles of ~ 5nm size in STO already at implantation dose 7.5×10^{16} Fe ions/cm^2. Apparently in the case of the lower implantation dose used in my study, Fe did not aggregate to nanoparticles. The mixture of Fe^{3+} and Fe^{4+} states has been also observed in $SrTi_{1-x}Fe_xO_{3-\delta}$ powder samples studied by Mössbauer spectroscopy [22]. In powder

samples of $SrTi_{1-x}Fe_xO_{3-\delta}$ solid solutions studied by the electron paramagnetic resonance method, Fe oxidation states were +2, +3 and +4 [23]. These discrepancies can be explained by different experimental conditions.

To further investigate the local symmetry of iron in STO samples, computer simulations were performed for several model compounds including $SrFeO_3$, $Sr_8Fe_8O_{23}$, $Sr_8Ti_5Fe_3O_{23}$, $Sr_8Ti_3Fe_5O_{23}$, FeO, Fe_2O_3, Fe_3O_4, and Fe foil. The XANES spectra were calculated self-consistently by the Real Space Multiple Scattering program of FEFF9 [1-3]. The clusters of 40 atoms (or 8 unit cells) with the following group symmetry were used for simulations of $SrTi_{1-x}Fe_xO_{3-\delta}$. The cluster assumed a cubic perovskite structure where some of Ti atoms were replaced by Fe atoms. The experimental and calculated Fe K-edge XANES are displayed in Figures 5.8 and 5.9.

The experimental Fe K-edge XANES of Fe foil follows the calculated spectrum of the Fe *bcc* structure with peaks A, B, C, D, E, and F coincided closely (Fig. 5.8). However the experimental Fe K-edge spectrum of STO-Fe2e16 is much smoother indicating the absence of long-range ordering of Fe in the implanted STO sample.

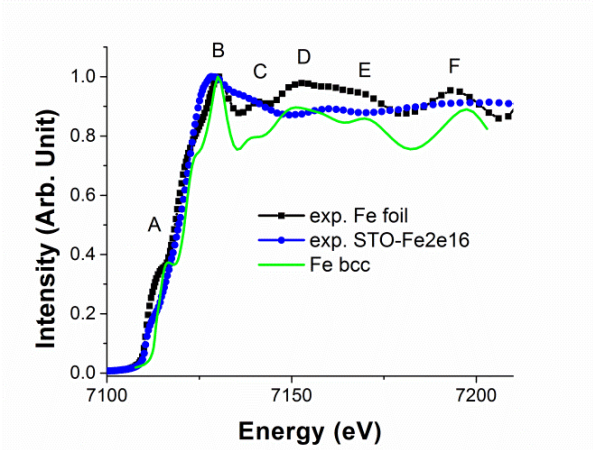

Figure 5.8. Experimental Fe K-edge XANES of STO-Fe2e16 and Fe foil and FEFF calculations for Fe foil with bcc unit cell.

As shown in Figure 5.9(a), the shape of the Fe K-edge XANES of the annealed sample STO-Fe2e16-350C differs from both FeO and Fe_2O_3 standards, but follows that of Fe_3O_4, implying the presence of two oxidation state Fe^{2+} and Fe^{3+}. However, analysis of

the pre-edge area (Fig. 5.9(b)) demonstrates the difference in the local structure of Fe in STO-Fe2e16-350C and all measured standard oxide samples.

Additional information about local chemical environment can be obtained from FEFF calculations. The Fe K-edge XANES spectrum of the annealed sample STO-Fe2e16-350C (Fig. 5.9(c)) closely follows those of the $SrFeO_{3-\delta}$ and $SrTi_{1-x}Fe_xO_{3-\delta}$ calculated for 40-atom (or 2×2×2 lattice cell) supercell by FEFF program [1-4]. It should be noted that $SrFeO_3$ structure does not correspond to the experimental XANES of STO-Fe2e16-350C. The peaks B, C, and D which can be observed in the calculated spectra of $SrFeO_{3-\delta}$, $Sr_8Ti_5Fe_3O_{23}$ and $Sr_8Ti_3Fe_5O_{23}$ are not very pronounced in the experimental Fe K-edge XANES of STO-Fe2e16-350C. Fe ions are distributed more randomly in STO-Fe2e16-350C sample, in other words there is no relationship in Fe positions in neighboring cells.

Close examination of the pre-edge area showed that the best agreement is with the XANES of $Sr_8Ti_3Fe_5O_{23}$ cluster where there is more Fe than Ti (Fig. 5.9(d)). Thus iron and titanium can occupy the same crystallographic site in STO-Fe2e16-350C sample. Position of the pre-edge feature A for STO-Fe2e16-350C sample is moved to higher energy (~7113 eV) compare to those of the $SrFeO_{3-\delta}$ and $Sr_8Ti_3Fe_5O_{23}$ (~7112.7 eV) clearly indicating that there is distortion of O_h symmetry at the Fe site, and there is a presence of vacancy within the structure [24]. Another cause of the detected differences arises from the choice of the 40-atom cell in FEFF calculations. Previous studies have shown that such cell is possibly too small to correctly reflect the screening of the periodically repeated oxygen vacancies [25].

A certain amount of oxygen vacancies should still exist, even after heating, to maintain charge neutrality due to the different oxidation states of titanium (Ti^{4+}) and substituting iron (Fe^{3+}). The studies of $SrTi_{1-x}Fe_xO_{3-\delta}$ structure have shown that oxygen vacancies can demonstrate short-range ordering, and no evidence for long-range ordering has been found [26-28]. As a result the channeling RBS method evaluates the implanted area in the STO-Fe2e16-350C sample as a rather disordered region (see Chapter 4).

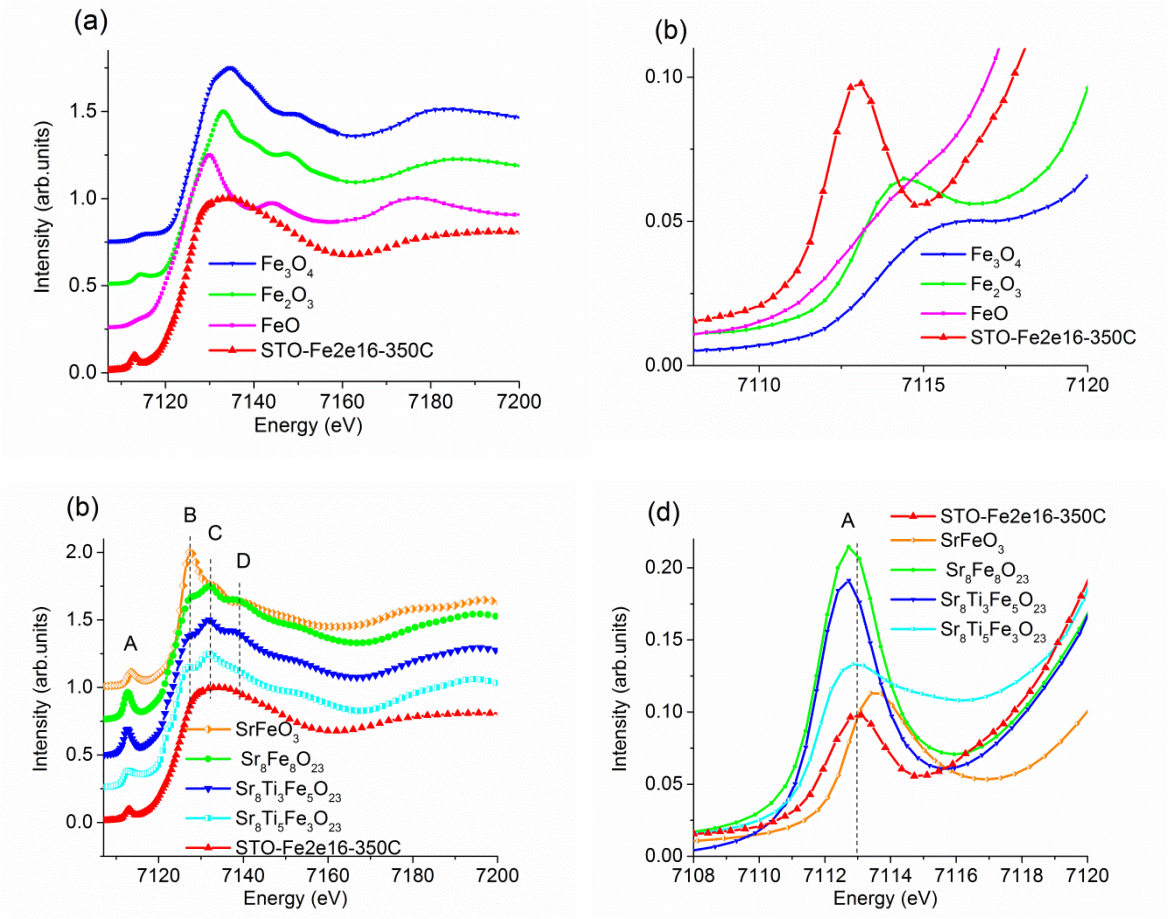

Figure 5.9. Comparison of the Fe K-edge XANES of STO-Fe2e16-350C sample, iron oxides and FEFF calculation for $SrTi_{1-x}Fe_xO_{3-\delta}$ clusters(a) Experimental Fe K-edge XANES of STO-Fe2e16-350C and several oxide FeO, Fe_2O_3, and Fe_3O_4; (b) Enlarged pre-edge area; (c) Experimental Fe K-edge XANES of STO-Fe2e16-350C and FEFF calculations for several mixed oxide clusters: $SrFeO_3$, $Sr_8Fe_8O_{23}$, $Sr_8Ti_5Fe_3O_{23}$ and $Sr_8Ti_3Fe_5O_{23}$; (d) Enlarged pre-edge peaks.

In summary, the results obtained by XANES spectroscopy revealed the structural and chemical transformation of STO crystals following Fe ion irradiation and post-implantation annealing in oxygen atmosphere. The effect of Fe implantation on crystal structure was clearly seen in O K-edge and Ti K- and L-edge spectra. With increase of implantation dose, amount of oxygen vacancies and the disordering in STO structure increased. Anneal in O_2 at 350°C improved crystallinity of implanted samples. Fe K- and L-edge XANES spectra revealed the oxidation state and the local structure of the implanted iron. Iron was in metallic state (Fe^0) in as-implanted samples. Annealing in O_2

led to oxidation of iron. Comparison of Fe L-edge XANES spectra collected in TEY and TFY showed the difference in Fe oxidation state in the bulk and the surface area. After annealing, iron was in the Fe^{3+} state in bulk of the STO samples; in the surface area the oxidation state of iron was Fe^{2+}. The finding indicated that there were more oxygen vacancies at the surface even after annealing in oxygen atmosphere. The smoothed shape of Fe K-edge XANES as compared to the spectrum of the standard Fe foil showed absence of the long-range ordering of iron in as-implanted STO samples. As followed from comparison of Fe K-edge XANES with results of the FEFF simulations, annealing caused Fe to incorporate in the STO structure, substituting Ti and forming clusters of $Sr_8Ti_3Fe_5O_{23}$.

References

[1] J.J. Rehr, R.C. Albers, Theoretical approaches to x-ray absorption fine structure, Reviews of Modern Physics 72 (2000) 621-654.
[2] J.J. Rehr, J.J. Kas, M.P. Prange, A.P. Sorini, Y. Takimoto, F. Vila, Ab initio theory and calculations of X-ray spectra, Comptes Rendus Physique 10 (2009) 548-559.
[3] J.J. Rehr, J.J. Kas, F.D. Vila, M.P. Prange, K. Jorissen, Parameter-free calculations of X-ray spectra with FEFF9, Physical Chemistry Chemical Physics 12 (2010) 5503-5513.
[4] J.J. Rehr, A.L. Ankudinov, Progress in the theory and interpretation of XANES, Coord. Chem. Rev. 249 (2005) 131-140.
[5] M. Vracar, A. Kuzmin, R. Merkle, J. Purans, E.A. Kotomin, J. Maier, O. Mathon, Jahn-Teller distortion around Fe^{4+} in $Sr(Fe_xTi_{1-x})O_{3-\delta}$ from x-ray absorption spectroscopy, x-ray diffraction, and vibrational spectroscopy, Phys Rev B 76 (2007) 174107.
[6] T. Yamamoto, T. Mizoguchi, I. Tanaka, Core-hole effect on dipolar and quadrupolar transitions of $SrTiO_3$ and $BaTiO_3$ at Ti edge, Phys Rev B 71 (2005) 245113.
[7] R.V. Vedrinskii, V.L. Kraizman, A.A. Novakovich, P.V. Demekhin, S.V. Urazhdin, Pre-edge fine structure of the 3d atom K x-ray absorption spectra and quantitative atomic structure determinations for ferroelectric perovskite structure crystals, Journal of Physics-Condensed Matter 10 (1998) 9561-9580.
[8] M. Ghaffari, T. Liu, H. Huang, O.K. Tan, M. Shannon, Investigation of local structure effect and X-ray absorption characteristics (EXAFS) of Fe (Ti) K-edge on photocatalyst properties of $SrTi_{(1-x)}Fe_xO_{(3-\delta)}$, Materials Chemistry and Physics 136 (2012) 347-357.
[9] F. de Groot, A. Kotani, Core level spectroscopy of solids, CRC Press, Boca Raton, 2008.
[10] T.K. Sham, Multiplet splitting (broadening) of the Ru $L_{2,3}$ edge white lines in the X-ray absorption near edge spectra of $Ru(NH_3)_6Cl_3$, Journal of Chemical Physics 83 (1985) 3222-3224.
[11] J.F. Ziegler, J.P. Biersack, U. Littmark, The stopping and range of ions in solids, New York, Pergamon, 1985.
[12] G.-z. Zhu, G. Radtke, G.A. Botton, Bonding and structure of a reconstructed (001) surface of $SrTiO_3$ from TEM, Nature 490 (2012) 384-387.
[13] F.M.F. de Groot, XANES spectra of transition metal compounds, 14th International Conference on X-Ray Absorption Fine Structure (XAFS14), Proceedings 190 (2009) 9.
[14] T.E. Westre, P. Kennepohl, J.G. DeWitt, B. Hedman, K.O. Hodgson, E.I. Solomon, A multiplet analysis of Fe K-edge 1s$\rightarrow$3d pre-edge features of iron complexes, Journal of the American Chemical Society 119 (1997) 6297-6314.
[15] L.X. Chen, T. Liu, M.C. Thurnauer, R. Csencsits, T. Rajh, Fe_2O_3 nanoparticle structures investigated by X-ray absorption near-edge structure, surface modifications, and model calculations, J. Phys. Chem. B 106 (2002) 8539-8546.
[16] J. Leveneur, G.I.N. Waterhouse, J. Kennedy, J.B. Metson, D.R.G. Mitchell, Nucleation and Growth of Fe Nanoparticles in SiO_2: A TEM, XPS, and Fe L-Edge XANES Investigation, Journal of Physical Chemistry C 115 (2011) 20978-20985.
[17] S.L. Yang, D.N. Wang, G.X. Liang, Y.M. Yiu, J.J. Wang, L.J. Liu, X.L. Sun, T.K. Sham, Soft X-ray XANES studies of various phases related to $LiFePO_4$ based cathode materials, Energy & Environmental Science 5 (2012) 7007-7016.

[18] F.M.F. de Groot, J. Faber, J.J.M. Michiels, M.T. Czyzyk, M. Abbate, J.C. Fuggle, Oxygen 1s x-ray absorption of tetravalent titanium oxides: A comparison with single-particle calculations, Phys Rev B 48 (1993) 2074-2080.
[19] D.A. Muller, N. Nakagawa, A. Ohtomo, J.L. Grazul, H.Y. Hwang, Atomic-scale imaging of nanoengineered oxygen vacancy profiles in $SrTiO_3$, Nature 430 (2004) 657-661.
[20] T. Mizoguchi, Y. Sato, J.P. Buban, K. Matsunaga, T. Yamamot, Y. Ikuhara, Sr vacancy segregation by heat treatment at SrTiO3 grain boundary, Appl Phys Lett 87 (2005) 241920.
[21] E.N. Dulov, N.G. Ivoilov, O.A. Strebkov, L.R. Tagirov, V.I. Nuzhdin, R.I. Khaibullin, S. Kazan, F.A. Mikailzade, Magnetic phase composition of strontium titanate implanted with iron ions, Materials Research Bulletin 46 (2011) 2304-2307.
[22] A. Sendilkumar, P.D. Babu, M.M. Raja, V.R. Reddy, A. Gupta, S. Srinath, Structural and Mossbauer Investigation of Nanocrystalline $SrFe_{1-x}Ti_xO_{3-\delta}$, Journal of the American Ceramic Society 96 (2013) 2973-2978.
[23] M.D. Drahus, P. Jakes, E. Erdem, R.-A. Eichel, Defect structure of the mixed ionic-electronic conducting $Sr[Ti,Fe]O_x$ solid-solution system - Change in iron oxidation states and defect complexation, Solid State Ionics 184 (2011) 47-51.
[24] T.E. Westre, P. Kennepohl, J.G. DeWitt, B. Hedman, K.O. Hodgson, E.I. Solomon, A multiplet analysis of Fe K-edge 1s->3d pre-edge features of iron complexes, Journal of the American Chemical Society 119 (1997) 6297-6314.
[25] J. Carrasco, F. Illas, N. Lopez, E.A. Kotomin, Y.F. Zhukovskii, R.A. Evarestov, Y.A. Mastrikov, S. Piskunov, J. Maier, First-principles calculations of the atomic and electronic structure of F centers in the bulk and on the (001) surface of $SrTiO_3$ Phys Rev B 73 (2006) 064106.
[26] J.R. Jurado, F.M. Figueiredo, B. Gharbage, J.R. Frade, Electrochemical permeability of $Sr_{0.7}(Ti,Fe)O_{3-delta}$ materials, Solid State Ionics 118 (1999) 89-97.
[27] P. Adler, S. Eriksson, Structural properties, Mossbauer spectra, and magnetism of perovskite-type oxides $SrFe_{1-x}Ti_xO_{3-y}$, Z Anorg Allg Chem 626 (2000) 118-124.
[28] T.C. Gibb, P.D. Battle, S.K. Bollen, R.J. Whitehead, Investigation of the crystal and magnetic structure of the perovskite system Sr_2FeTiO_6 by Mossbauer spectrosocpy and neutron diffraction, Journal of Materials Chemistry 2 (1992) 111-114.

Chapter 6. Analysis of N- and O- implanted highly oriented pyrolytic graphite

6.1 Introduction

The role of defects in determining the electronic structure of graphite is crucial to our understanding of many important properties, including enhanced catalytic activity and defect-induced magnetism [1-7]. The work presented here was inspired by several independent studies where defect-induced ferromagnetism was observed in various graphite materials, such as H^+ and C^+ implanted graphite, carbon nanofoams and graphene [6, 8-10]. These studies suggest some inherent ferromagnetic behaviour of graphite modified by ion beams. Additionally, it is promising to find a route alternative to Hummers' method to produce N-doped graphite [11]. Recent experimental results proved that N-doped graphite has a higher catalytic activity than pristine graphite, which can be used in proton-exchange membrane fuel cells [12, 13]. Therefore, structure and properties of highly oriented pyrolytic graphite (HOPG) samples were modified by N^+ and O^+ ion implantation and analyzed by the ion beam analysis techniques, X-ray absorption near edge structure method, and superconducting quantum interference device (SQUID), to probe magnetic response. Structural properties of graphite as well as the most common defects in graphitic materials were discussed in Chapter 3. The present chapter focuses on structural modifications in graphite related to the ion-beam modification process, while Chapter 7 summarizes resultant magnetic properties. We found that the origin of the ferromagnetic signal in these samples was dominated by transition metal impurities, distributed somewhat randomly in the depth of the graphite. Results of PIXE analysis for N- and O-doped graphite samples are presented here, as well.

6.2 Optimization of implantation parameters for low energy N and O implantation

Highly oriented pyrolytic graphite (HOPG) was implanted with N^+ and O^+ ions at the Tandetron facility, the University of Western Ontario. HOPG crystal was split into

~1mm thick layers. HOPG substrates were annealed in vacuum at 450°C before ion implantation to remove residual oxygen content. Implantation parameters were optimized to have O and N distributions in near-surface layers. Even at the lowest incident energy achievable at the Tandetron (25-50 keV), N and O implantation profiles would be relatively deep, and incident ion beam currents are too low, therefore implantation with N and O ions was performed through an Al mask (2.46 μm thick) in front of the HOPG piece. The incident energies for N and O beams were determined with SRIM. SRIM simulation takes ion beam straggling in the Al foil into account which slowed the incident ions, so they arrived at the graphite surface with a wide distribution in energy. Based on the simulated results, a 2.46 μm thick Al foil reduces the initial ion energies of 2.65 MeV N^+ and 2.78 MeV O^+ to energy distributions ranging from 0 to ~100keV for N^+ and O^+, and transmitting ~ 50% of the ions. SRIM simulation for 2.65 MeV N^+ irradiated HOPG presented in Figure 6.1 shows that the implanted ions and the produced vacancy defects were distributed in ~300 nm thick near-surface layer (with maxima at ~100 nm). Similar distribution of implanted ions and produced defects was predicted by SRIM for 2.78 MeV O^+ irradiated HOPG. Transmission coefficient of the Al foil was calibrated by the independent RBS measurement. Al contaminations on the HOPG surface from the Al mask recoils were $\leq 5\times10^{13}$ atoms/cm^2.

HOPG samples implanted with 2.65 MeV N^+ ions at doses of 2×10^{15} and 1×10^{16} ions/cm^2, and 2.78 MeV O^+ ions at doses of 2×10^{15}, 5×10^{15} and 1×10^{16} ions/cm^2 were prepared. These ion implanted doses were transmitted through the Al foil. The samples were denoted HOPG-N2e15, HOPG-N1e16, HOPG-O2e15, HOPG-O5e15 and HOPG-O1e16, respectively. After implantation, samples were annealed in vacuum on the implantation stage at 50°C and 100°C to partially heal the irradiation damage. The vacancy defect migration energy in graphene layer is ~1 eV, which results in significant migration already at 100-200°C [10, 14]. The higher temperature can cause irreversible change in modified graphite structure [6, 10].

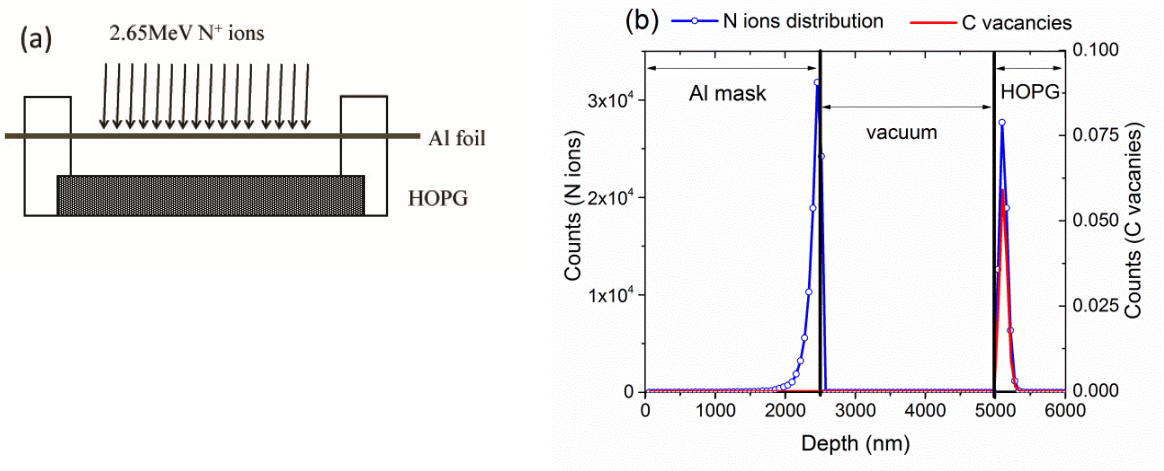

Figure 6.1. (a) Schematic of the implantation of 2.65 MeV N^+ in HOPG through Al mask; (b) SRIM simulation demonstrates distribution of N ions and C vacancies in HOPG.

6.2.1 RBS spectra

RBS spectra were recorded at the Tandetron facility using 4 MeV He^+ ion beams for HOPG samples implanted with N^+ and O^+ ions , 3.03 MeV He^+ ion beams for HOPG samples implanted with O^+ ions and 3.7 MeV He^+ for sample implanted with N^+, all 5^o off the normal to sample surface. 3.03 MeV and 3.7 MeV He^+ ions were chosen to take advantage of the non-Rutherford scattering cross sections to increase the sensitivity to surface oxygen and nitrogen, respectively. At these energies, the O cross section increase by a factor of 14-15, and N cross section increase by 5-7 times, while quantification uncertainty becomes worse [15].

RBS spectra of virgin HOPG and HOPG annealed at vacuum at 450°C collected with 3.03 MeV He^+ beams are presented in Figure 6.2. There was significant amount of oxygen in virgin HOPG crystal. It can be seen that, O content decreased by ~5 times in graphite annealed in vacuum (HOPG-450) but still can be detected by RBS. We note that a small amount of oxygen is always present at the surface due to exposure to the ambient environment.

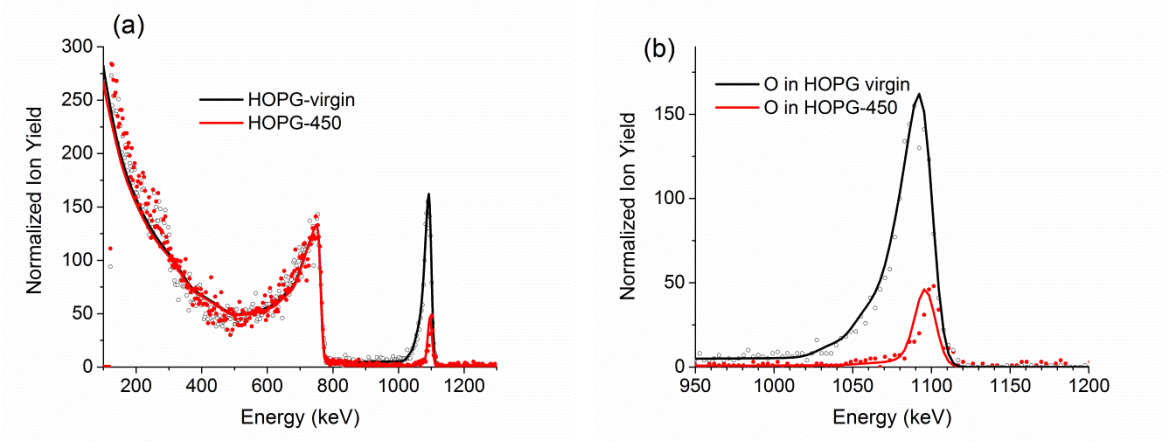

Figure 6.2. (a) RBS spectra for virgin HOPG and HOPG annealed in vacuum at 450°C collected with 3.03 MeV He+ beams; (b) Magnified oxygen peak.

RBS spectra detected with 3.03 MeV He^+ ion beams for O implanted HOPG samples showed an increase in O content after implantation compared to un-implanted HOPG-450 (Fig. 6.3). However the ion yield coming from the bulk of HOPG were low, and simulated spectra did not reveal unambiguously the difference between samples with different O implantation doses. Total O areal density is estimated to be 2.3×10^{16} atoms/cm^2 in HOPG-O1e16 sample, as compared to the pre-implantation value of 1.5×10^{16} atoms/cm^2 in HOPG-450.

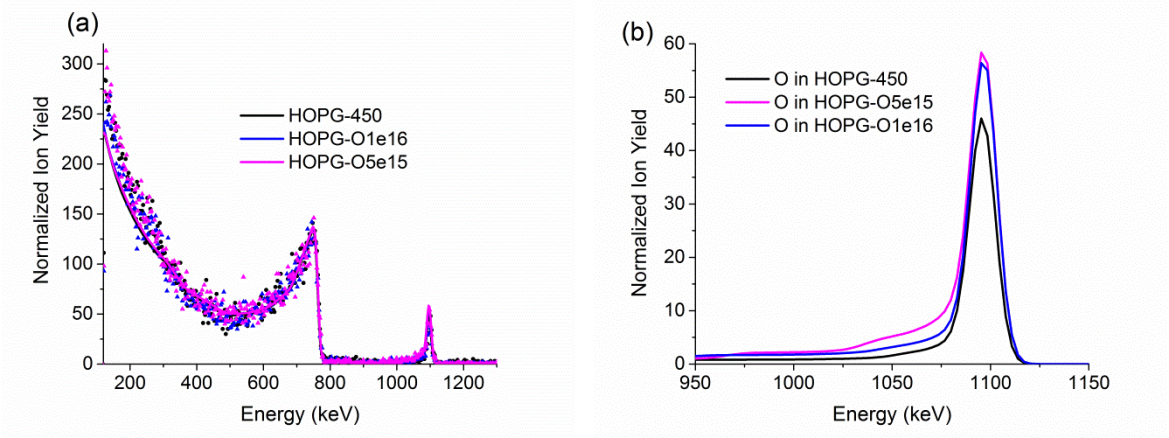

Figure 6.3. (a) RBS spectra recorded with He^+ beam at energy 3.03 MeV for HOPG-450, HOPG-O1e16 and HOPG-O5e15 samples; (b) Magnified oxygen peak.

For N implanted samples, RBS spectra were recorded with 3.7 MeV He^+ beams. Figure 6.4(a) shows the experimental RBS data for HOPG-N1e16 and the simulated by

SIMNRA program spectra for elements. Figure 6.4(b) presents N distribution in HOPG-N1e16 and HOPG-N2e15 samples. There were lower N content seen in HOPG-N2e15 comparing to HOPG-N1e16 sample (Fig. 6.4(b)). However low ion yield of N peaks as against C peak and overlapping with peaks from carbon isotopes (^{13}C, ^{14}C) made it ambiguous to determine real distribution of the implanted nitrogen, or at least N distribution deeper in the sample. Overall N areal densities were estimated to be 5×10^{15} atoms/cm^2 and 1.5×10^{16} for HOPG-N2e15 and HOPG-N1e16 samples, respectively.

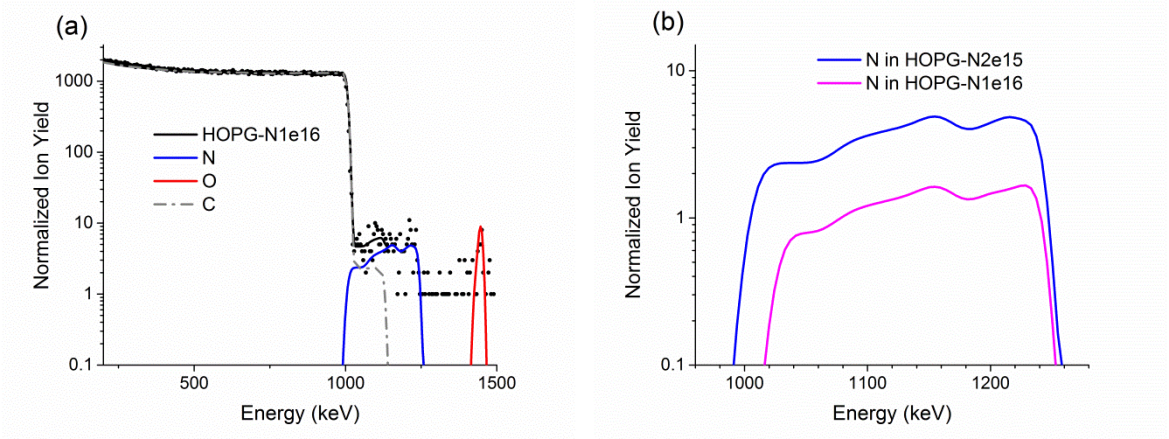

Figure 6.4. (a) RBS spectrum recorded He^+ beam at energy 3.7 MeV for N irradiated sample HOPG-N1e16; (b) Magnified peaks from N for HOPG-N1e16 and HOPG-N2e15 samples..

RBS analysis did not show any noticeable change of the O and N content in the implanted HOPG samples after annealing them in vacuum at 50°C and 100°C, though it has been shown that the higher temperature can cause irreversible change in graphite structure [6, 10].

6.2.2 PIXE spectra of HOPG samples

PIXE spectra of graphite samples were recorded at the Tandetron facility as was described in Chapter 4, chronologically after the SQUID measurements to be presented in Chapter 7 were completed. Though the PIXE method has limited sensitivity to light elements, it is suitable for trace element analysis in a carbon matrix. PIXE spectra recorded with 1 MeV and 2 MeV H^+ particles for selected HOPG samples are presented in Figures 6.5 and 6.6, respectively. Higher H^+ energy provided higher intensity of X-ray

characteristic peak but in the same time it resulted in higher background level. The spectra revealed the presence of metallic impurities, such as Al, Ca, Ti, Cr, Fe, Ni and Cu, in different concentrations in all the analyzed graphite samples. This information has some bearing on the magnetism analysis. The amounts of transition metals, including Cr, Ti, Fe and Ni, are changing randomly from one sample to another; there is no correlation with implantation dose. However we often see dependence between the amount of magnetic impurities and the observed magnetic response, as will be discussed in the next chapter.

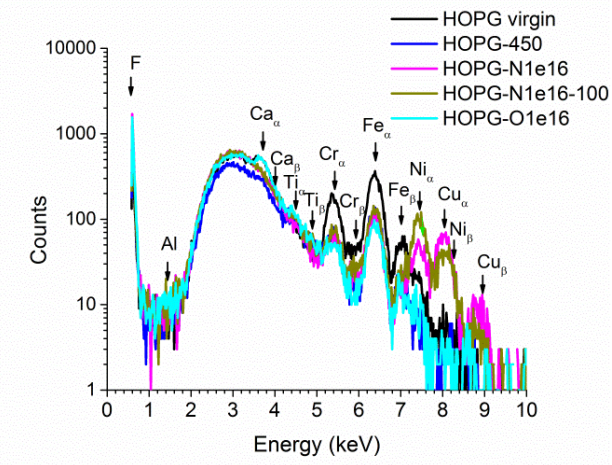

Figure 6.5. PIXE spectra of selected HOPG samples recorded with 2 MeV H^+ ions.

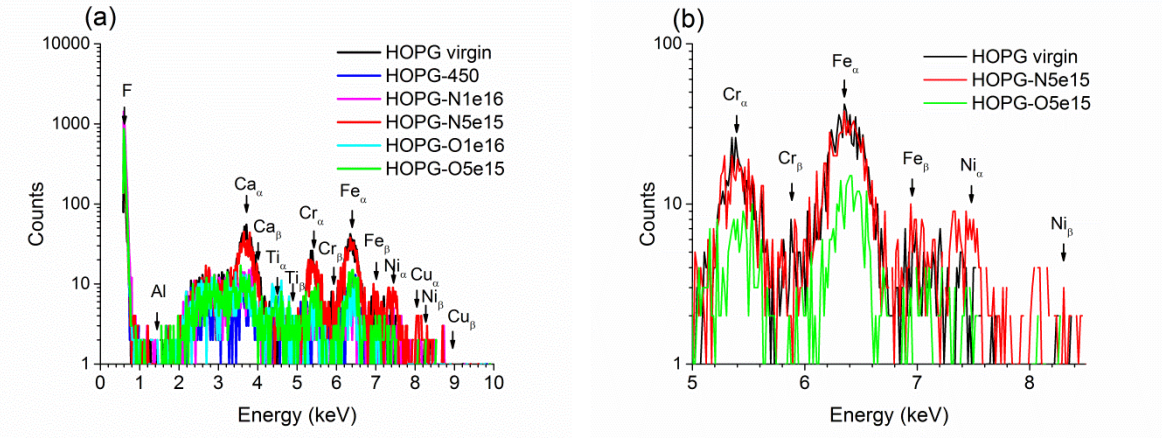

Figure 6.6. (a) PIXE spectra of selected HOPG samples recorded with 1 MeV H^+ ions; (b) Enlarged image of Cr, Fe and Ni peaks for HOPG, HOPG-N5e15 and HOPG-O5e15 samples.

Metallic particles are known impurities in HOPG crystals used for monochromators [16, 17]. Fe was the most prevalent impurity in all our HOPG samples. PIXE spectra of selected HOPG samples recorded with 1 MeV H^+ ions were used to calculate the atomic density of Fe in different graphite samples (with the standard sample 58 mg/cm^2 Fe in Al with known composition and the use of equation (2.13) as was described above in Chapter 4. Results are presented in Table 6.1. The concentration of Fe differed from sample to sample which was caused by non-uniform distribution of impurities in the original HOPG crystal. A similar result was reported recently by Venkatesan *et al*. [17] who found different concentrations of metallic clusters in HOPG crystals as the crystal was cleaved in the depth.

Table 6.1. Values of the atomic densities of Fe in the standard sample 58 mg/cm^2 Fe in Al and HOPG samples.

Sample	Element	Channels (keV)	Integrated Area A	Atomic Density (10^{14} atoms/cm^2)
58 mg/cm^2 Fe in Al standard sample	Fe	6.18-6.70	30335	6300±300
HOPG virgin	Fe	6.18-6.70	692	42±2
HOPG-450	Fe	6.18-6.70	159	9.0±0.5
HOPG-N1e16	Fe	6.18-6.70	142	8.3±0.4
HOPG-N1e16-100	Fe	6.18-6.70	181	11.0±0.5
HOPG-N5e15	Fe	6.18-6.70	652	37±2
HOPG-O1e16	Fe	6.18-6.70	140	8.0±0.4
HOPG-O1e16-100	Fe	6.18-6.70	111	6.3±0.3
HOPG-O5e15	Fe	6.18-6.70	232	13.0±0.6

6.3 X-ray absorption near edge structure

C K-edge and O K-edge XANES spectra were measured at the Canadian Light Source (CLS) (Saskatoon, Canada) at the high resolution Spherical Grating Monochromator (SGM) beamline. The spectra were collected in total electron yield (TEY) and total fluorescence yield (TFY). X-ray photon energy was calibrated at the C K-edge. All spectra were normalized to the intensity of the incident beam I_0, and a continuous background was subtracted from data in same manner as for XANES measurements of strontium titanate samples.

6.3.1 Carbon K-edge XANES of HOPG samples

C K-edge XANES spectra of un-implanted HOPG (virgin and annealed at 450°C) are shown in Figure 6.7. All C K-edge XANES spectra were normalized by energy by the position of the π^* peak and by intensity to unity at energy above the absorption edge (at 320 eV).

C K-edge TEY spectra of all HOPG samples before implantation had a sharp peak at 285.5 eV assigned to C $1s \rightarrow \pi^*$ transitions due to excitations of $C=C$ bonds (sp^2). Two peaks at 291.15 eV and 292.8 eV are attributed to excitation C 1s states to unoccupied σ^* orbitals of tetrahedral $C-C$ (sp^3). Since these peaks are due to excitonic resonances, they are very narrow owing to a long lifetime of bound excitons. Double σ^* peaks are observed because they result from partial overlapping of p_{xy} and p_z orbitals along the c-axis of structurally non-equivalent C atoms which belong to A or B sites in graphite crystal. The σ^* peaks are sensitive to long range order, and are observed in highly crystalline graphite samples with good alignment between the graphene planes [8, 18-21].

The relative intensity of the π^* vs. σ^* peaks depends on the orientation of the graphitic plane with respect to the direction of the incident X-ray beam which is linearly polarized in the plane of the electron orbit of the synchrotron. The σ^* peak dominates at normal incidence, and the π^* peak is more prominent at grazing incidence [12, 22]. The relative intensity of π^* *vs.* σ^* depends on the alignment between basal plane of

graphite. The π^* peak decreases in samples with low crystallinity [12, 23]. Thus, C K-edge XANES can be used to probe the crystallinity of graphite.

Three absorption features, A, B and C, were observed in the area above σ^* peaks. In the spectra of HOPG-450, peaks A, B, and C were at 297.5 eV, 303.5 eV, and 307.3 eV, respectively. For virgin HOPG, peaks A and B were observed at same energies but feature C was detected at lower energy (306.4 eV).

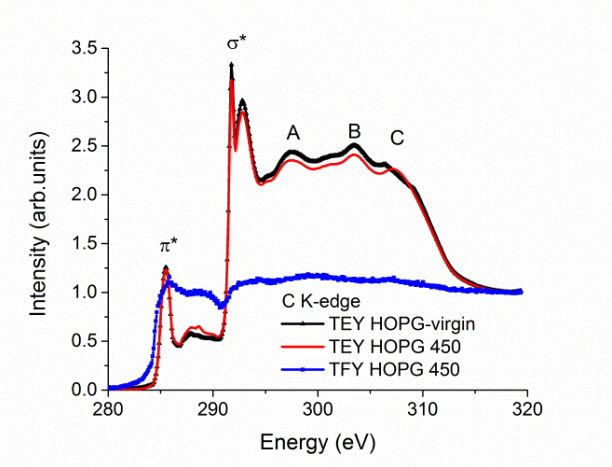

Figure 6.7. C K-edge TEY spectra of un-implanted graphite samples: virgin HOPG and annealed at 450°C; C K-edge TFY spectrum of HOPG annealed at 450°C is also shown. The flattened out spectral feature in TFY results from saturation (sample is optically thick).

After implantation with N and O ions, the intensity of π^* and σ^* peaks decreases dramatically, and the absorption features A, B and C became smooth as the implantation doses increased (Figs. 6.8 (a) and (b)). Some spectral features in this area can be seen only in C K-edge XANES of HOPG-N2e15 (the samples with the lowest implantaton dose) (Fig. 6.8 (a)).

In the intermediate region between π^* and σ^* resonances, three features D_1, D_2 and D_3 appeared in spectra of ion irradiated HOPG samples (Fig. 6.8(c)). Note that there is no significant difference between samples implanted with N and samples implanted with O. Most intensive peak D_2 was observed at ~289.0 eV HOPG-N5e15, HOPG-N1e16, HOPG-O5e15 and HOPG-O1e16. The D_2 peak was noticeably lower in sample with the lowest implantation dose, HOPG-N2e15, than in HOPG samples implanted with higher doses and shifted to lower energy. D_1 and D_3 peaks were observed at ~286.9 eV

and ~290.3 eV, respectively, in the C K-edge spectra of HOPG-N5e156, HOPG-N1e16, HOPG-O5e15 and HOPG-O1e16.

(a) (b)

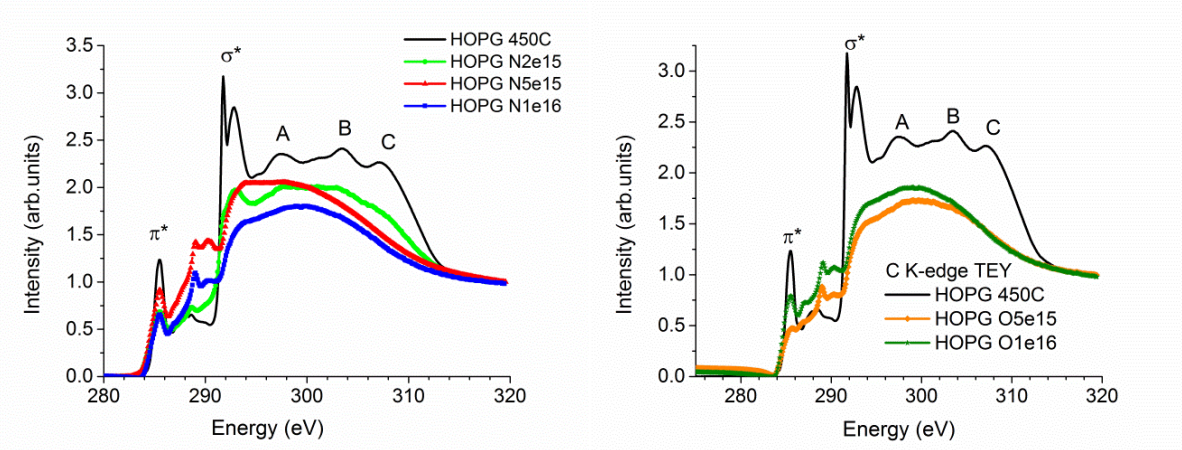

(c)

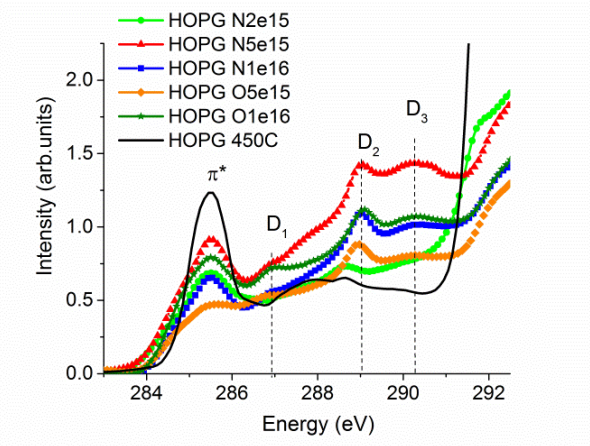

Figure 6.8. C K-edge TEY XANES spectra of HOPG samples implanted with different doses of (a) N and (b) O; (c) Enlarged graph demonstrates adsorption features in the intermediate region between C π^* and σ^* resonances. Spectrum of un-implanted HOPG is shown for comparison.

The appearance of C K-edge TFY spectra of HOPG samples varies distinctly from TEY spectra (Figs. 6.7 and 6.9(a)). TFY spectra of HOPG samples before and after implantation showed dramatic decrease of σ^* peak intensity. The HOPG samples are not single crystals but agglomerates of small graphite crystals oriented in one direction. TFY spectra are bulk sensitive and probe much thicker layer comparing to TEY mode. The difference between TEY and TFY can reflect the fact that the latter is averaged over a big

number of individual crystallines with some degree of misalignment between them. Unfortunately, the TFY features are somewhat obscured due to the thickness saturation effect, which hampers more detailed interpretation.

Figure 6.9 (a) demonstrates C K-edge TEY and TFY spectra of HOPG-N1e16 as an example. TFY spectra of all implanted HOPG samples had a shoulder at ~284.6 eV, peaks at ~286.0 eV and ~290.1 eV, and a gradual rise at energy above ~292 eV. Small pre-edge peak at ~282.3 eV appeared in the spectra of implanted samples (Fig. 6.9(b)). The pre-edge feature has been observed in HOPG after ion irradiation and attributed to defect induced states just above the Fermi level [6, 12, 24].

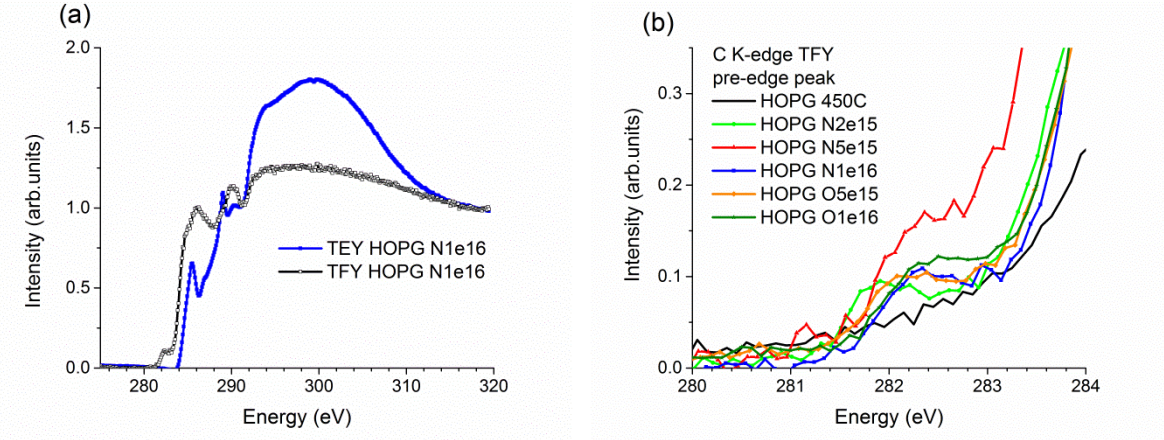

Figure 6.9. (a) C K-edge XANES spectra of HOPG-N1e16 collected in total electron yield and total fluorescent yield. (b) Enlarged pre-edge peak in TFY spectra of HOPG samples implanted with different doses of N and O.

Annealing in vacuum at 50°C and 100°C did not change the appearance of C K-edge spectra. All absorption peaks were observed at the same positions, though the intensity of $D_{1\text{-}3}$ peaks changed slightly with annealing temperature, as can be seen in C K-edge TEY spectra of HOPG-N1e16 and HOPG-O1e16 (Fig. 6.10 (a) and (b)). However there was not any definite pattern in these changes, which probably reflected minor variations between samples. Notably, spectral features of O- and N-implanted samples are identical. In order to see if there is any difference between the two types, we looked closely at the O and N K-edge.

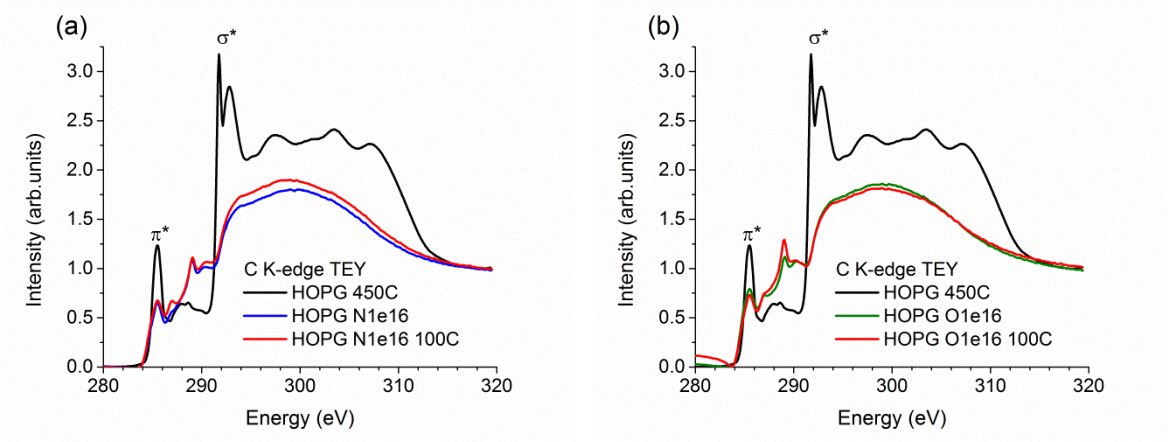

Figure 6.10. C K-edge XANES spectra of (a) HOPG-N1e16 and (b) HOPG-O1e16 samples, implanted and annealed in vacuum at 50°C and 100°C.

6.3.2 O K-edge XANES of HOPG samples

O K-edge spectra were normalized to unity by the intensity of the highest peak at 540eV. Figure 6.11 shows O K-edge XANES of virgin HOPG and annealed at 450°C HOPG-450 samples. O K-edge XANES in TEY and TFY modes have a sharp peak at ~531 eV and a broader peak at ~539.2 eV. Typically, the peak at ~531 eV has been assigned to O 1s $\rightarrow \pi^*$ excitation of COOH or C=O groups, whereas a broad peak at ~539 eV has been attributed to the σ^* excitation of various C–O function groups [25-28].

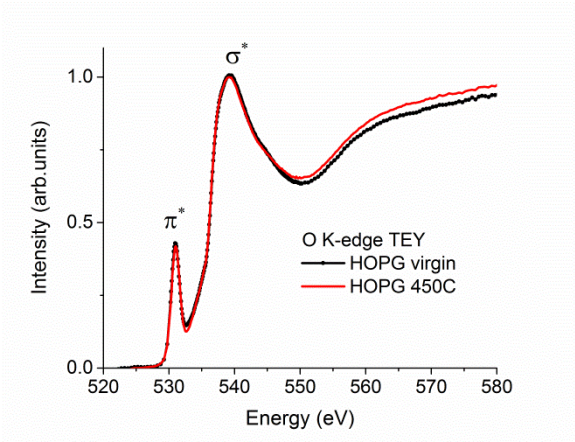

Figure 6.11 O K-edge XANES of un-implanted samples: virgin HOPG and annealed HOPG 450 collected in total electron yield.

O K-edge XANES spectra collected in TEY mode of HOPG implanted with N and O are presented in Figure 6.12(a). π^* and σ^* peaks both shifted to higher energies. Samples HOPG-N5e15, HOPG-N1e16 and HOPG-O5e15 had π^* and σ* peaks at ~532.75 eV, and ~540.75 eV, respectively. σ^* peak in HOPG-O1e16 spectrum shifted to ~541.1 eV. An additional peak at ~536.0 eV that appeared in the intermediate area between π* and σ^* peaks can be assigned to O 1s transitions to σ^* O–H moieties [26]. A shoulder at ~531.5 eV observed in the implanted HOPG samples. The assignment of the shoulder differs in literature from π^* states of $C=O$ to the π∗ state of $C-O$ from the epoxide [29, 30].

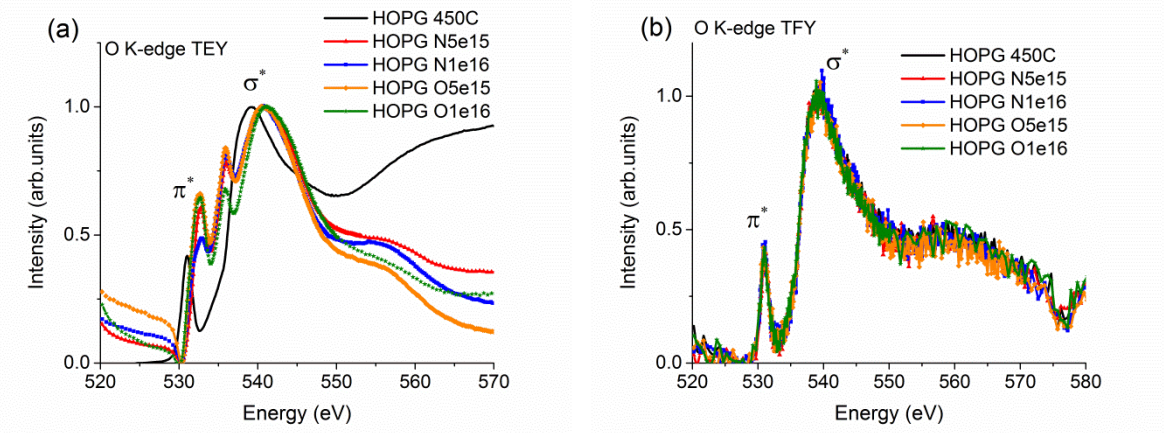

Figure 6.12 O K-edge XANES of HOPG samples implanted with N and O at different doses: collected in (a) total electron yield and (b) inverted fluorescence yield.

Annealing in vacuum at 100°C did not affect significantly the surface condition of the implanted HOPG samples. The position of the absorption peaks in O K-edge TEY XANES spectra of HOPG-N1e16 and HOPG-O1e16 did not change with annealing as can be seen in Figures 6.13 and 6.14. O K-edge TFY XANES spectra were identical for all graphite samples (Figs. 6.12-14) which proves that ion implantation affected only the near-surface area of the HOPG crystals.

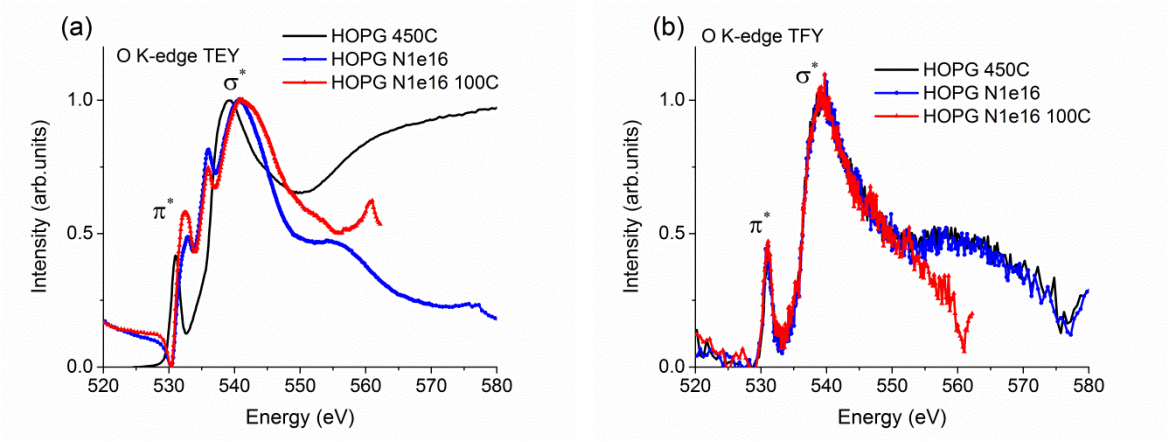

Figure 6.13 O K-edge XANES of un-implanted HOPG, HOPG-N1e16 and HOPG-N1e16-100C samples collected in (a) total electron yield and (b) inverted fluorescence yield.

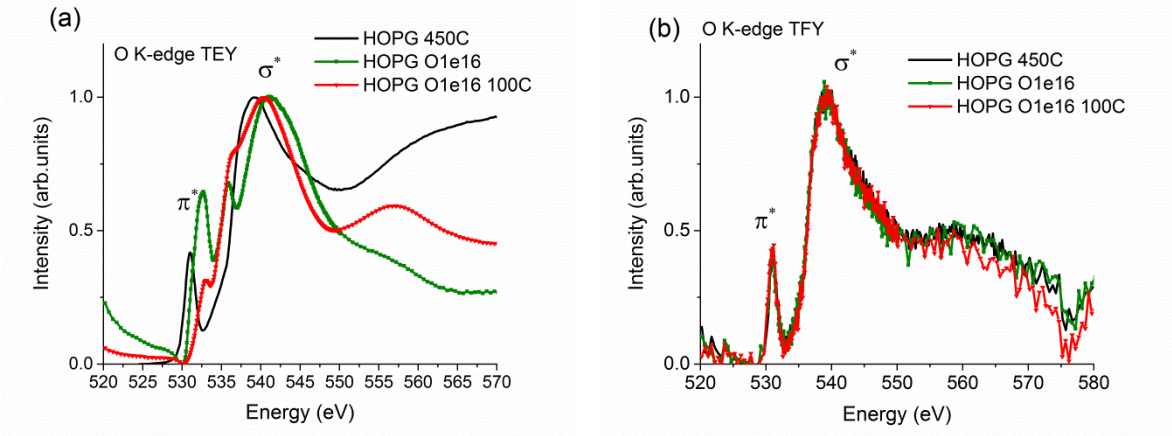

Figure 6.14. O K-edge XANES of un-implanted HOPG, HOPG-O1e16 and HOPG-O1e16-100C samples collected in (a) total electron yield and (b) inverted fluorescence yield.

6.3.3 XANES at N K-edge

N K-edge XANES spectra are shown in Figure 6.15 There are two weak inverted peaks at ~ 399.3 eV and ~ 400.6 eV in spectra of HOPG-N1e16 samples (Fig.6.15). Same spectra were observed for HOPG-N2e15 samples. The absorption features at N K-edge were very weak because of low concentration of N in graphite matrix and did not reveal any interesting information. In the soft X-ray energy range, photon energy is completely absorbed by material, and the elements of HOPG samples are competing for it. At N K edge (~400eV), the attenuation length (which is the thickness of the material at which the intensity of the transmitted X-rays reduces in *e* times) in C is at least 10^3 times

shorter than in N. Due to the difference in the attenuation length in carbon and nitrogen (Fig. 6.16), in N-doped graphite samples soft X-rays were absorbed mostly by carbon. As a result at low level of N doping, it is difficult to register absorption at the N K-edge. As a result N K-edge spectra on N irradiated HOPG did not reveal any interesting information.

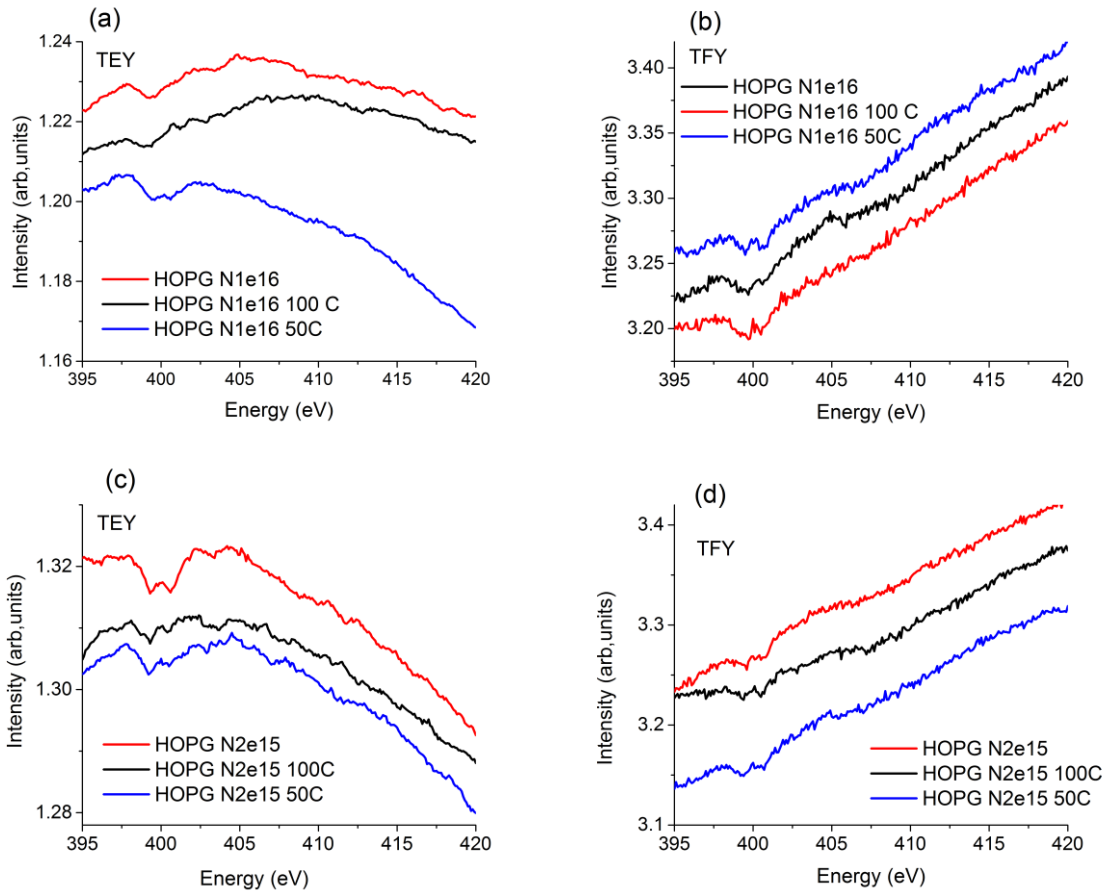

Figure 6.15 N K-edge XANES spectra of N-doped HOPG samples at doses of 2×10^{15} and 1×10^{16} ions/cm^2.

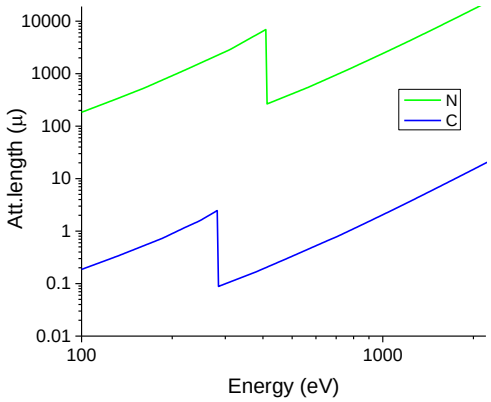

Figure 6.16 Attenuation length of soft X-rays absorbed by C and N [31].

6.4 Discussion

Implantation of HOPG samples with N and O ions led to formation of defects in the near surface area of graphite samples. RBS spectra clearly showed the increase of N and O content followed implantation. Low temperature annealing in vacuum at 50°C and 100°C did not lead to obvious redistribution of implanted ions. However low scattering cross sections for light elements and overlapping of O, N, C and its isotopes peaks gave higher uncertainty with quantitative conclusions of RBS analysis.

The presence of metallic impurities (mostly Fe) was detected by the PIXE method. Metallic pellets (up to 5μm in diameter) are possible contaminations in HOPG crystals of ZY-grades used for monochromators [16, 17]. However, Fe was found by neither XANES nor RBS analysis. The lack of Fe and other transition metal peaks in RBS spectrum indicated that these impurities are distributed uniformly in depths up to microns. There are no segregation effects on the surface. Defects produced by ion irradiation increased the surface reactivity. As followed from the XANES analysis, the resonances corresponding to different carbon and oxygen functional groups appeared in C K-edge spectra of the ion irradiated HOPG samples in the energy region between π^* and σ^* resonances of pure graphite. The intensity of the resonances depended slightly on the implantation doses, i.e. on the degree of irradiation damage. There was no noticeable difference between HOPG implanted with N and HOPG implanted with O. It proved the defect origin of the observed changes. It is likely that defects produced by the ion

implantation process react with various oxidizing moieties in ambient atmosphere. Only the sample with lowest implantation dose HOPG-N2e15 stood out. Apparently the irradiation damage was insignificant in this samples compared to the other HOPG samples implanted with higher doses of N and O ions.

Additional features in the intermediate region between π^* and σ^* resonances are due to defects, different functional groups ($C-OH$, $C-C$, $COOH$ or $C=O$) and/or surface contamination [25, 29, 32, 33]. Studies have shown that there is a weak dependence on the orientation of the incident beam indicating that these electronic states have an isotropic character [18, 22, 29]. In purely crystalline graphite the area between π^* and σ^* resonances is usually monotonic. Table 6.2 presents a possible assignment of spectral features observed in C K-edge XANES of N and O implanted HOPG samples.

Table 6.2 Assignments of peaks observed in C K-edge XANES spectra of HOPG samples

Peak	Assignment	Ref.
pre-edge ~282.3 eV	surface defects, dangling bonds in amorphous carbon	[6, 12]
D_1 286.9 eV	π^* *C-O* of hydroxyl group π^* *C-OH* of phenol	[26, 29, 30, 34]
D_2 289.0 eV	π^* *C=O* of acrylic group *COOH* and *C-H* species σ^* *C-O* of epoxide group	[25, 26, 29, 30, 34]
D_3 290.3 eV	π^* *C=O* carboxylic group π^* *C=O* carbonyl group diamond-like bonds in amorphous carbon (due to mix of sp^2 and sp^3 bonds)	[26, 29, 34, 35]

Studies of graphene and graphene oxide assign the peak at ~287 eV to π^* states of $C-O$ bonds derived from hydroxyl groups [26, 29, 33, 34]. The feature was also ascribed to the contribution from $C-H$ σ^* band and from $O-C=O$ band [27]. Feature at ~288 eV is assigned to $C-O$ σ^* of epoxides [6, 26, 29, 33]. Peaks in the

region 288.8—290.3 eV are attributed to $C=O$ π^* band of carboxylic acid and carbonyl moieties [4, 26, 29, 34]. The feature at ~289 eV was also observed in amorphous carbon due to diamond-like bond with a mixture of sp^2 and sp^3 [36, 37].

O K-edge XANES also demonstrated effect of ion irradiation of HOPG. In ion implanted HOPG samples additional peaks which could be ascribed to $C=O$, $C-O$ and $O-H$ moieties were detected in O K-edge TEY spectra.

Low temperature annealing in vacuum at 50 and 100°C did not lead to change in surface condition of HOPG implanted with N and O ions. Spectra of implanted and annealed HOPG samples showed adsorption peaks in the same positions (see for example, Figs. 5.8 and 5.12). Comparison between TFY spectra at O K-edge showed that in the bulk all HOPG samples had practically same structure before and after implantation. However TFY spectra at C K-edge revealed defect states appeared after implantation. Additional pre-edge peak at ~282.3 eV due to defects appeared in the spectra of implanted samples (Fig. 5.8(b)).

In summary, HOPG samples were implanted with N and O ions to modify the near-surface area of HOPG samples. The produced irradiation damage was confined to the near-surface layers of HOPG (of ~300 nm in thickness) for both ions. Comparison of TEY and TFY XANES spectra at C K-edge and O K-edge showed that the effect of ion irradiation was mostly restricted to the HOPG surface, e.g. the first ~5nm. Defects (vacancies) produced by ion irradiation increased the surface reactivity. Exposed to the ambient atmosphere, defective graphite surface reacted with the gas molecules giving rise to the formation of new oxygen functional groupson the HOPG surface. The effect showed dependence on the implantation dose but there was not significant difference noticed between O and N irradiated HOPG samples.

References

[1] X.Y. Sun, R. Wang, D.S. Su, Research progress in metal-free carbon-based catalysts, Chin. J. Catal. 34 (2013) 508-523.
[2] D. Chen, A. Holmen, Z.J. Sui, X.G. Zhou, Carbon mediated catalysis: A review on oxidative dehydrogenation, Chin. J. Catal. 35 (2014) 824-841.
[3] J.L. Figueiredo, M.F.R. Pereira, The role of surface chemistry in catalysis with carbons, Catal. Today 150 (2010) 2-7.
[4] R.A. Sidik, A.B. Anderson, N.P. Subramanian, S.P. Kumaraguru, B.N. Popov, O_2 reduction on graphite and nitrogen-doped graphite: Experiment and theory, J. Phys. Chem. B 110 (2006) 1787-1793.
[5] O. Lehtinen, J. Kotakoski, A.V. Krasheninnikov, A. Tolvanen, K. Nordlund, J. Keinonen, Effects of ion bombardment on a two-dimensional target: Atomistic simulations of graphene irradiation, Phys Rev B 81 (2010) 153401.
[6] Z. He, X. Yang, H. Xia, T.Z. Regier, D.K. Chevrier, X. Zhou, T.K. Sham, Role of defect electronic states in the ferromagnetism in graphite, Phys Rev B 85 (2012) 144406.
[7] X.M. Yang, Z.T. He, W.F. Li, H.H. Xia, Y. Song, X.T. Zhou, X.D. Liu, M.W. Zhao, T.W. Wang, K.Y. Hou, Localized defects closely related with the magnetism of graphite induced by $^{12}C^{+}$ ion implantation, J Appl Phys 109 (2011) 083933.
[8] R.A. Rosenberg, P.J. Love, V. Rehn, Polarozation-dependent C(K) near -edge X-ray absoprtion fine structure of graphite Physical Review B 33 (1986) 4034-4037.
[9] M.A. Ramos, J. Barzola-Quiquia, P. Esquinazi, A. Munoz-Martin, A. Climent-Font, M. Garcia-Hernandez, Magnetic properties of graphite irradiated with MeV ions, Phys Rev B 81 (2010) 214404.
[10] F. Banhart, J. Kotakoski, A.V. Krasheninnikov, Structural Defects in Graphene, Acs Nano 5 (2011) 26-41.
[11] R.P. Rocha, A.G. Gonçalves, L.M. Pastrana-Martínez, B.C. Bordoni, O.S.G.P. Soares, J.J.M. Órfão, J.L. Faria, J.L. Figueiredo, A.M.T. Silva, M.F.R. Pereira, Nitrogen-doped graphene-based materials for advanced oxidation processes Catalysis Today 249 (2015) 192-198.
[12] D.S. Geng, S.L. Yang, Y. Zhang, J.L. Yang, J. Liu, R.Y. Li, T.K. Sham, X.L. Sun, S.Y. Ye, S. Knights, Nitrogen doping effects on the structure of graphene, Applied Surface Science 257 (2011) 9193-9198.
[13] Y.G. Chen, J.J. Wang, H. Liu, M.N. Banis, R.Y. Li, X.L. Sun, T.K. Sham, S.Y. Ye, S. Knights, Nitrogen Doping Effects on Carbon Nanotubes and the Origin of the Enhanced Electrocatalytic Activity of Supported Pt for Proton-Exchange Membrane Fuel Cells, J. Phys. Chem. C 115 (2011) 3769-3776.
[14] A.V. Krasheninnikov, P.O. Lehtinen, A.S. Foster, R.M. Nieminen, Bending the rules: Contrasting vacancy energetics and migration in graphite and carbon nanotubes, Chemical Physics Letters 418 (2006) 132-136.
[15] J.F. Ziegler, Helium : stopping powers and ranges in all elemental matter, Pergamon, New York, NY, 1977.
[16] M. Sepioni, R.R. Nair, I.L. Tsai, A.K. Geim, I.V. Grigorieva, Revealing common artifacts due to ferromagnetic inclusions in highly oriented pyrolytic graphite, Epl 97 (2012) 47001.

[17] M. Venkatesan, P. Dunne, Y.H. Chen, H.Z. Zhang, J.M.D. Coey, Structural and magnetic properties of iron in graphite, Carbon 56 (2013) 279-287.
[18] R. Ahuja, P.A. Bruhwiler, J.M. Wills, B. Johansson, N. Martensson, O. Eriksson, Theoretical and experimental study of the graphite 1s x-ray absorption edges, Phys Rev B 54 (1996) 14396-14404.
[19] P.A. Bruhwiler, A.J. Maxwell, C. Puglia, A. Nilsson, S. Anderson, N. Martensson, π^* and σ^* excitons in C-1s absorption of graphite, Physical Review Letters 74 (1995) 614-617.
[20] T.K. Sham, Nanoparticles and nanowires: synchrotron spectroscopy studies, International Journal of Nanotechnology 5 (2008) 1194-1246.
[21] D.G. McCulloch, R. Brydson, Carbon K-shell near-edge structure calculations for graphite using the multiple-scattering approach, Journal of Physics-Condensed Matter 8 (1996) 3835-3841.
[22] V.V. Belavin, A.V. Okotrub, L.G. Bulusheva, A.S. Kotosonov, D.V. Vyalykh, S.L. Molodtsov, Determining misorientation of graphite grains from the angular dependence of X-ray emission spectra, J. Exp. Theor. Phys. 103 (2006) 604-610.
[23] J. Zhong, T. Xie, J.J. Deng, X.H. Sun, X.L. Pan, X.H. Bao, Z.Y. Wu, Direct observation and spectroscopy of nanoscaled carboxylated carbonaceous fragments coated on carbon nanotubes, Chem. Commun. 47 (2011) 8373-8375.
[24] D. Pacile, M. Papagno, A.F. Rodriguez, M. Grioni, L. Papagno, Near-edge x-ray absorption fine-structure investigation of graphene, Physical Review Letters 101 (2008) 066806.
[25] A. Kuznetsova, I. Popova, J.T. Yates, M.J. Bronikowski, C.B. Huffman, J. Liu, R.E. Smalley, H.H. Hwu, J.G.G. Chen, Oxygen-containing functional groups on single-wall carbon nanotubes: NEXAFS and vibrational spectroscopic studies, Journal of the American Chemical Society 123 (2001) 10699-10704.
[26] B.J. Schultz, R.V. Dennis, J.P. Aldinger, C. Jaye, X. Wang, D.A. Fischer, A.N. Cartwright, S. Banerjee, X-ray absorption spectroscopy studies of electronic structure recovery and nitrogen local structure upon thermal reduction of graphene oxide in an ammonia environment, RSC Adv. 4 (2014) 634-644.
[27] S.C. Ray, H.M. Tsai, J.W. Chiou, B. Bose, J.C. Jan, K. Kumar, W.F. Pong, D. Dasgupta, M.H. Tsai, X-ray absorption spectroscopy (XAS) study of dip deposited a-C : H(OH) thin films, Journal of Physics-Condensed Matter 16 (2004) 5713-5719.
[28] V. Lee, L. Whittaker, C. Jaye, K.M. Baroudi, D.A. Fischer, S. Banerjee, Large-Area Chemically Modified Graphene Films: Electrophoretic Deposition and Characterization by Soft X-ray Absorption Spectroscopy, Chem. Mat. 21 (2009) 3905-3916.
[29] V. Lee, R.V. Dennis, B.J. Schultz, C. Jaye, D.A. Fischer, S. Banerjee, Soft X-ray Absorption Spectroscopy Studies of the Electronic Structure Recovery of Graphene Oxide upon Chemical Defunctionalization, J. Phys. Chem. C 116 (2012) 20591-20599.
[30] H.K. Jeong, H.J. Noh, J.Y. Kim, M.H. Jin, C.Y. Park, Y.H. Lee, X-ray absorption spectroscopy of graphite oxide, EPL 82 (2008) 67004.
[31] B.L. Henke, E.M. Gullikson, J.C. Davis, X-Ray Interactions: Photoabsorption, Scattering, Transmission, and Reflection at E = 50-30,000 eV, Z = 1-92, Atomic Data and Nuclear Data Tables 54 (1993) 181-342.
[32] J.A. Brandes, G.D. Cody, D. Rumble, P. Haberstroh, S. Wirick, Y. Gelinas, Carbon K-edge XANES spectromicroscopy of natural graphite, Carbon 46 (2008) 1424-1434.

[33] V. Lee, R.V. Dennis, C. Jaye, X. Wang, D.A. Fischer, A.N. Cartwright, S. Banerjee, In situ near-edge x-ray absorption fine structure spectroscopy investigation of the thermal defunctionalization of graphene oxide, J. Vac. Sci. Technol. B 30 (2012) 061206.
[34] R.V. Dennis, B.J. Schultz, C. Jaye, X. Wang, D.A. Fischer, A.N. Cartwright, S. Banerjee, Near-edge x-ray absorption fine structure spectroscopy study of nitrogen incorporation in chemically reduced graphene oxide, J. Vac. Sci. Technol. B 31 (2013) 041204.
[35] R. Gago, I. Jimenez, J.M. Albella, A. Climent-Font, D. Caceres, I. Vergara, J.C. Banks, B.L. Doyle, L.J. Terminello, Bonding and hardness in nonhydrogenated carbon films with moderate sp^3 content, J Appl Phys 87 (2000) 8174-8180.
[36] R. Gago, I. Jimenez, J.M. Albella, A. Climent-Font, D. Caceres, I. Vergara, J.C. Banks, B.L. Doyle, L.J. Terminello, Bonding and hardness in nonhydrogenated carbon films with moderate sp(3) content, Journal of Applied Physics 87 (2000) 8174-8180.
[37] I. Jimenez, R. Gago, J.M. Albella, Fine structure at the X-ray absorption π^* and σ^* bands of amorphous carbon, Diam. Relat. Mat. 12 (2003) 110-115.

Chapter 7. Defect induced magnetism

7.1 New materials for spintronics

The emerging technology of spintronics is looking for ways to utilize an electron charge, and an electron spin as conventional information carriers in electronic devices. Such devices promise to increase integration densities, speed up data processing, and decrease power consumption compared to the conventional semiconductor electronics. Materials suitable for spintronic applications besides being ferromagnetic must be compatible with conventional materials used in electronics, and be functional at room temperature. Doping of oxides and semiconductors with transition metals (TM) is one of the promising methods to create new spintronic materials. Dietl *et al.* [1] in their theoretical work showed several promising scenarios for tailoring magnetic and spin-related phenomena in semiconductors. These theoretical calculations explain ferromagnetic ordering with the focus on Mn-doped semiconductors. The result of the calculations demonstrated that at least two p-type semiconducting materials, GaN and ZnO, containing 5% of Mn doping and 3.5×10^{20} holes per cm^3, can have Curie temperatures above 300 K. A high Curie point, T_C, is the main condition to makes these materials suitable for spintronic applications (Fig. 7.1).

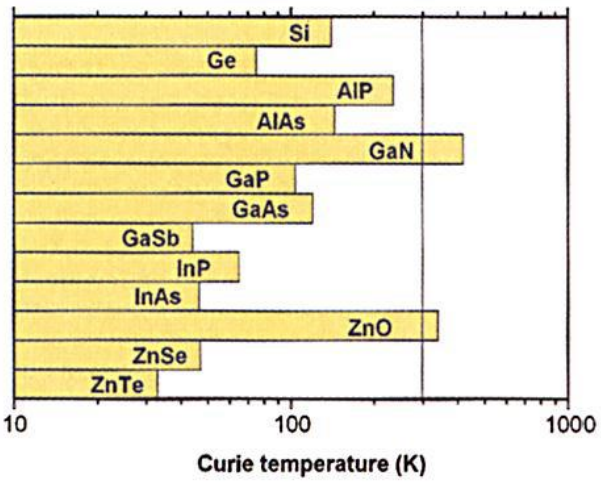

Figure 7.1. Values of Curie temperature calculated for various oxide materials containing 5% of Mn doping and 3.5×10^{20} holes per cm^3. Adapted from Ref. [1].

Studies of weak magnetism of oxide and carbon materials have shown that they can demonstrate magnetic properties even in the absence of TM doping. The magnetism has been induced by defects. The phenomenon has been called d^0-magnetism [2].

This chapter gives a brief introduction to the magnetic properties of materials, and explains the basic ideas of d^0-magnetism. The experimental results of magnetic properties measurement of $SrTiO_3$ and highly ordered pyrolytic graphite modified by ion beams are then presented. The details of structural analysis of these materials were discussed in detail in previous chapters 4, 5 and 6.

7.2 Types of magnetism

Magnetism of materials is connected to the intrinsic property of electrons – to the angular momentum or the spin which can accept two states, pointing up or down. Only electrons with opposite spins can occupy the same electron level in an element. In elements with a filled electronic shell such arrangement results in zero net orbital motion. However in elements with a partially filled electronic shell, electrons can accept (spontaneously or due to an applied external magnetic field) a configuration where the electrons are aligned in the same direction creating a macroscopic magnetic moment (Fig. 7.2). Spontaneous alignment happens only in ferromagnetic elements. Among all the elements of the periodic table only a few are truly ferromagnetic: 3d transition metals Fe, Co and Ni (at room temperature), and 4f rare-earth Gd (just below room temperature). Their alloys and compounds form a wide family of magnetic materials. One of the few naturally occurring ferromagnetic oxides is magnetite Fe_3O_4.

All materials can be divided into paramagnetic, diamagnetic, ferromagnetic and antiferromagnetic depending on their response to an applied external magnetic field. The magnetization, M, in para- and diamagnetic materials depends linearly on the applied magnetic field, H:

$$M = \chi H, \qquad (7.1)$$

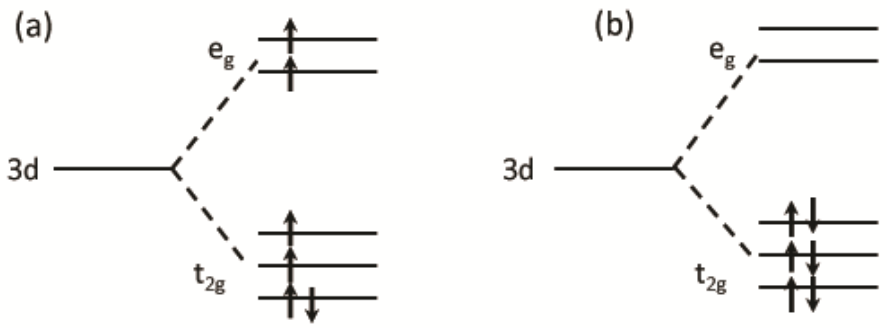

Figure 7.2. 3d electron level of Fe^0 ([Ar] $3d^6 4s^2$): (a) "high" spin configuration, (b) "low" spin configuration.

For a diamagnetic material, the magnetic susceptibility χ is negative and independent of temperature; for a paramagnetic material, χ is positive and decreases as 1/T with temperature.

In a ferromagnetic material there is a non-linear dependence on an applied magnetic field (Fig. 7.3). If there is no initial magnetic moment, magnetization increases with magnetic field to the saturation value. As the applied magnetic field decrease to zero and then to negative values, the magnetization curve outlines a characteristic hysteresis. An important parameter of a ferromagnetic material is the Curie temperature, T_C. The magnetic moment of a ferromagnetic material decreases with temperature, and can be destroyed completely at $T > T_C$.

In ionic materials different types of ions can form sublattices with different magnetic moments, which can partially compensate each other resulting in nonzero net magnetic moment. Such materials are referred to as ferrimagnets. Ferrimagnets have analogous properties to ferromagnetic material (spontaneous magnetization, hysteresis, Curie temperature); however, their magnetic ordering has different mechanism. When magnetic moments of sublattices in ionic materials have equal values but different directions, they completely cancel each other producing the antiferromagnetic materials. The magnetic susceptibility of antiferromagnets increases linearly with temperature up to the Néel temperature, T_N. At $T > T_N$ they become paramagnetic.

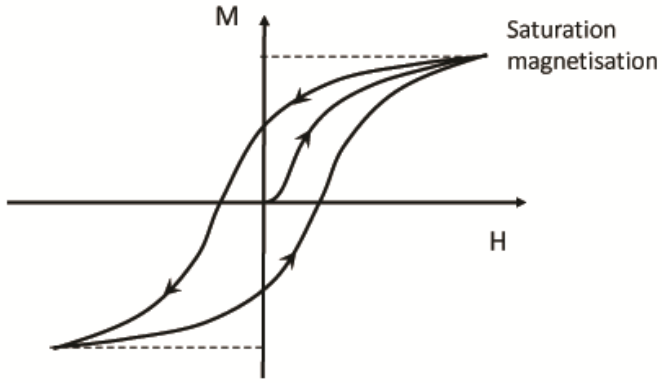

Figure 7.3. Dependence of magnetization, M, on an applied magnetic field, H, in ferromagnetic material.

7.3 Origin of magnetism in dilute magnetic materials

Magnetism of dilute magnetic materials can originate from different mechanisms. In the traditional dilute magnetic semiconductors and oxides, the doping of a host with transition metal ions has been used for development of new magnetic materials. A schematic representation of a diluted magnetic semiconductor (DMS) is shown in Figure 7.4 [3]. A number of different semiconductors have been used as a host: common Si, II-IV (such as CdTe, ZnSe) or III-V semiconductors (such as GaAs, InAs). However, ferromagnetism in these systems is often observed at low temperatures only, with the Curie temperatures below 100 K. Promising results have been observed for ZnO and TiO_2 doped with different transition metals including V, Cr, Mn, Fe, Co, and Ni [4-10]. Following that success, several theories have been developed for the explanation for the origin of ferromagnetism in DMS based on exchange models (both direct and carrier mediated) and double exchange model [11, 12]. In the dilute magnetic semiconductors and oxides, magnetic ions are spatially straddled, and direct exchange is inefficient. In such systems, magnetic ordering can be mediated by intermediate anions (*indirect superexchange model*), by free electron gas (*carrier-mediated exchange model),* or by both *(double exchange theory*).

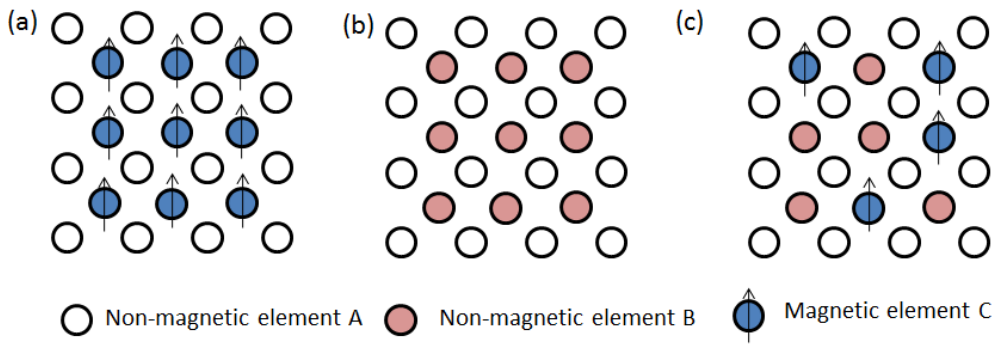

Figure 7.4. Schematic representation of (a) magnetic semiconductor, (b) non-magnetic semiconductor, and (c) diluted magnetic semiconductor. Redrawn in the style of Ref. [3].

Another field is emergent magnetism, the phenomenon where magnetic ordering appears in nanostructures of materials that are nonmagnetic in the bulk, and generally in any material that is not a traditional d-band magnet [13]. Magnetism at the interfaces of thin films or multilayers is one of the interesting phenomena possible in oxide materials. The difference in the lattice parameters causes strain, broken crystal symmetry, and rotation of oxygen octahedra, and often electronic reconstruction is required to restore local charge neutrality. The disturbances of symmetry can produce the magnetic, charge or orbital ordering which extends in just several atomic layers [14].

7.3.1 Exchange in insulators

(a) In *the direct exchange* model, the direct exchange interactions of spins s_i of localized electrons in *insulators* can be described by the Heisenberg Hamiltonian:

$$H_{ex} = -\sum_{ij} J_{ij} s_i \cdot s_j , \qquad (7.2)$$

where J_{ij} is the exchange integral.

In order to result in a magnetic state, spins must interact between themselves effectively. The exchange integral J_{ij} can be positive (when the spins align parallel) and negative (when two electrons localized on the neighboring atoms are aligning antiparallel). In a solid with unpaired electrons both situations are possible. Typically in a

solid, the coupling can result in parallel alignment of spins (if electrons belong to a free atom) or antiparallel (for electrons localized on the neighboring atoms). More often the antiparallel alignment dominates leading to antiferromagnetism.

(b) Superexchange is an indirect exchange occurring in ionic solids such as oxides and fluorides where bonding orbitals are formed by 3d electrons in transition metal atoms and 2p valence electrons in diamagnetic oxygen or fluorine. Magnetic interactions between transition metal ions can be mediated by the intermediate anions. The size of the exchange integral depends on: the d electron configuration of the transition metal, on metal-oxygen orbital overlap, and on the metal-oxygen-metal bond length and angle. These dependences are summarized in the semi-empirical Goodenough–Kanamori–Anderson rules, as follows [10]:

1. 180º exchange between half-filled orbitals is strong and antiferromagnetic;

2. 90º exchange between half-filled orbitals is ferromagnetic, and rather weak;

3. Exchange between half-filled orbitals and empty orbitals of different symmetry is ferromagnetic, and rather weak.

Figure 7.5 demonstrates superexchange interaction involving half-filled Mn^{2+} ions and O^{2-} ions in MnO. When the 2p electron with ↓ spin is transferred to Mn on the left, a 2p hole of O can be filled by an electron from the Mn on the right provided it also has ↓ spin [10].

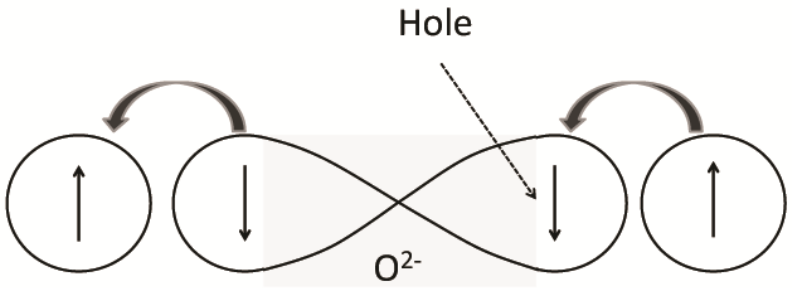

Figure7.5. Superexchange interaction between d shells via O^{2-} ions. Redrawn in the style of Ref. [11].

7.3.2 Carrier-mediated exchange

The carrier-mediated exchange model requires involvement of the free carriers into magnetic interactions between localized magnetic moments. The model can be described in three limiting cases: the Rudermann–Kittel–Kasuya–Yosida (RKKY) interaction, Zener carrier-mediated exchange, and Zener double exchange. In the RKKY model the interaction is described quantum mechanically by

$$J(R) = \frac{m^* k_F^4}{h^2} F(2k_F R) \qquad (7.3)$$

where m^* is the effective mass, k_F is the Fermi wavevector of the electron and $F(x)$ is the oscillating function:

$$F(x) = \frac{x\cos x - \sin x}{x^4} \qquad (7.4)$$

The oscillating nature of RKKY interaction arises from the wave nature of "free" conducting electrons. They rearrange themselves to minimize their energy after scattering on an atom, causing charge and spin density to oscillate around the scattering center. The Zener model explains ferromagnetic ordering by the lowering of the carrier energy in the result of the redistribution between spin subbands which are split apart by the exchange interactions [15]. One of variants of this model is the Zener double exchange model proposed for a particular case of the doped perovskite structure manganites $La_{1-x}A_xMnO_3$, involves the ability of a TM ion to adopt different valences. As in the superexchange model, magnetic coupling between neighboring TM ions with (*n-1*) and *n* valency (for example, Mn^{3+} and Mn^{4+}) is mediated by oxygen atoms but with involvement of free carriers [15].

The difference with the super-exchange model consists in that the indirect coupling between two atoms occurs through the outer electronic states of TM atoms themselves rather than through the electronic state of an intermediate atom [12].

7.3.4 d^0 magnetism theory

The exchange models require the existence of a high concentration of free carriers, electrons and holes, which is often not applicable to DMSs. These models do not provide a satisfactory explanation for the magnitude of magnetism in dilute oxides. In oxide materials doped with transition metals, room-temperature ferromagnetism has been observed at doping concentrations below percolation level [16-23]. Typically, in these studies the transition metal dopant concentration has not exceeded 5%-10%. At such low concentration, the TM ions are too scarce to interact with each other (directly or through intermediate oxygen atoms) and cannot provide significant ferromagnetic moment. In the same way these theories cannot explain magnetism observed in carbon materials where d-electrons are absent. Furthermore, magnetic properties strongly depend on the state of TM doping ions in the host oxide crystal. Studies of oxides and carbon materials have shown that maximum magnetism can be observed in a narrow range of TM doping and/or defect concentration [24, 25].

d^0 magnetism model considers the lattice defects as a cause of ferromagnetic response [26, 27]. The theory was suggested by Coey [28] for explanation of magnetism observed in graphite and other materials composed only of light elements such as boron nitride.

If there is a sufficient density of such defects, an impurity band is formed in the band gap. Magnetic ordering is provided by spontaneous spin-splitting of the band (Fig. 7.6). In a slightly different scenario magnetic moment is associated with the molecular orbitals localized in the vicinity of the defects. As a result, a long-range ferromagnetic exchange is mediated by the interactions between the orbitals localized in the vicinity of the defects.

For the case of dilute ferromagnetic oxide materials d^0 theory was modified into the charge transfer theory. Typically, oxides contain intrinsic defects: oxygen vacancies and metal interstitials. Charge transfer ferromagnetism requires three main components to produce magnetic ordering: (i) a defect-based band with a high density of states in the

vicinity of the Fermi level; (ii) a proximate charge reservoir to or from which electrons can be easily transferred; and (iii) an effective exchange integral *J* associated with the defect states [29].

The impurity band should not be conductive itself. If the localization length is greater than the distance between magnetic centers, a ferromagnetic state with high Curie temperature can be formed as a result. When the 3d↑ and 3d↓ states mix up with the spin-split impurity band, they give rise to ferromagnetic interactions (Fig. 7.6) [30].

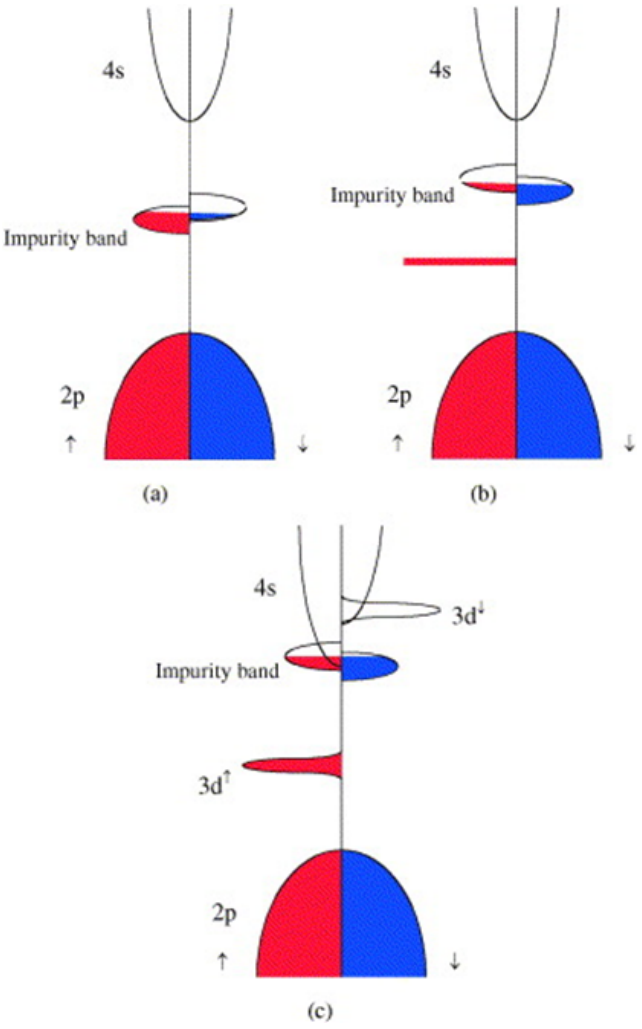

Figure 7.6 Spin-split impurity band mediate ferromagnetic state. (a) Spontaneous spin-splitting; (b) spin-splitting due to magnetic defects or impurities; (c) population of unoccupied d band by overlap with an impurity band, which lead to spin-splitting of the latter. Reprinted with permission from Ref. [29].

Transition metal doping is not a main cause of magnetism in dilute oxides. TM ions with the variable valence, that can exist in different states such as Ti^{3+}/Ti^{4+}, Mn^{3+}/Mn^{4+}, Fe^{2+}/Fe^{3+}, Co^{2+}/Co^{3+}, or Cu^{+}/Cu^{2+}, act as a charge reservoir. Provided the exchange integral is large enough, the energy gain from the exchange splitting compensates the energy cost of the electron transferring from the charge reservoir. Electrons are transferred between the charge reservoir and the impurity band, until the density of states $D(E_F)$ in the defects band increases to the point where the Stoner criterion is satisfied: $JD(E_F)>1$ (Fig. 7.7).

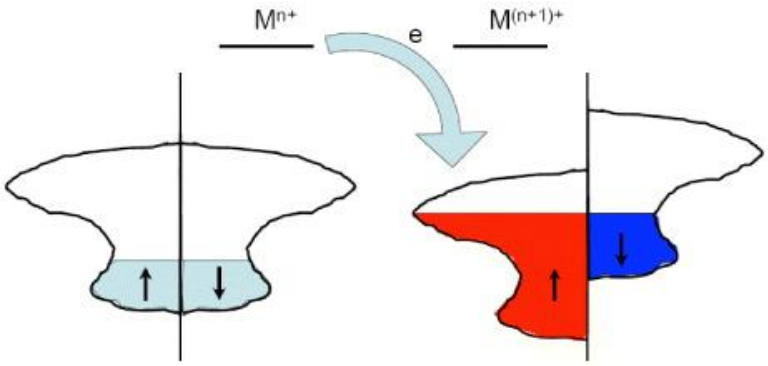

Figure 7.7. Schematic of charge transfer mechanism. Electrons transfer to or from the charge reservoir to the impurity band leading to spontaneous ferromagnetic splitting. Reprinted with permission from Ref. [30].

7.4 Role of defects on boundaries and interfaces

In contrast to the classical Stoner ferromagnets with uniform magnetization, in dilute oxides (or any material that is not a traditional d-band magnet) only regions containing defects become ferromagnetic while the rest of the material stays nonmagnetic in the bulk. This so-called emergent magnetism, confined to defects located in thin films and in grain-boundary regions, has been found in a variety of materials including graphite and graphene, metal oxides and nanocrystals of nonmagnetic metals like Au [11, 28, 30, 31]. The defect states can be associated with the surfaces of randomly distributed nanoparticles, with spinoidal decomposition of the material, with grain boundaries or with surfaces or interfaces of thin film (Fig 7.8) [30].

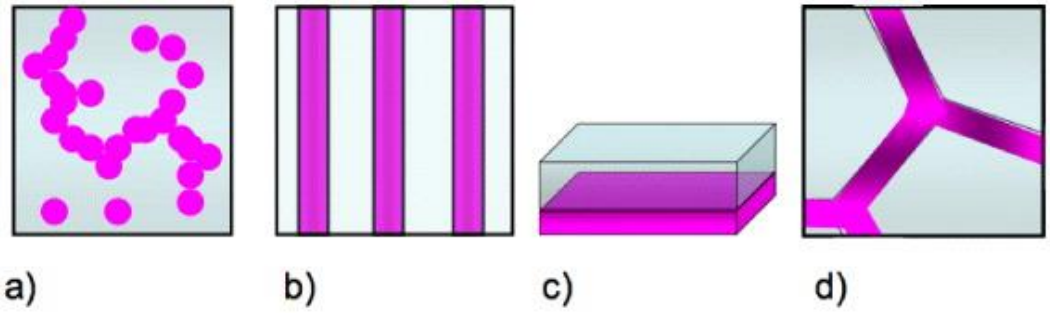

Figure 7.8. Inhomogeneous distribution of ferromagnetic region in a dilute oxide: a) random distribution of ferromagnetic particles; b) spinoidal decomposition; c) interface/surface defects; d) grain boundaries. Reprinted with permission from Ref. [30]

Progress in synthesis methods allows fabricating magnetic structures with atomic or molecular precision including nanoparticles, core-shell structures, nanowires, nanotubes, thin-film and multilayer structures [32]. However experimental success in reaching high Curie temperatures reproducibly in such systems is still moderate. Research in the area of dilute magnetic materials suffers from the lack of reproducibility because usually defects are not in thermodynamic equilibrium, and their concentration and distribution evolves irreversibly upon heating. Thus, vacancies can migrate through the crystal forming clusters, or get pinned on the crystallographic steps or by foreign adatom [31, 33].

7.5 Magnetism in oxide materials

Numerous studies report magnetic properties of strontium titanate induced by doping with transition metals and defects. Ferromagnetic properties have been found in strontium titanate doped with Mn, Fe Co, and Nb [34-37]. The magnetic properties have been observed at low level TM metal doping below the percolation level. Magnetism has been also detected in strontium titanate without the TM doping [38-41]. Despite the vast variety of systems and different fabrication methods applied, based on these studies most of the authors have agreed that the origin of magnetism in strontium titanate is mostly due to oxygen vacancy defects.

Dulov *et al.* [35] studied Fe implanted STO crystals using Mössbauer spectroscopy. Several diluted phases of strontium titanate with substitution of Ti^{4+} ions by

Fe^{2+} or Fe^{3+} were identified. However the authors found that most of the implanted iron in their high-fluence implanted STO ($1.5x\ 10^{17}$ Fe ion/cm^2) was in α-Fe nanoclusters which defined the magnetic behavior at room temperature.

Zhang *et al.* [42] found a positive correlation between ferromagnetism and doping concentration in Co-doped $SrTiO_3$ nanofibers in the 50-300ºK temperature range. In their experiment, Co was incorporated into STO structure in Ti sites without any phase separation of metallic Co or Co oxide. Ferromagnetism of Co:$SrTiO_3$ nanofiber samples were related to oxygen vacancies because their magnetic moments increased considerably upon annealing in H_2.

Zeng *et al.* [24] studying magnetism of iron doped $LiNbO_3$ observed the highest magnetic moment for 1 % Fe doping substituting on Li sites. Further increase of Fe concentration led to significant decreasing of the magnetic moment due to the formation of FeO_x clusters.

Numerous studies have mentioned defect induced ferromagnetism in pure strontium titanate crystals. Strong ferromagnetism was observed in laser annealed un-doped STO crystals [39]. The researches ascribed it to coupling between spin polarized oxygen vacancies and localized Ti 3d electrons. Rice et al. observed a persistent ferromagnetic state created in strontium titanate under laser irradiation [40]. Xu et al. studied STO films grown by the molecular beam epitaxy method on (100) STO substrates. They found ferromagnetic behavior in the films that was not observed in the bulk crystal [41]. The authors explained it by the presence of oxygen vacancies in the epitaxial films.

Great attention has recently been attracted by the $LaAlO_3/SrTiO_3$ interface. The unusual properties of the heterostructure related to polarity discontinuity in the interface area resulting in nontrivial local atomic and electronic structure. An STO crystal consists of alternating non-polar layers of SrO and TiO_2, whereas $LaAlO_3$ consists of polar positively charged $(LaO)^+$ and negatively charged $(AlO_2)^-$ layers. This leads to the appearance of a two-dimensional electron gas (2DEG) in the interface between TiO_2-terminated STO and $LaAlO_3$ as well as non-zero magnetic moment [43-46]. It was found

that the interface of $LaAlO_3/SrTiO_3$ has metallic behavior in the presence of oxygen vacancies. Although origin of the magnetism is still under debate, most authors ascribe it to electrons in Ti 3d t_{2g} orbitals. Similar properties are possible for other heterostructures, such as $SrTiO_3/SrRuO_3$ and $TiO_2/SrTiO_3$ [47, 48].

7.6. Defect induced magnetism in graphite materials

Graphite-based materials have attracted a great deal of attention due to their unique structural, mechanical, electronic and thermal properties. Pure carbon materials (including graphene and graphite) are not ferromagnetic by themselves. However, weak ferromagnetism was found in carbon-based materials, and in many cases ferromagnetic properties were observed in high-temperature experiments [25, 49-52]. The possible combination of magnetic and semiconducting properties in graphite materials makes them the promising candidates for semiconductor spintronics technology. The interest in graphite magnetism is increasing even though experimental results are suffering from poor reproducibility.

Numerous studies indicate defect-related magnetism in graphite. Calculations show that the ground state of a single vacancy in graphene layer has a magnetic moment of 1.04 μ_B formed by an unsaturated sp^2 dangling bond [53]. The studies also show that the magnetic moment can depend on the type of ions used for ion beam modification of graphite structure. For example, in the case of a proton beam, a hydrogen atom can be absorbed directly into the vacancy, forming a metastable configuration with a magnetic moment of 2.3 μ_B. Two H atoms absorbed on a vacancy create a stable configuration with a magnetic moment of 1.2 μ_B localized on the dangling sp^2 bond. Another stable configuration can be formed when a hydrogen atom is pinned by a carbon adatom. This C-H group has a magnetic moment of 0.9 μ_B [53].

Spin-polarized density functional theory (DFT) calculations on graphene fragments and nanoribbons show that magnetic moments reside mainly on the zigzag edges; the armchair-edged nanoribbons stay non-magnetic [54, 55]. Calculations conducted for multiple vacancies (nanoholes) in the graphene layer revealed that such

holes with the zigzag edges can possess high stability and have magnetic state with a finite-energy band gap [56]. At the same time the electronic properties of a single C vacancy in a well-decoupled graphene layer differ significantly from the electronic properties of a graphene layer on a metal substrate. Thus, a study conducted by Ugeda *et al.* [57] discarded the possibility to induce magnetism in the latter systems. A recent study of graphene nanoribbons has reported paramagnetic centers associated with the zigzag edges and vacancy defects [58, 59].

There are many researches who work on the connection between the concentration of defects in graphite and its magnetic properties. Ion irradiation produces multiple vacancies in graphite [25, 50, 60, 61]. The implanted atoms (neutralized ions) can stay between carbon layers or substitute for one of the C atoms. However, experimental results on ion irradiated highly oriented pyrolytic graphite (HOPG) vary from each other. Horne *et al.* [61] found ferromagnetic properties in HOPG samples both virgin and implanted with Fe, F and B ions. Nevertheless they did not detect a correlation between ferromagnetism and implantation doses and did not observe a clear influence of Fe implantation on ferromagnetism. Yang *et al.* [50] observed an increase in total magnetic moment of graphite implanted with 70 eV C^+ ions due to vacancies. Similar conclusions were made for 2.25 MeV proton irradiated graphite. The authors noted the possibility to create ferromagnetic areas with sharp borders by introducing defects into HOPG [60].

In a recent research, highly oriented pyrolytic graphite samples were irradiated by C^+ ions in a four-step implantation process which produced a 160 nm layer of uniformly distributed vacancies [25]. Using the combination of X-ray absorption near edge structure spectroscopy and bulk magnetization measurements, the authors established a clear correlation between implantation dose (or disorder extent) and magnetic moments. At first the magnetic moment increased with implanted dose. However, as the implantation dose farther increased, the defect concentration became so high that it destroyed magnetic ordering, and the magnetic moment decreased (Fig. 7.9). A pre-edge peak in the XANES spectrum at ~ 283 eV was ascribed to vacancy defects formed under irradiation conditions. The defect-induced electronic states at the Fermi level were identified as the origin of ferromagnetism in the HOPG samples.

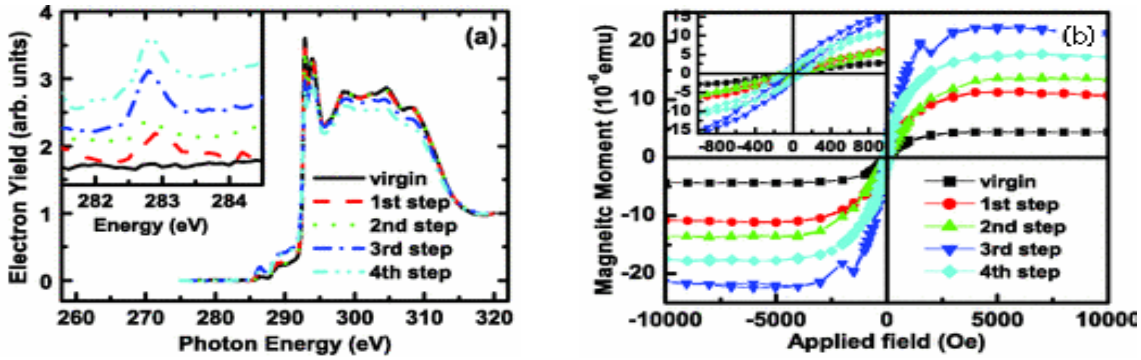

Figure 7.9. (a) C *K*-edge XANES spectra of HOPG and (b) corresponding magnetic hysteresis loops at each of the four steps of C^+ ion implantation: 1) 70 keV and 1×10^{15} ion/cm^2; 2) 50 keV and 3×10^{14} ion/cm^2; 3) 30 keV and 3×10^{14} ion/cm^2; and 4) 15 keV and 2×10^{14} ion/cm^2. Reprinted from Ref. [25].

7.7 SQUID measurements for STO and HOPG samples: experimental details

In this work, the magnetic properties of STO and HOPG samples were measured with a Quantum Design MPMS XL-5 SQUID magnetometer, at the Department of Physics, Dalhousie University. Samples were handled with special care to avoid any contact with metal tools. During measurements, the samples were placed in a clear plastic straw and oriented such that the magnetic field was applied along the STO[100] direction and along the graphene planes of the HOPG pieces (within an experimental resolution of ±3%). The field dependence of the magnetic moment M(H) was done at 5°K and at 300°K.

The temperature dependence of magnetization was measured as the remanent magnetic moments. The samples were saturated in a 5T magnetic field at low temperature (T=5°K). After setting the magnetic field to zero, the SQUID magnetometer was reset to remove any remaining magnetic flux trapped in the coils. The remanent moment was then measured up to 400°K while warming the sample.

7.7.1. Magnetism of Fe implanted STO samples

The measured magnetic moments M(H) showed both linear diamagnetic and nonlinear ferromagnetic behavior. (Fig.7.10). Since only a near-surface layer of STO crystal substrate is affected by Fe implantation, all magnetic moment presented here are shown as they were measured (without dividing on the sample volume or mass), since all samples had the same dimensions. Such procedure allowed comparing between virgin STO and implanted STO samples.

The susceptibility χ of STO crystals was calculated from the slopes measured by making linear fits in the higher field regions ($-5000 \le H \le -2000$ and $2000 \le H \le 5000$ *G*). There is a slight deviation in the slops which reflect the value of the magnetic susceptibility χ. The average value of susceptibility was -0.88×10^{-7}emu/Oe·cm^3 and -1.02×10^{-7}emu/Oe·cm^3 at 5 K and at 300 K, respectively, which is within 2% of the published values [62].

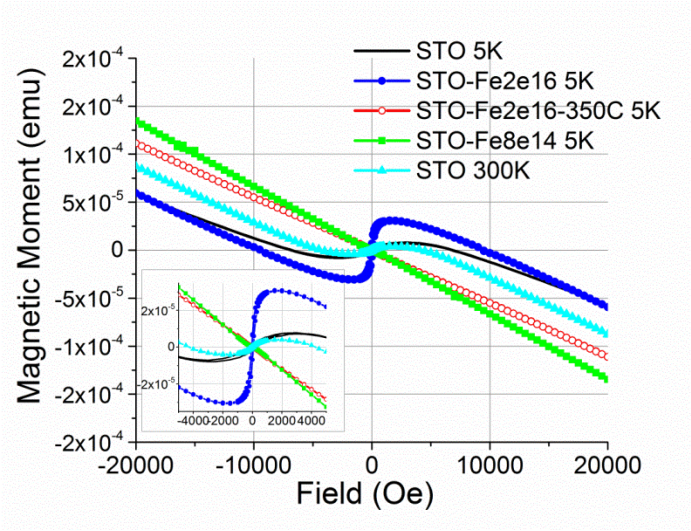

Figure 7.10. Magnetic moment (M) vs. field (H) curves of STO samples before subtraction of diamagnetic component.

To reveal the non-linear hysteresis part and to quantify saturation moments for implanted and un-implanted samples, the linear diamagnetic contribution was subtracted from the M(H) curves. Magnetic moments as a function of applied field M(H) measured at 5°K for several STO samples are presented in Figure 7.11(a). Notably, un-implanted

STO crystal had a weak magnetic moment. Previous studies showed that surface contaminations are often responsible for the magnetism of strontium titanate crystals, in the presence of ferromagnetic impurities. The studies showed that when magnetic impurities were deleted by the surface polishing, the initial magnetic moment of several oxide substrates decreased significantly [63, 64].

The effects of oxygen vacancies on the ferromagnetism in rutile TiO_2 have also been demonstrated based on first-principles local density approximation (LDA+*U)* calculations [65]. Their results show that the magnetic moment depend on the oxygen vacancies concentration *x*, and predicted the ferromagnetism in rutile TiO_{2-x} with $x > 0.0417$. Oxygen vacancies not only modulate the valence of neighboring transition metal elements but also cause a change of the band structure of the host oxides [66]. Therefore one can achieve ferromagnetism by increasing vacancy concentrations above a certain threshold, while still keeping ordering within the crystalline lattice of the host material. And experimentally, oxygen anneal typically decreased magnetic moment in contrast to vacuum anneal [65].

Our strontium titanate crystal was annealed in pure oxygen for 2 hours to reduce oxygen vacancies that can be initially present on the surface. The magnetic moment of STO-350 after subtraction of the diamagnetic contribution was considerably lower than that of un-implanted STO (Fig. 7.11(a)).

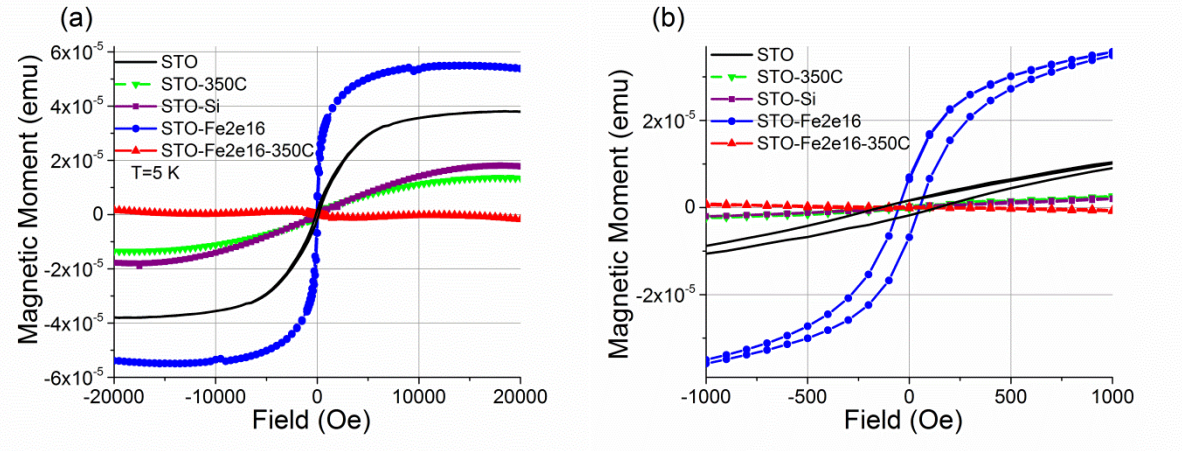

Figure 7.11 Magnetic moment (M) vs. field (H) curves of un-implanted STO and STO-350, Fe implanted samples STO-Fe2e16 and STO- Fe2e16-350C, and Si implanted STO after subtraction of diamagnetic contribution.

To further explore the role of oxygen vacancies in the magnetic properties, STO substrate was implanted with non-magnetic silicon ions. The M(H) curve for STO-Si sample after subtraction of the diamagnetic contribution is also presented in Figure 7.11. The Si implantation led to reduction of the magnetic moment by approximately a factor of two compared to the sample before implantation. Though the implanted layer in STO-Si sample was thicker than that in the Fe ion implanted samples, the dose of 2×10^{16} Si ion/cm^2 produced comparable level of damage (~1.6×10^{19} V_o/cm^2) but with non-magnetic ions. These vacancies are abundant, however they are not well ordered, and do not contribute to the magnetic moment. Additionally, the Si-implanted sample exhibited no ferromagnetic hysteresis loop (Fig. 7.11(b)), and the saturation of M(H) of STO-Si sample is reached at high values of magnetic field of 15 kOe, suggesting soft-ferromagnetic behavior.

Implantation of a high dose of iron (2×10^{16} Fe^+ ion/cm^2) resulted in a magnetic moment with a ferromagnetic hysteresis loop due to the oxygen vacancies and presence of Fe atoms (Fig. 7.11(b)). Remarkably, the STO-Fe8e14 sample with a medium implantation dose of Fe has a lower magnetic moment compared to un-implanted STO crystal (Fig. 7.12(a)). Ion implantation introduces disordering to the crystal structure. The disordering destroyed the initial magnetic moment of the un-implanted strontium titanate crystals, and the dose of Fe doping in STO- Fe8e14 sample has been too low to produce magnetic phases, which could increase the magnetic moment.

Post-implantation annealing in oxygen of sample STO-Fe2e16-350C led to a decrease in the magnetic moment to zero (Fig. 7.11(a)). Post-implantation annealing in oxygen contributes to two different effects. First, it partially heals oxygen vacancies produced during ion implantation. Second, annealing should reduce ferromagnetic domains due to Fe^0. According to XANES results the iron oxidation state changed from Fe^0 to Fe^{3+} with iron substituting for Ti ions in the STO crystal structure. The process destroys the ferromagnetic order, and the implanted and then annealed STO-Fe2e16-350C sample becomes purely diamagnetic.

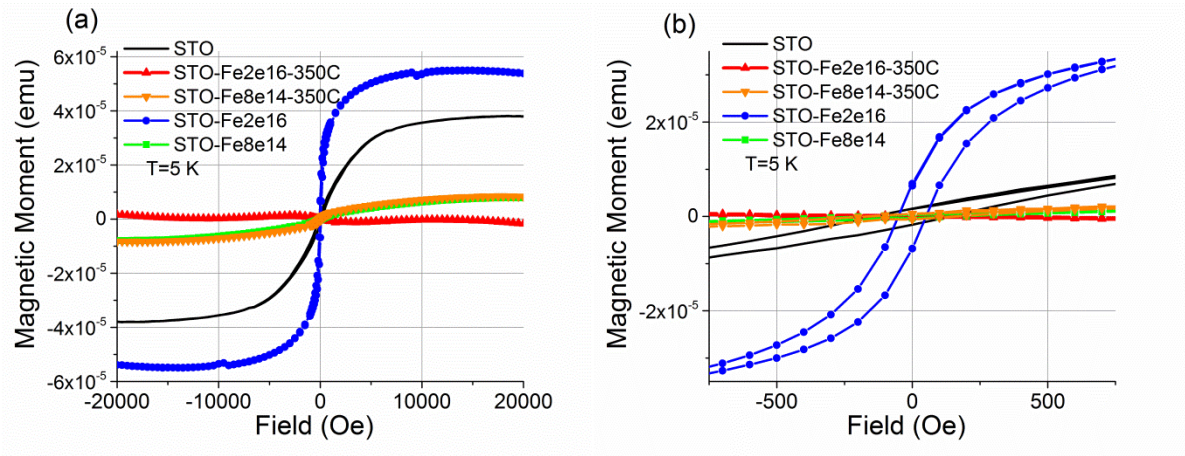

Figure 7.12 (a) Magnetic moment (M) vs. field (H) curves of un-implanted STO and STO implanted different Fe doses after subtraction of diamagnetic contribution; (b) enlarged part with ferromagnetic hysteresis.

Experimental research conducted on commercially available oxide substrates showed that surface contamination on the surface is often the most probable explanation for the observed ferromagnetic behavior in many cases [63, 67]. Metal particles are often left on the surface when single-crystals are cut into separate pieces. In the work by Yee *et al.* several commercial substrates (including intrinsically diamagnetic or paramagnetic) were examined [68]. All unpolished crystals used in the research (Al_2O_3, $LaAlO_3$, $SrTiO_3$, TiO_2, and ZnO) have showed initial magnetic moment due to excess iron, possibly in the form of a mixture of Fe, Fe_3O_4, and/or γ-Fe_2O_3. The magnetic moment of the crystals has been reduced considerably when crystal surfaces were polished and cleaned of metallic contaminations [31]. A series of studies show chemical and/or structural segregation of the transition metal dopants into non DMS phases [69-72]. So, special care was taken to handle the STO samples with Teflon tweezers to avoid additional metal contaminations on the surface.

The remanent magnetization curves for selected STO samples are presented in Figure 7.13. No phase transitions were found in any of the samples. They show monotonic behaviour typical for diamagnetic materials with small paramagnetic contribution at very low temperatures.

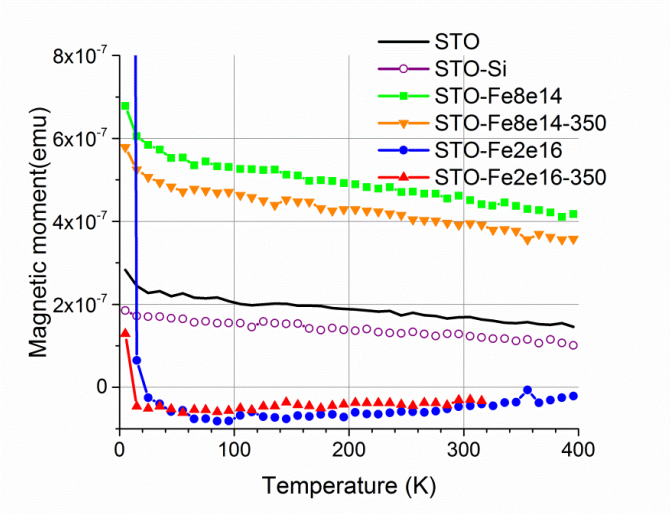

Figure 7.13. Remanent magnetization of STO samples.

7.7.2. Magnetic properties of N and O implanted HOPG.

The magnetic measurements of graphite samples were conducted as was described above. The magnetic moments are presented as they were measured without dividing by the sample volume because HOPG samples had irregular shapes and their volumes (or masses) can be estimated only with high uncertainty.

The field dependence of the magnetic moment was measured for three graphite samples, virgin HOPG, HOPG-N5e15 and HOPG-O5e15. The magnetic moments of HOPG samples were diamagnetic in general (Fig. 7.14(a)). Difference in the M(H) dependence slopes was probably reflecting the different dimensions of the tested samples. In the low magnetic field, a ferromagnetic–like hysteresis was observed on M(H) dependences. Magnetic moments of the HOPG samples after subtracting a linear diamagnetic contribution are presented in Figure 7.14(b). They demonstrated roughly the same value of magnetization. As followed from PIXE analysis the tested samples had high contents of iron impurities. It indicated that the most probable origin of magnetism in the tested HOPG samples were the metal impurities. Distortion of hysteresis curves seen in Figure 7.14(b) were connected to the difficulties of measuring weak small magnetic moments on a strong diamagnetic substrate [73].

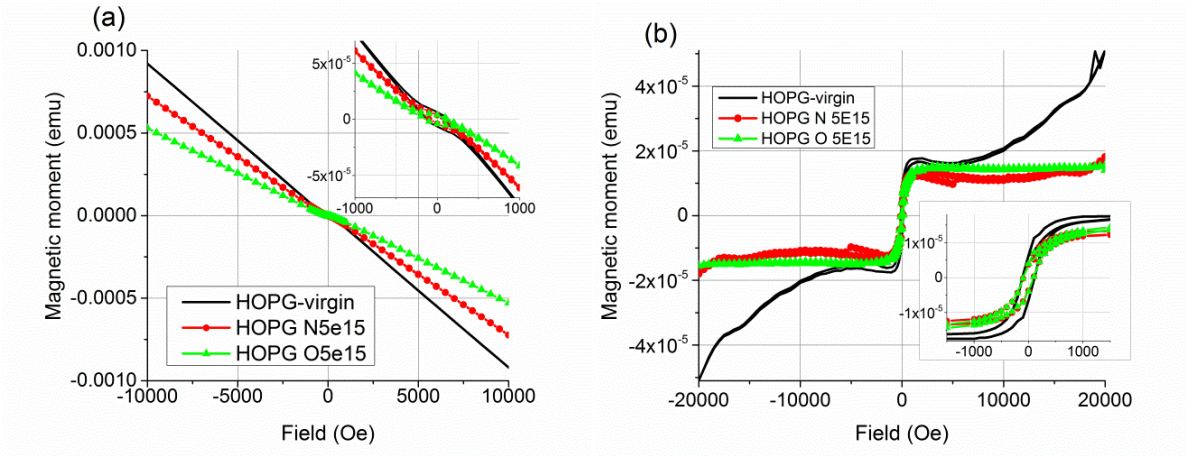

Figure 7.14. Magnetic moment of HOPG samples: (a) before and (b) after subtraction of the diamagnetic contribution. Inserts show enlarged image of hysteresis part.

The remanent magnetic moments of HOPG samples were measured in the range from 5°K to 400°K as was described above for STO samples. The magnetic moments of all HOPG samples decreased monotonically with temperature (Fig. 7.15). The temperature dependence did not reveal any phase transformations.

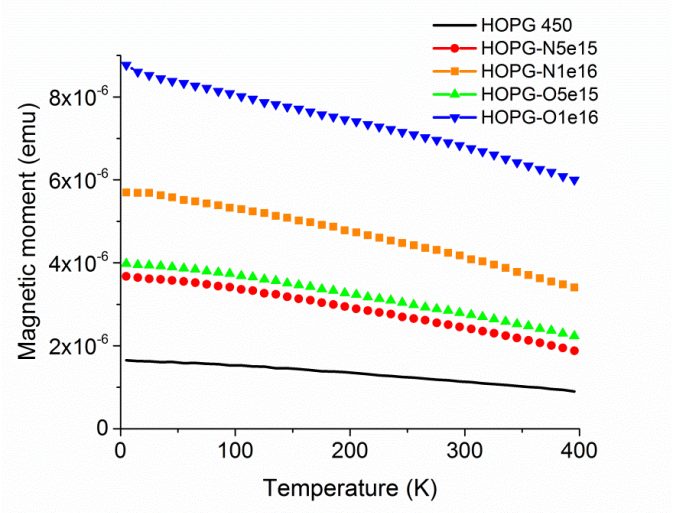

Figure 7.15. The temperature dependence of the remanent magnetic moments of HOPG samples.

Metal inclusions have been found in widely used HOPG of ZY-grades.[74-76] Sepioni et al. (74) studied ZYA-, ZYB-, and ZYH-grades from different manufacturers and found particles of ~ 5 μm in diameter containing Fe, Ni, Ti, Cr and V. There is also a different concentration of these metal inclusions at different depths of the HOPG crystal. Venkatesan et al. found more impurities in the middle part of a HOPG crystal when it was cleaved on several layers [77]. This shows that the quality (purity) of the initial oxide and graphite substrate is very important for magnetic studies.

In summary, the magnetic measurements showed that STO and HOPG samples were mostly diamagnetic. The unimplanted STO crystals demonstrated weak ferromagnetic moments due to vacancy states on the surface. Iron implantation at the highest implantation dose used in this research (2×10^{16} ion/cm^2) increased the magnetic moment. The oxidation state of iron doping was Fe^0 directly after implantation. Annealing in O_2 atmosphere, which removed oxygen vacancies and oxidized iron to $Fe^{2+/}Fe^{3+}$ state, destroyed this magnetic ordering. Lower implantation doses of Fe decreased the magnetic moments as the ion irradiation perturbed the initial magnetic ordering observed in the unimplanted STO crystals. Ferromagnetic contribution to the magnetic moments observed in HOPG samples was chiefly due the metal inclusions. The temperature dependence of the magnetic moments of the STO and HOPG samples did not show any phase transitions.

References

[1] T. Dietl, H. Ohno, F. Matsukura, J. Cibert, D. Ferrand, Zener model description of ferromagnetism in zinc-blende magnetic semiconductors, Science 287 (2000) 1019-1022.
[2] H. Raebiger, S. Lany, A. Zunger, Electronic structure, donor and acceptor transitions, and magnetism of 3D impurities in In_2O_3 and ZnO, Phys Rev B 79 (2009) 165202.
[3] H. Ohno, Making nonmagnetic semiconductors ferromagnetic, Science 281 (1998) 951-956.
[4] B. Zhang, Q.H. Li, L.Q. Shi, H.S. Cheng, J.Z. Wang, Room temperature ferromagnetism of Fe-implanted ZnO film, Journal of Vacuum Science & Technology A 26 (2008) 1469-1473.
[5] K. Ueda, H. Tabata, T. Kawai, Magnetic and electric properties of transition-metal-doped ZnO films, Applied Physics Letters 79 (2001) 988-990.
[6] K. Kikoin, V. Fleurov, On the nature of ferromagnetism in non-stoichiometric TiO_2 doped with transition metals, Journal of Magnetism and Magnetic Materials 310 (2007) 2097-2098.
[7] J.M.D. Coey, M. Venkatesan, C.B. Fitzgerald, L.S. Dorneles, P. Stamenov, J.G. Lunney, Anisotropy of the magnetization of a dilute magnetic oxide, J Magn Magn Mater 290 (2005) 1405-1407.
[8] Y. Yamada, K. Ueno, T. Fukumura, H.T. Yuan, H. Shimotani, Y. Iwasa, L. Gu, S. Tsukimoto, Y. Ikuhara, M. Kawasaki, Electrically Induced Ferromagnetism at Room Temperature in Cobalt-Doped Titanium Dioxide, Science 332 (2011) 1065-1067.
[9] Z.J. Wang, J.K. Tang, H.G. Zhang, V. Golub, L. Spinu, L. Tung, Ferromagnetism in chromium-doped reduced-rutile titanium dioxide thin films, J Appl Phys 95 (2004) 7381-7383.
[10] R. Janisch, P. Gopal, N.A. Spaldin, Transition metal-doped TiO_2 and ZnO - present status of the field, Journal of Physics-Condensed Matter 17 (2005) R657-R689.
[11] J.M.D. Coey, Handbook of spin transport and magnetism, CRC Press; CRC Press; CRC Press, Boca Raton; Boca Raton; Boca Raton, 2012.
[12] J. Stöhr, H.C. Siegmann, Magnetism :from fundamentals to nanoscale dynamics, Springer, Berlin, 2006.
[13] A. Enders, R. Skomski, J. Honolka, Magnetic surface nanostructures, Journal of Physics-Condensed Matter 22 (2010) 433001.
[14] J.M.D. Coey, Ariando, W.E. Pickett, Magnetism at the edge: New phenomena at oxide interfaces, MRS Bulletin 38 (2013) 1040-1047.
[15] C. Zener, Interaction between the D-Shells in the Transition Metals.2. Ferromagnetic compounds of manganese with perovskite structure, Physical Review 82 (1951) 403-405.
[16] Y. Matsumoto, M. Murakami, T. Shono, T. Hasegawa, T. Fukumura, M. Kawasaki, P. Ahmet, T. Chikyow, S. Koshihara, H. Koinuma, Room-temperature ferromagnetism in transparent transition metal-doped titanium dioxide, Science 291 (2001) 854-856.
[17] Z.J. Wang, W.D. Wang, J.K. Tang, L.D. Tung, L. Spinu, W.L. Zhou, Extraordinary Hall effect and ferromagnetism in Fe-doped reduced rutile, Applied Physics Letters 83 (2003) 518-520.

[18] S.J. Han, J.W. Song, C.H. Yang, S.H. Park, J.H. Park, Y.H. Jeong, K.W. Rhie, A key to room-temperature ferromagnetism in Fe-doped ZnO: Cu, Applied Physics Letters 81 (2002) 4212-4214.
[19] S.K. Sharma, P. Thakur, S. Kumar, D.K. Shukla, N.B. Brookes, C.G. Lee, K.R. Pirota, B.H. Koo, M. Knobel, Room temperature ferromagnetism in Fe-doped CeO_2 thin films grown on $LaAlO_3$ (001), Thin Solid Films 519 (2010) 410-413.
[20] K. Tanaka, K. Fujita, Y. Maruyama, Y. Kususe, H. Murakami, H. Akamatsu, Y. Zong, S. Murai, Ferromagnetism induced by lattice volume expansion and amorphization in $EuTiO_3$ thin films, Journal of Materials Research 28 (2013) 1031-1041.
[21] T. Tietze, M. Gacic, G. Schuetz, G. Jakob, S. Brueck, E. Goering, XMCD studies on Co and Li doped ZnO magnetic semiconductors, New Journal of Physics 10 (2008) 055009.
[22] B.B. Straumal, A.A. Mazilkin, S.G. Protasova, A.A. Myatiev, P.B. Straumal, G. Schuetz, P.A. van Aken, E. Goering, B. Baretzky, Magnetization study of nanograined pure and Mn-doped ZnO films: Formation of a ferromagnetic grain-boundary foam, Phys Rev B 79 (2009) 205206.
[23] J.B. Torrance, M.W. Shafer, T.R. McGuire, Bound Magnetic Polarons and Insulator-Metal Transition in Euo, Physical Review Letters 29 (1972) 1168-1171.
[24] F. Zeng, P. Sheng, G.S. Tang, F. Pan, W.S. Yan, F.C. Hu, Y. Zou, Y.Y. Huang, Z. Jiang, D. Guo, Electronic structure and magnetism of Fe-doped $LiNbO_3$, Materials Chemistry and Physics 136 (2012) 783-788.
[25] Z. He, X. Yang, H. Xia, T.Z. Regier, D.K. Chevrier, X. Zhou, T.K. Sham, Role of defect electronic states in the ferromagnetism in graphite, Phys Rev B 85 (2012) 144406.
[26] H. Bednarski, J. Spalek, Bound-magnetic-polaron molecule in diluted magnetic semiconductors, Journal of Physics-Condensed Matter 24 (2012) 235801.
[27] H. Bednarski, The origin of ferromagnetic interaction between bound magnetic polarons in diluted magnetic semiconductors: A minimal model, J Magn Magn Mater 349 (2014) 281-283.
[28] J.M.D. Coey, D(0) Ferromagnetism, Solid State Sciences 7 (2005) 660-667.
[29] J.M.D. Coey, M. Venkatesan, C.B. Fitzgerald, Donor impurity band exchange in dilute ferromagnetic oxides, Nat Mater 4 (2005) 173-179.
[30] J.M.D. Coey, P. Stamenov, R.D. Gunning, M. Venkatesan, K. Paul, Ferromagnetism in defect-ridden oxides and related materials, New Journal of Physics 12 (2010) 053025.
[31] F. Cordero, Hopping and clustering of oxygen vacancies in $SrTiO_3$, Materials Science and Engineering A-Structural Materials Properties Microstructure and Processing 521-22 (2009) 77-79.
[32] B.B. Straumal, A.A. Mazilkin, S.G. Protasova, A.A. Myatiev, P.B. Straumal, G. Schuetz, P.A. van Aken, E. Goering, B. Baretzky, Magnetization study of nanograined pure and Mn-doped ZnO films: Formation of a ferromagnetic grain-boundary foam, Phys Rev B 79 (2009) 205206-205206.
[33] F. Banhart, J. Kotakoski, A.V. Krasheninnikov, Structural Defects in Graphene, Acs Nano 5 (2011) 26-41.
[34] D. Choudhury, S. Mukherjee, P. Mandal, A. Sundaresan, U.V. Waghmare, S. Bhattacharjee, R. Mathieu, P. Lazor, O. Eriksson, B. Sanyal, P. Nordblad, A. Sharma, S.V. Bhat, O. Karis, D.D. Sarma, Tuning of dielectric properties and magnetism of $SrTiO_3$ by site-specific doping of Mn, Phys Rev B 84 (2011) 125124.

[35] E.N. Dulov, N.G. Ivoilov, O.A. Strebkov, L.R. Tagirov, V.I. Nuzhdin, R.I. Khaibullin, S. Kazan, F.A. Mikailzade, Magnetic phase composition of strontium titanate implanted with iron ions, Materials Research Bulletin 46 (2011) 2304-2307.
[36] W. Zhang, H.P. Li, W. Pan, Ferromagnetism in Electrospun Co-doped $SrTiO_3$ Nanofibers, Journal of Materials Science 47 (2012) 8216-8222.
[37] Z.Q. Liu, W.M. Lu, S.L. Lim, X.P. Qiu, N.N. Bao, M. Motapothula, J.B. Yi, M. Yang, S. Dhar, T. Venkatesan, Ariando, Reversible room-temperature ferromagnetism in Nb-doped $SrTiO_3$ single crystals, Phys Rev B 87 (2013) 220405.
[38] Y. Zhang, J. Hu, E. Cao, L. Sun, H. Qin, Vacancy induced magnetism in $SrTiO_3$, Journal of Magnetism and Magnetic Materials 324 (2012) 1770-1775.
[39] S.S. Rao, Y.F. Lee, J.T. Prater, A.I. Smirnov, J. Narayan, Laser annealing induced ferromagnetism in $SrTiO_3$ single crystal, Appl Phys Lett 105 (2014) 042403.
[40] W.D. Rice, P. Ambwani, M. Bombeck, J.D. Thompson, G. Haugstad, C. Leighton, S.A. Crooker, Persistent optically induced magnetism in oxygen-deficient strontium titanate, Nature Materials 13 (2014) 481-487.
[41] W. Xu, J. Yang, W. Bai, K. Tang, Y. Zhang, X. Tang, Oxygen vacancy induced photoluminescence and ferromagnetism in $SrTiO_3$ thin films by molecular beam epitaxy, J Appl Phys 114 (2013) 154106.
[42] W. Zhang, H.-P. Li, W. Pan, Ferromagnetism in Electrospun Co-doped $SrTiO_3$ Nanofibers, Journal of Materials Science 47 (2012) 8216-8222.
[43] A. Ohtomo, H.Y. Hwang, A high-mobility electron gas at the $LaAlO_3/SrTiO_3$ heterointerface, Nature 427 (2004) 423-426.
[44] Ariando, X. Wang, G. Baskaran, Z.Q. Liu, J. Huijben, J.B. Yi, A. Annadi, A.R. Barman, A. Rusydi, S. Dhar, Y.P. Feng, J. Ding, H. Hilgenkamp, T. Venkatesan, Electronic phase separation at the $LaAlO_3/SrTiO_3$ interface, Nat Commun 2 (2011) 188.
[45] Z.Q. Liu, L. Sun, Z. Huang, C.J. Li, S.W. Zeng, K. Han, W.M. Lu, T. Venkatesan, Ariando, Dominant role of oxygen vacancies in electrical properties of unannealed $LaAlO_3/SrTiO_3$ interfaces, J Appl Phys 115 (2014) 054303.
[46] Y.L. Han, S.C. Shen, J. You, H.O. Li, Z.Z. Luo, C.J. Li, G.L. Qu, C.M. Xiong, R.F. Dou, L. He, D. Naugle, G.P. Guo, J.C. Nie, Two-dimensional superconductivity at (110) $LaAlO_3/SrTiO_3$ interfaces, Appl Phys Lett 105 (2014) 192603
[47] M. Verissimo-Alves, P. Garcıa-Fernandez, D.I. Bilc, P. Ghosez, J. Junquera, Highly Confined Spin-Polarized Two-Dimensional Electron Gas in $SrTiO_3/SrRuO_3$ Superlattices, Physical Review Letters 108 (2012) 107003.
[48] M. Wang, M. Feng, Ab initio study on magnetism at $TiO_2/SrTiO_3$ interface, Comp Mater Sci 86 (2014) 43-48.
[49] J.M.D. Coey, M. Venkatesan, C.B. Fitzgerald, A.P. Douvalis, I.S. Sanders, Ferromagnetism of a graphite nodule from the Canyon Diablo meteorite, Nature 420 (2002) 156-159.
[50] X.M. Yang, Z.T. He, W.F. Li, H.H. Xia, Y. Song, X.T. Zhou, X.D. Liu, M.W. Zhao, T.W. Wang, K.Y. Hou, Localized defects closely related with the magnetism of graphite induced by $^{12}C^{+}$ ion implantation, J Appl Phys 109 (2011) 083933.
[51] A. Rajca, J. Wongsriratanakul, S. Rajca, Magnetic ordering in an organic polymer, Science 294 (2001) 1503-1505.

[52] X. Wang, Z.X. Liu, Y.L. Zhang, F.Y. Li, R.C. Yu, C.Q. Jin, Evolution of magnetic behaviour in the graphitization process of glassy carbon, Journal of Physics-Condensed Matter 14 (2002) 10265-10272.
[53] P.O. Lehtinen, A.S. Foster, Y.C. Ma, A.V. Krasheninnikov, R.M. Nieminen, Irradiation-induced magnetism in graphite: A density functional study, Physical Review Letters 93 (2004) 187202.
[54] M. Topsakal, E. Aktuerk, H. Sevincli, S. Ciraci, First-principles approach to monitoring the band gap and magnetic state of a graphene nanoribbon via its vacancies, Phys Rev B 78 (2008) 235435.
[55] O.V. Yazyev, Emergence of magnetism in graphene materials and nanostructures, Reports on Progress in Physics 73 (2010) 056501.
[56] X.Y. Cui, R.K. Zheng, Z.W. Liu, L. Li, B. Delley, C. Stampfl, S.P. Ringer, Magic numbers of nanoholes in graphene: Tunable magnetism and semiconductivity, Phys Rev B 84 (2011) 125410.
[57] M.M. Ugeda, I. Brihuega, F. Guinea, J.M. Gomez-Rodriguez, Missing Atom as a Source of Carbon Magnetism, Physical Review Letters 104 (2010) 096804.
[58] A. Akbari-Sharbaf, M.G. Cottam, G. Fanchini, A combined theoretical-experimental investigation of paramagnetic centres in chemically exfoliated graphene nanoribbons, J Appl Phys 114 (2013) 024309
[59] A. Akbari-Sharbaf, M.G. Cottam, Influence of zigzag edges on the Ruderman-Kittel-Kasuya-Yosida interaction between magnetic impurities in graphene nanoribbons, J Appl Phys 116 (2014) 194309.
[60] P. Esquinazi, D. Spemann, R. Hohne, A. Setzer, K.H. Han, T. Butz, Induced magnetic ordering by proton irradiation in graphite, Physical Review Letters 91 (2003) 227201.
[61] R. Hohne, P. Esquinazi, V. Heera, H. Weishart, A. Setzer, D. Spemann, The influence of iron, fluorine and boron implantation on the magnetic properties of graphite, J Magn Magn Mater 320 (2008) 966-977.
[62] H.P.R. Frederikse, G.A. Candela, Magnetic Susceptibility of Insulating and Semiconducting Strontium Titanate, Physical Review 147 (1966) 583-584.
[63] S.M.M. Yee, D.A. Crandles, L.V. Goncharova, Ferromagnetism on the unpolished surfaces of single crystal metal oxide substrates, J Appl Phys 110 (2011) 033906.
[64] D.A. Crandles, B. DesRoches, F.S. Razavi, A search for defect related ferromagnetism in $SrTiO_3$, J Appl Phys 108 (2010) 053908.
[65] G.-b. Han, S.-j. Hu, S.-s. Yan, L.-m. Mei, Oxygen vacancy induced ferromagnetism in rutile TiO2-x, Physica Status Solidi-Rapid Research Letters 3 (2009) 148-150.
[66] M. Djermouni, A. Zaoui, S. Kacimi, B. Bouhafs, Vacancy defects in strontium titanate: Ab initio calculation, Computational Materials Science 49 (2010) 904-909.
[67] M. Khalid, A. Setzer, M. Ziese, P. Esquinazi, D. Spemann, A. Poeppl, E. Goering, Ubiquity of ferromagnetic signals in common diamagnetic oxide crystals, Phys Rev B 81 (2010) 214414.
[68] L.V. Goncharova, D.G. Starodub, E. Garfunkel, T. Gustafsson, V. Vaithyanathan, J. Lettieri, D.G. Schlom, Interface structure and thermal stability of epitaxial $SrTiO_3$ thin films on Si(001), J Appl Phys 100 (2006) 014912.

[69] Z. Sun, W. Yan, G. Zhang, H. Oyanagi, Z. Wu, Q. Liu, W. Wu, T. Shi, Z. Pan, P. Xu, S. Wei, Evidence of substitutional Co ion clusters in $Zn_{1-x}Co_xO$ dilute magnetic semiconductors, Phys Rev B 77 (2008) 245208.
[70] A. Shalimov, S. Zhou, O. Roshchupkina, N. Jeutter, C. Baehtz, G. Talut, H. Reuther, K. Potzger, Multiple ferromagnetic secondary phases in Fe implanted yttria stabilized zirconia, J Appl Phys 108 (2010) 024907.
[71] Q. Xu, S. Zhou, Z. Wen, D. Wu, T. Qiu, M. Xu, K. Potzger, H. Schmidt, Magnetic characterization of $Bi(Fe_{1-x}Mn_x)O_3$, Physics Letters a 375 (2011) 1209-1212.
[72] S. Zhou, K. Potzger, Q. Xu, K. Kuepper, G. Talut, D. Marko, A. Muecklich, M. Helm, J. Fassbender, E. Arenholz, H. Schmidt, Spinel ferrite nanocrystals embedded inside ZnO: Magnetic, electronic, and magnetotransport properties, Phys Rev B 80 (2009) 094409.
[73] A. Ney, T. Kammermeier, V. Ney, K. Ollefs, S. Ye, Limitations of measuring small magnetic signals of samples deposited on a diamagnetic substrate, Journal of Magnetism and Magnetic Materials 320 (2008) 3341-3346.
[74] P. Esquinazi, J. Barzola-Quiquia, D. Spemann, M. Rothermel, H. Ohldag, N. Garcia, A. Setzer, T. Butz, Magnetic order in graphite: Experimental evidence, intrinsic and extrinsic difficulties, J Magn Magn Mater 322 (2010) 1156-1161.
[75] M. Sepioni, R.R. Nair, I.L. Tsai, A.K. Geim, I.V. Grigorieva, Revealing common artifacts due to ferromagnetic inclusions in highly oriented pyrolytic graphite, Epl 97 (2012) 47001.
[76] D. Spemann, P. Esquinazi, A. Setzer, W. Bohlmann, Trace element content and magnetic properties of commercial HOPG samples studied by ion beam microscopy and SQUID magnetometry, AIP Adv. 4 (2014) 107142.
[77] M. Venkatesan, P. Dunne, Y.H. Chen, H.Z. Zhang, J.M.D. Coey, Structural and magnetic properties of iron in graphite, Carbon 56 (2013) 279-287.

Chapter 8. Conclusions

Recently, numerous studies have shown that the properties of strontium titanate and carbon-based materials can be controlled by suitable doping and structure modification. In this thesis, properties of strontium titanate (STO) and highly oriented pyrolytic graphite (HOPG) were modified by the ion beam implantation method. Both materials have immense potential for applications in different areas, including spintronics, catalysts or gas sensors. Doping and structural defects affect such important characteristics as conductivity, catalytic activity, luminescent and magnetic properties of STO and HOPG [1-9]. For example, in STO, which is a high-κ dielectric in the pure state, the defect states increase the ionic and electronic conductivity [1, 2]. In carbon materials on the other hand, defects can limit the conductivity, inducing semiconductor properties [10, 11]. The possibility of defect-induced ferromagnetism was theoretically predicted in $SrTiO_3$ and graphite material [6-8, 12, 13]. However, the experimental results suffer from poor reproducibility due to the very unpredictable behaviour of defects in real crystals. The comprehensive study conducted in this thesis helped in the better understanding of how doping and defects affect local structure and magnetic properties of these materials.

Several complementary experimental techniques, including PIXE, RBS, XANES and XPS, were applied to study the influence of ion irradiation on the structural and magnetic properties of $SrTiO_3$ and HOPG. The used methods provided very important and comprehensive information about chemical composition, oxidation state and distribution of impurities.

One part of the thesis was devoted to Fe-doped strontium titanate. Comparison of random and channeled RBS spectra showed that though oxygen annealing improved the crystal structure of STO, it did not return to its initial state, and a new phase was formed in the near-surface layer.

Analysis of Fe-doped STO showed that as implanted iron had Fe^0 oxidation and exhibited ferromagnetic behaviour. O_2 annealing at 350°C changed the iron oxidation to Fe^{3+} and frustrated the ferromagnetic response. XANES spectra collected in TEY and

TFY detection modes are able to probe different depths, which allows us to distinguish the surface and the bulk signals. It was detected that on the surface of the implanted and annealed samples the oxidation state of iron was Fe^{2+}. This showed that despite the oxygen annealing, such defects as oxygen vacancies tend to collect in the surface area. The spectra analysis indicated that the annealing caused Fe to incorporate into the STO structure and substitute for Ti. Calculations conducted using the FEFF9 program suggested that the best model for Fe implanted and annealed STO samples is the formation of $Sr_8Ti_3Fe_5O_{23}$ clusters.

The XPS analysis showed an increase of chemical reactivity of the STO surface after ion irradiation and post-implantation anneal. The increase of C and O peaks on the Fe-implanted STO surface indicated that the defective STO surface reacted more easily with the gases of the ambient atmosphere. The changes revealed by XPS spectra implied formation of strontium carbonates and strontium hydroxide on the STO surface.

Ion irradiation and heat treatment also led to Sr loss in the surface area as evident from RBS analysis. The effect was dependent on the implantation dose and was the most noticeable for the samples with the highest implantation dose used in this study (2×10^{16} Fe^{+}ions/cm^2). The proposed explanation of Sr loss is that in the presence of irradiation defects and carbon contamination, rather unstable phases containing SrO, $SrCO_3$ and $Sr(OH)_2$ could be formed on the STO surface. SrO can desorb from the surface, leaving a Sr-depleted layer, while $SrCO_3$ and $Sr(OH)_2$ have lower physical densities compared to $SrTiO_3$, leading to reduced areal densities for Sr in the layer affected by the implantation process, as measured by RBS.

As found in our PIXE analysis, the HOPG used in this study contained metallic impurities which could be potentially responsible for the magnetic moments of the graphite samples. However Fe concentrations were below detection limits of RBS and XANES. To overcome the low sensitivity of the RBS method to light elements, we used non-Rutherford cross sections to detect changes in oxygen and nitrogen contents by RBS analysis of HOPG samples implanted with O and N ions. Our distributions of implanted N and O were in agreement with the SRIM simulation. The annealing at 100°C in vacuum did not lead to the redistribution or loss of implanted O and N.

For HOPG implanted with O and N, ion irradiation also led to enhanced surface reactivity. The XANES C K-edge spectra clearly demonstrated the appearance of new absorption features due to various functional groups on the surface. The position of the adsorption peaks allowed their identification as carbonyl, carboxyl, hydroxyl and epoxide groups. There was dependence on the implantations dose; however no considerable difference was found between HOPG irradiated with N and O. These results indicated that N is weakly physisorbedin graphite and detected functional groups are the products of reactions between the surface defect sites and ambient gases (O_2, H_2O, CO_2).

The connection between the ion implantation and the induced magnetic properties was investigated by SQUID analysis. There was a correlation found between the observed magnetic moments and the implantation treatment of STO crystals. The STO crystal showed ferromagnetic properties before iron implantation due to the presence of defect (and probably contaminations) on the surface. The low dose Fe implantation actually led to decrease of the magnetic moments because the ion irradiation destroyed the initial defect-related magnetic ordering. Yet the highest implantation dose (2×10^{16} Fe^{+} ions/cm^2) result in an increase of the measured magnetic moment due to higher concentration of oxygen defects and the presence of Fe atoms. This level of Fe implantation would be suitable for fabrication of spintronic devices and can be explored further.

However thermal anneal in oxygen destroys the magnetic ordering. Oxygen annealing healed oxygen vacancies and at the same time led to a change in the oxidation state and the local structure of the implanted iron. In annealed samples Fe built into the STO crystal structure substituting on Ti sites, and as was mentioned above the oxidation state changed from Fe^0 to Fe^{3+}. Therefore, the magnetic moments of STO depend not only on the doping dose, but also on the oxidation state of the dopant and on the defect concentration. The XANES results for Fe-implanted STO provided information about the change in oxidation state and local structure of Fe atoms. However they did not rule out the clustering of dopant. EXAFS study can help to determine the distances between the Fe atoms in the implanted samples. In future work, more systematic study with a higher range of Fe implantation doses can clarify the dependence between the magnetism observed in STO and the Fe doping concentration.

The loss of Sr on the STO surface after ion implantation also requires more consideration, as it is related to the potential use of these materials in gas sensor applications. Probable reactions on the Fe-doped STO surface should be considered to determine the driving force for the decrease of Sr content. It can be interesting to examine the surface morphology, (or example by using atomic force microscopy.

SQUID results from the HOPG samples showed that the metallic inclusions in graphite are likely to overshadow the effect of ion irradiation, and the measured magnetic moments were correlated with the impurity concentrations detected by PIXE.

SQUID is an extremely sensitive method, and in the area of low magnetic moments the purity of the original samples is very important. Even though extreme care was taken during the handling of the STO and HOPG samples, the surface contaminations cannot be completely overruled out. Thus, in ideal situations, when several analytic methods in different locations were used, it would be advisable to prepare a separate set of samples for magnetic measurement to avoid any contamination. To study magnetism in graphite, a new source (manufacturer) of HOPG samples needs to be considered in the future, and careful analysis (including PIXE) need to be conducted to make sure that no significant level of ferromagnetic impurities is present prior to the ion beam implantation experiments. If in the future experiments we confirm that a ferromagnetic response can be produced by ion implantation experiments in the absence of transition metal impurities by SQUID magnetometry, we can study this phenomenon further. It would be interesting to test depth distribution of defects with scanning tunneling microscopy to identify different defect configurations and their magnetic signatures.

References

[1] M.D. Drahus, P. Jakes, E. Erdem, R.-A. Eichel, Defect structure of the mixed ionic-electronic conducting Sr[Ti,Fe]O_x solid-solution system - Change in iron oxidation states and defect complexation, Solid State Ionics 184 (2011) 47-51.
[2] M. Djermouni, A. Zaoui, S. Kacimi, B. Bouhafs, Vacancy defects in strontium titanate: Ab initio calculation, Computational Materials Science 49 (2010) 904-909.
[3] X. Wei, G. Xu, Z.H. Ren, C.X. Xu, W.J. Weng, G. Shen, G.R. Han, Single-crystal-like mesoporous $SrTiO_3$ spheres with enhanced photocatalytic performance, J Am Ceram Soc 93 (2010) 1297-1305.
[4] B. Wang, Recent development of non-platinum catalysts for oxygen reduction reaction, J. Power Sources 152 (2005) 1-15.
[5] Y. Yamada, Y. Kanemitsu, Photoluminescence spectra of perovskite oxide semiconductors, Journal of Luminescence 133 (2013) 30-34.
[6] J.M.D. Coey, P. Stamenov, R.D. Gunning, M. Venkatesan, K. Paul, Ferromagnetism in defect-ridden oxides and related materials, New Journal of Physics 12 (2010) 053025.
[7] M.M. Ugeda, I. Brihuega, F. Guinea, J.M. Gomez-Rodriguez, Missing Atom as a Source of Carbon Magnetism, Physical Review Letters 104 (2010) 096804.
[8] P.O. Lehtinen, A.S. Foster, Y.C. Ma, A.V. Krasheninnikov, R.M. Nieminen, Irradiation-induced magnetism in graphite: A density functional study, Physical Review Letters 93 (2004) 187202.
[9] X.Y. Sun, R. Wang, D.S. Su, Research progress in metal-free carbon-based catalysts, Chin. J. Catal. 34 (2013) 508-523.
[10] V. Singh, D. Joung, L. Zhai, S. Das, S.I. Khondaker, S. Seal, Graphene based materials: Past, present and future, Prog Mater Sci 56 (2011) 1178-1271.
[11] C.K. Chang, S. Kataria, C.C. Kuo, A. Ganguly, B.Y. Wang, J.Y. Hwang, K.J. Huang, W.H. Yang, S.B. Wang, C.H. Chuang, M. Chen, C.I. Huang, W.F. Pong, K.J. Song, S.J. Chang, J.H. Guo, Y. Tai, M. Tsujimoto, S. Isoda, C.W. Chen, L.C. Chen, K.H. Chen, Band Gap Engineering of Chemical Vapor Deposited Graphene by in Situ BN Doping, Acs Nano 7 (2013) 1333-1341.
[12] J.M.D. Coey, M. Venkatesan, C.B. Fitzgerald, Donor impurity band exchange in dilute ferromagnetic oxides, Nat Mater 4 (2005) 173-179.
[13] S.J. Pearton, W.H. Heo, M. Ivill, D.P. Norton, T. Steiner, Dilute magnetic semiconducting oxides, Semicond. Sci. Technol. 19 (2004) R59-R74.

CURRICULUM VITAE

Education

2008	MSc, University of Western Ontario, London, Ontario, Canada
	Diploma: *Optical Properties of Zinc Oxide Nanostructures: X-ray Absorption Spectroscopy, X-ray Excited Optical Luminescence and Cathodoluminescence Studies,* (Supervisor Prof. T.K. Sham)
1989	Specialist in Physics, Saint-Petersburg State University, Saint-Petersburg, Russia
	Diploma: *Adsorption of Lutetium on Tungsten Single Crystal Planes*

Related work experience	Research assistant, Teaching assistant Department of Physics, University of Western Ontario
Honours and rewards	Queen Elizabeth II scholarship in Science and Technology, University of Western Ontario, 2013-2014
	Honorable Mention in the overall student poster competition at CAP Congress, 2013
	CEWIP best Overall student poster presentation award at CAP Congress, 2013

Selected publications

1) O. Lobacheva, Y.M.Yiu, T.K. Sham, and L.V. Goncharova *Effects of N and O ion irradiation on the graphite structure and magnetic properties,* in preparation.
2) O. Lobacheva, Y.M.Yiu, N. Chen, T.K. Sham, and L.V. Goncharova *Changes in local surface structure and Sr loss in Fe-implanted $SrTiO_3$ (100),* in preparation
3) O. Lobacheva, M. Chavarha, Y.M. Yiu, T.K. Sham, and L.V. Goncharova *The local structure and ferromagnetism in Fe-implanted $SrTiO_3$ single crystals,* Journal of Applied Physics **116**, 013901, 2014.
4) O. Lobacheva, L.V. Goncharova, M. Chavarha, and T.K. Sham, *XANES study of Fe-implanted strontium titanate,* AIP Conference Proceedings 1590, 82, 2014.
5) O. Lobacheva, P.L. Corcoran, M.W. Murphy, J.Y.P. Ko, and T.K. Sham *Cathodoluminescence (CL), X-ray Excited Optical Luminescence (XEOL) and X-ray Absorption Near Edge Structures (XANES) studies of ZnO nanostructures* Canadian Journal of Chemistry-Revue Canadienne de Chimie 90, 298-305, 2012.
6) O. Lobacheva, M.W. Murphy, J.Y.P. Ko, and T.K. Sham *Morphology dependent luminescence from ZnO nanostructures: an X-ray Excited Optical Luminescence*

study at the Zn K-edge Canadian Journal of Chemistry-Revue Canadienne de Chimie 87, 9, 1255-1260, 2009.

7) O.A. Lobacheva, J.Y.P. Ko, M.W. Murphy, L. Liu, T. K. Sham *XANES and XEOL Studies of Rare-earth Phosphor Powder (La,Ce,Tb)PO_4* CLS Activity Report 2008, 28-29,June 2009.